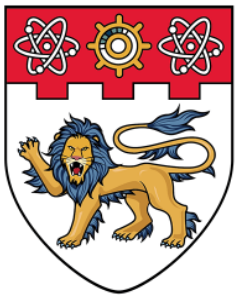

NANYANG TECHNOLOGICAL UNIVERSITY
SINGAPORE

NANOMATERIAL ENGINEERED VOLTAMMETRIC SENSORS FOR TARGETED ON-SITE MONITORING AND SPECIATION OF HEAVY METAL IONS

ZHAO KE
SCHOOL OF CIVIL AND ENVIRONMENTAL ENGINEERING

2024

NANOMATERIAL ENGINEERED VOLTAMMETRIC SENSORS FOR TARGETED ON-SITE MONITORING AND SPECIATION OF HEAVY METAL IONS

ZHAO KE

School of Civil and Environmental Engineering

A thesis submitted to the Nanyang Technological University
in partial fulfilment of the requirement for the degree of
Doctor of Philosophy

2024

Statement of Originality

I hereby certify that the work embodied in this thesis is the result of original research, is free of plagiarised materials, and has not been submitted for a higher degree to any other University or Institution.

08th August 2024

. . . . . .

Date

. . . . . .

Zhao Ke

Supervisor Declaration Statement

I have reviewed the content and presentation style of this thesis and declare it is free of plagiarism and of sufficient grammatical clarity to be examined. To the best of my knowledge, the research and writing are those of the candidate except as acknowledged in the Author Attribution Statement. I confirm that the investigations were conducted in accord with the ethics policies and integrity standards of Nanyang Technological University and that the research data are presented honestly and without prejudice.

08th August 2024

. . . . . .
Date

. . . . . .
Grzegorz Lisak

Authorship Attribution Statement

This thesis contains material from 4 papers published in the following peer-reviewed journals, in which I am listed as an author.

Chapter 3 is published as Ke Zhao, Liya Ge and Grzegorz Lisak. Facile synthesis of electrocatalytically active bismuth oxide nanosheets for detection of palladium traces in pharmaceutical wastewater, *Environmental Pollution* **307**, 119524 (2022). DOI: doi.org/10.1016/j.envpol.2022.119524.

The contributions of the co-authors are as follows:

- Ke Zhao: Conceptualization, investigation, data curation, visualization, writing-original draft.
- Liya Ge: Conceptualization, methodology, validation, writing-original draft.
- Grzegorz Lisak: Conceptualization, methodology, supervision, writing-review & editing.

Chapter 4 is published as Ke Zhao, Liya Ge, Ten It Wong, Xiaodong Zhou and Grzegorz Lisak. Gold-silver nanoparticles modified electrochemical sensor array for simultaneous determination of chromium(III) and chromium(VI) in wastewater samples. *Chemosphere*. **2811**, 130880 (2021). DOI: doi.org/10.1016/j.chemosphere.2021.130880.

The contributions of the co-authors are as follows:

- Ke Zhao: Conceptualization, investigation, data curation, visualization, writing-original draft.
- Liya Ge: Conceptualization, methodology, validation, writing-original draft.
- Ten It Wong: Formal analysis, visualization, writing-review & editing.
- Xiaodong Zhou: Methodology, visualization, writing-review & editing.
- Grzegorz Lisak: Conceptualization, methodology, supervision, writing-review & editing.

Chapter 5 is published as Ke Zhao, Canwei Mao, Ruiyu Ding, Dean Song, Liya Ge and Grzegorz Lisak. Simultaneous Speciation of Inorganic Arsenic (III and V) Utilizing Gold-Manganese Oxide Nanoparticles Modified Electrochemical Sensors. *Electrochimica Acta.* 144796 (2024). DOI: doi.org/10.1016/j.electacta.2024.144796

The contributions of the co-authors are as follows:

- Ke Zhao: Conceptualization, investigation, data curation, visualization, writing-original draft.
- Canwei Mao: Conceptualization, investigation, data curation, visualization, writing-original draft.
- Ruiyu Ding: Conceptualization, investigation, data curation, visualization, writing-original draft.

- Dean Song: Conceptualization, methodology, validation, writing-original draft.
- Liya Ge: Conceptualization, methodology, validation, writing-original draft.
- Grzegorz Lisak: Conceptualization, methodology, supervision, writing-review & editing.

Chapter 6 is published as Ke Zhao, Canwei Mao, Ruiyu Ding, Cherilyn Wong, Liya Ge and Grzegorz Lisak. Rapid on-site determination of heavy metals and metalloids in contaminated biochar samples by accelerated leaching process coupled with voltammetric sensors. *Talanta* (2025): 127572. DOI: doi.org/10.1016/j.talanta.2025.127572

The contributions of the co-authors are as follows:

- Ke Zhao: Conceptualization, investigation, data curation, visualization, writing-original draft.
- Canwei Mao: Conceptualization, investigation, data curation, visualization, writing-original draft.
- Ruiyu Ding: Conceptualization, investigation, data curation, visualization, writing-original draft.
- Cherilyn Wong: Investigation, data curation.
- Liya Ge: Conceptualization, methodology, validation, writing-original draft.
- Grzegorz Lisak: Conceptualization, methodology, supervision, writing-review & editing.

08th August 2024

. . . . . .
Date

. . . . . .
Zhao Ke

ACKNOWLEDGEMENTS

I am profoundly grateful to all those who have supported me throughout my Ph.D. journey. This thesis would not have been possible without the guidance, support, and encouragement of many individuals and organizations.

First and foremost, I would like to thank my supervisor, Dr. Grzegorz Lisak, Associate Professor at the School of Civil and Environmental Engineering (CEE), Nanyang Technological University (NTU), for his unwavering support, insightful guidance, and expert knowledge. His patience and encouragement have equipped me for the successful completion of this research. I am honored to have been his student. My gratitude also goes to Dr. Ge Liya, Senior Research Fellow, for her invaluable guidance and for introducing me to the vibrant academic community at NTU.

I would like to extend my sincere thanks to the members of my thesis committee, Prof. Fei Xunchang and Prof. Lim Teik Thye, for their constructive feedback and suggestions that significantly improved the quality of this work.

I gratefully acknowledge the workmates from Nanyang Environment & Water Research Institute (NEWRI), especially those from Residues, Resource and Reclamation Centre and Analytics Cluster. With your cooperation and companionship, I was able to complete various experiments and characterizations, and eventually publish scientific publications. Also, I am grateful that CEE and NEWRI provided me the chance and essential recourses to undertake my Ph.D. study.

Last but not least, I would like to express my heartfelt gratitude to my family and friends. Your support has been my pillar of strength in facing all the challenges during these studies. Once again, thank you all for your part in my journey!

Table of Contents

SUMMARY

Heavy metals have garnered significant attention due to their detrimental effects on the environment and living organisms. However, heavy metals can also be valuable resources. Monitoring of heavy metals is crucial for both pollution control and resource recovery. Currently, standard detection methods require lab-scale instruments such as atomic absorption spectrometry (AAS), inductively coupled plasma optical emission spectroscopy (ICP-OES), inductively coupled plasma mass spectrometry (ICP-MS), and UV–visible absorption spectroscopy (UV-Vis). Additionally, the valence state of some metal ions is closely related to their toxicity, necessitating the speciation of heavy metal ions. This often involves high-performance liquid chromatography (HPLC) to separate species before measurement with the aforementioned instruments. These methods are expensive, time-consuming, and require professional operators, making on-site detection and monitoring challenging. In recent years, electrochemical sensors have been introduced for rapid on-site pollutant detection due to their high sensitivity, high selectivity, low cost, portability, and ease of operation. Electrochemical sensing requires only electrodes (sensors), an electrochemical workstation, and a laptop, making it a convenient and efficient solution for monitoring pollutants.

In this work, screen-printed carbon electrodes (SPCEs) were used to explore the potential for monitoring and speciation of several heavy metal ions. Different nanomaterials were synthesized and modified onto the SPCEs: (i) bismuth oxide nanosheets with flake-shaped structures (300-1000 nm wide and 6-10 nm thick) were employed to detect Pd(II) in a palladium recovery process; (ii) gold-manganese oxide (Au/Mn = 10/1, m/m) nanoparticles were utilized to monitor and speciate As(III) and As(V) in a wastewater treatment process; (iii) gold-silver (Au/Ag = 100/1, m/m) nanoparticles were developed for the speciation and detection of Cr(III) and Cr(VI) in tap water, artificial saliva, artificial sweat, and wastewater samples; (iv) SPCEs were applied directly for the determination of Cd(II) and Pb(II), while commercially available gold-modified SPCEs were used to measure Hg(II). Finally, an ultrasound-assisted leaching procedure was optimized for artificially contaminated biochar samples (compared to the standard Toxicity Characteristic Leaching Procedure). The leachates were analyzed using both developed sensors and bulk instruments. The consistent results from both methods confirm the feasibility of applying voltammetric sensors for the speciation and monitoring of heavy metal ions in environmental samples.

LIST OF PUBLICATIONS

Journal papers:

1. Ke, Zhao, Liya Ge, Ten It Wong, Xiaodong Zhou, and Grzegorz Lisak. "Gold-silver nanoparticles modified electrochemical sensor array for simultaneous determination of chromium (III) and chromium (VI) in wastewater samples." Chemosphere 281 (2021): 130880.
2. Ke, Zhao, Liya Ge, and Grzegorz Lisak. "Facile synthesis of electrocatalytically active bismuth oxide nanosheets for detection of palladium traces in pharmaceutical wastewater." Environmental Pollution 307 (2022): 119524.
3. Ke, Zhao, Canwei Mao, Ruiyu Ding, Dean Song, Liya Ge, and Grzegorz Lisak. "Simultaneous Speciation of Inorganic Arsenic (III and V) Utilizing Gold-Manganese Oxide Nanoparticles Modified Electrochemical Sensors." Electrochimica Acta (2024): 144796.
4. Zhao, Ke, Canwei Mao, Ruiyu Ding, Cherilyn Wong, Liya Ge, and Grzegorz Lisak. "Rapid on-site determination of heavy metals and metalloids in contaminated biochar samples by accelerated leaching process coupled with voltammetric sensors." Talanta (2025): 127572.

LIST OF TABLES

LIST OF FIGURES

LIST OF ABBREVIATIONS AND SYMBOLS

Abbreviation/ Symbol	Description
AAS	atomic absorption spectrometry
ACB	artificially contaminated biochar
AFM	atomic force microscope
AuMnNPs	gold-manganese nanoparticles
AuNP	gold nanoparticle
CE	counter electrode
CONAMA	Brazilian National Council for the Environment
CV	cyclic voltammetry
CVD	chemical vapor deposition
DC	direct current
DCC	diphenyl carbazide colorimetric
DI	Deionized
DNA	deoxyribonucleic acid
DPV	differential pulse voltammetry
E	potential
EDX	energy dispersive X-ray
EIS	electrochemical impedance spectroscopy
FE-SEM	field emission-scanning electron microscopy
GCE	glassy carbon electrode
HER	hydrogen evolution reaction
HMIs	heavy metal ions
HPLC	high-performance liquid chromatography
I	current
IARC	International Agency for Research Cancer
IBA	incineration bottom ash
IC	ion chromatography
ICP-MS	inductively coupled plasma mass spectrometry
ICP-OES	inductively coupled plasma optical emission spectroscopy
ICP-QQQ	inductively coupled plasma triple quadrupole mass spectrometry
IE	indicator electrode
IFA	incineration fly ash

ISE	ion-selective electrode
LOD	limit of detection
LSV	linear sweep voltammetry
MOFs	metal-organic frameworks
MSW	municipal solid waste
MSW	municipal solid waste
ppb	parts per billion
ppm	parts per million
ppt	parts per trillion
RA	rapid adsorption
RE	reference electrode
RNA	ribonucleic acid
SBL	spiked biochar leachate
SD	standard deviation
SHE	standard hydrogen electrode
SPCE	screen-printed carbon electrode
SWV	square wave voltammetry
TCLP	Toxicity Characteristic Leaching Procedure
TEM	transmission electron microscopy
TFT	thin film transistor
TLL	transistor-transistor logic
TOC	total organic carbon
UAL	ultrasound assisted leaching
UAT	ultrasound assisted tumbler
USEPA	United States Environmental Protection Agency
UV-Vis	ultraviolet–visible absorption spectroscopy
WE	working electrode
WHO	World Health Organization
XPS	X-ray photoelectron spectrometer
XRD	X-ray diffraction

CHAPTER 1 INTRODUCTION

1.1 Background

1.1.1 Heavy metals

Metals and metalloid elements with atomic numbers greater than 20 and densities greater than 5 g/cm³ are generally defined as heavy metals [1, 2]. In the environment, heavy metal ions (HMIs) can cause harm to humans, animals, and even plants when their concentrations exceed toxicity levels. HMIs cannot be naturally degraded and tend to accumulate and transform within organisms [3]. Arsenic, cadmium, chromium, lead, and mercury are classified as priority control heavy metals due to their notable carcinogenic and noncarcinogenic toxicities [4]. The toxicity of HMIs depends on their species, concentration, and valence [5, 6]. Among the priority control heavy metals, arsenic, and chromium are well-known elements with multiple stable valence states. As for arsenic, inorganic arsenic is more concerned because it is more water-soluble than organic arsenic and is more likely to be enriched in organisms [7]. The stable inorganic arsenic species in the environment are mainly arsenate (As(V)) and arsenite (As(III)), among which As(III) is considered to be more toxic [8]. Nevertheless, arsenic species can transform the environment and organisms, and their toxicity may change accordingly [9]. Similar to arsenic, inorganic chromium also has two stable oxidation states in nature: hexavalent (Cr (VI)) and trivalent (Cr (III)) [10]. Cr(VI) is a recognized strong carcinogen and can cause serious health problems either from acute exposure or chronic accumulation [11, 12]. However, Cr(III) is an essential trace element for the human body [13]. Thus, it is important to monitor and speciate the HMIs.

In addition, some pollutants can also be treated and recovered as useful products. Technologies for recovering heavy metals from wastewater are increasingly being developed [14, 15]. Monitoring the concentration of heavy metals recovered during these processes is also crucial.

1.1.2 Nanomaterials in electrochemical sensing applications and synthesis of

nanomaterials

Nanomaterials are characterized by having at least one external dimension within the range of 1 to 100 nanometers. Due to their unique size-dependent properties and vast surface area, nanomaterials have found applications across diverse fields, including the development of voltammetric sensors [16].

Carbon-based nanomaterials, such as carbon quantum dots (zero-dimensional), carbon nanotubes (one-dimensional), graphene (two-dimensional), (reduced) graphene oxide, fullerenes, carbon nanofibers, and their derivatives, are among the most effective materials for sensors. They exhibit excellent mechanical strength, electrical conductivity, and chemical stability, making them highly suitable for various sensing applications [17, 18].

Precious metals (gold, silver, platinum, and palladium) and non-precious metals (copper, iron, manganese, tungsten, etc.) in nanoparticle form, including their oxides are also widely used in electrochemical sensors due to their special catalytic properties and excellent conductivity [19-22].

Derivatives of metal-organic frameworks (MOFs) and electrode modification materials have received great attention. Due to their low conductivity, MOFs are unsuitable for electrochemical applications [23]. However, its pyrolysis products can still retain the metal core with catalytic properties, the carbon skeleton with high electrical conductivity, and the pore structure [24]. Thus, they are also widely applied in electrochemical sensing [25].

Nanocomposites, composed of two or more materials, as mentioned above, enhance overall performance through synergic effects [26]. Furthermore, even for the same type of nanomaterials, their effects can vary depending on their morphologies and sizes [27]. Consequently, the synthesis techniques for nanomaterials are critical. The synthesis methods of nanomaterials can be divided into physical, biological, and chemical methods, as listed in Table 1 [28]. Among them, physical methods require specialized instruments, while biological methods, typically limited to synthesizing metal nanoparticles, may involve pathogenic bacteria and fungi [28]. Due to its straightforwardness and minimal

equipment requirements, chemical synthesis is the most commonly employed technique. Additionally, the morphology and properties of the product can be easily regulated by adding additives (such as soft/hard templates) or controlling the synthesis conditions (such as temperature, pH, concentration, etc.) [29, 30]. Therefore, the nanomaterials in this study were primarily synthesized using chemical synthesis methods.

Table 1. Synthesis methods of nanomaterials.

Methods		Description	Reference
Physical synthesis	Mechanical force	Mechanical force is used to cut and refine large particles into small particles, such as the ball milling method.	[31]
	High-temperature process	The raw materials are evaporated at high temperatures and then form nanostructures in the condensation zone, using laser evaporation, thermal decomposition, thermolysis, radiofrequency plasmas, or other methods.	[32-34]
	Sputtering method	The sputtering method uses high-energy particles to bombard raw materials and sputter out nanoparticles.	[35]
	Electrospinning	Electrospinning is a process whereby materials (usually polymers) dissolved in a solution are ejected using an electrostatic field to form nanostructures.	[36]
Biosynthesis		Common biosynthesis methods use living microorganisms (such as bacteria and fungi), algae, and bioproducts (such as proteins, deoxyribonucleic acid (DNA), and ribonucleic acid (RNA))	[37-39]
Chemical synthesis	Co-precipitation	Two or more ions come into contact to produce nanoscale precipitates, usually in an aqueous system.	[40]
	Sol-gel process	The precursor is hydrolyzed in a solvent to release monomers, which are then polymerized to form a gel, and nanomaterials can be obtained after drying.	[41]
	Solvothermal method	It involves mixing precursors, which either do not react or react very slowly at normal temperature and pressure, with a solvent (or mixture of solvents) in a container that can withstand high temperatures and pressures. By heating the mixture to a temperature above the solvent's boiling point, high pressure is generated inside the reaction vessel,	[42]

	leading to the formation of nanomaterials. Water can be used as the solvent in this process, and microwave heating can be employed as the heating method.	
Chemical vapor deposition (CVD)	The precursors come into contact and react in the gas phase, and the products are deposited onto the substrate to form a nanomaterial film.	[43]
Electrochemical synthesis	Ions in ionic liquids are to be electrochemically reduced or oxidized at the corresponding electrodes, forming nanomaterials.	[44]

1.1.3 Electrochemical sensing methods

Electrochemical sensing methods mainly include: voltammetry, potentiometry, conductometry, coulometry, and electrochemical impedance spectroscopy (EIS) [45]. Among these methods, voltammetry and potentiometry are commonly applied for sensing HMIs.

Voltammetry is predominant method in electrochemical sensing of HMIs, which involves varying the applied potential and measuring the resulting current or redox reaction. It provides information about redox processes, electrode kinetics, and analyte concentration. Commonly used voltammetric techniques include linear sweep voltammetry (LSV), square wave voltammetry (SWV), cyclic voltammetry (CV), and differential pulse voltammetry (DPV).

In voltammetric analysis, a three-electrode system is normally required. As illustrated in Figure 1(A), the three electrodes are connected to an electrochemical workstation (potentiostat) [46]. The potential (E) between the reference electrode (RE) and the working electrode (WE) is adjusted by the potentiostat. Since the WE is connected to the counter electrode (CE), a potential is generated on the CE to balance the WE, and the current (I) in the path between the WE and CE is recorded [47]. The redox process of an analyte can be visualized by plotting the E vs. I curve, from which the concentration of the analyte can then be further analyzed.

Taking CV as an example, the oxidation peak (Figure 1(B) peak 1) appears during a forward scan (potential from low to high), while the reduction peak (Figure 1(B) peak 2) appears, when the potential is scanned from high to low. The peak height of the peak is proportional to the concentration of the analytes in a certain range (working range/linear range), while the peak position is highly dependent on the redox ability of the analyte, which helps us to identify the analyte.

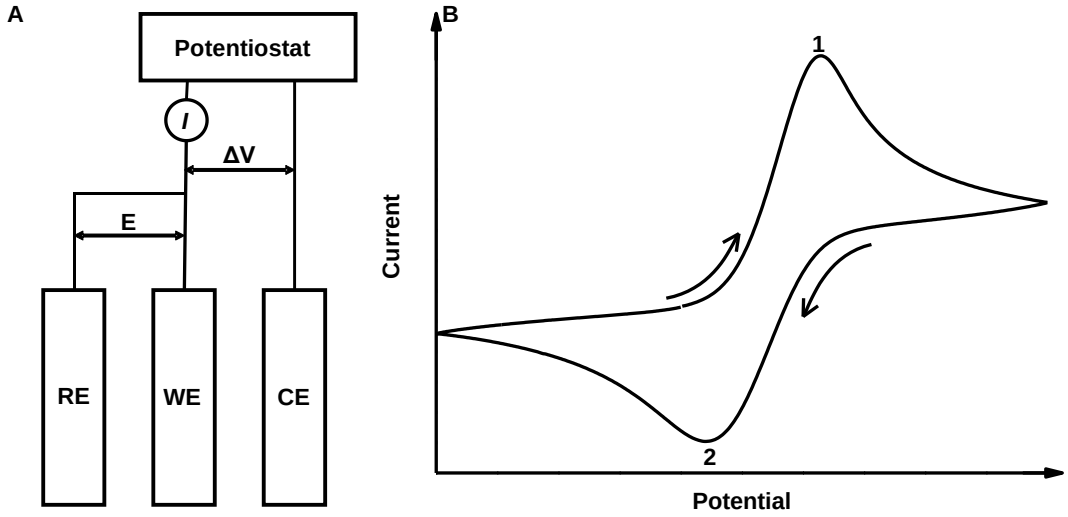

Figure 1. Three electrodes system (A) and a typical CV curve (B) [46].

As shown in Figure 2, the main differences among various voltammetry methods is in voltage applied and how the signal is collected. The applied voltage is linear with time for LSV and CV. The only difference is that CV has an additional reverse scan to complete a closed loop. SWV and DPV apply pulsed potential: in SWV, the pulses alternate between forward and reverse directions, and the sampling value is the current value at the end of the forward pulse (S1) minus the current value at the end of the reverse pulse (S2), which is suitable for studying reversible/quasi-reversible reaction processes; DPV applies a pulse of fixed amplitude at a step potential, and the difference between the current at the end of the pulse (S2) and the current before the pulse (S1) is the recorded current, which can remove the influence of background signals [48]. The limit of detection (LOD) of voltammetric sensors can normally reach parts per billion (ppb), and they are widely applied in HMIs detection [49].

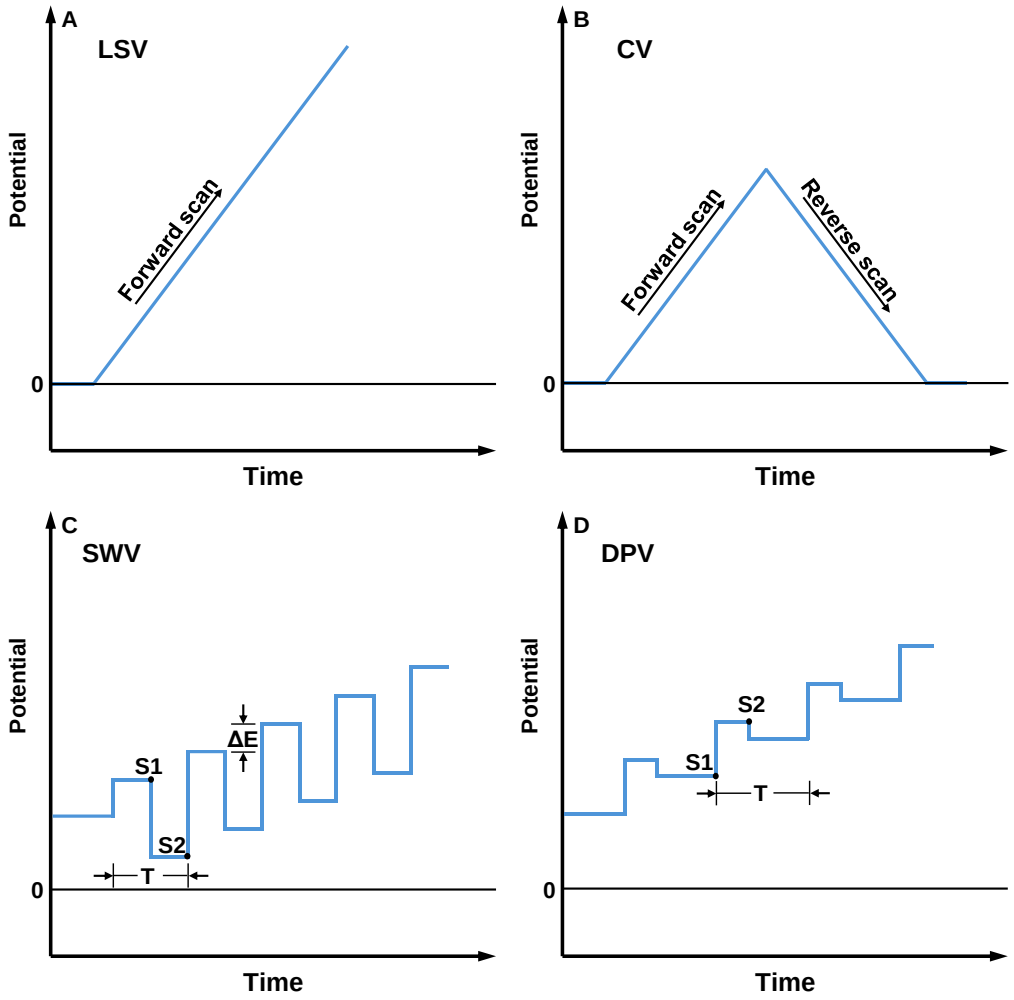

Figure 2. Typical potential waveform of LSV (A), CV (B), SWV (C), and DPV (D) [48].

As shown in Figure 3, potentiometric sensors are usually two-electrode systems consisting of an indicator electrode (IE) and an RE, where the IE is usually an ion-selective electrode (ISE) [50]. Based on the Nernst equation and the potential difference between IE and RE, the concentration of the analyte can be calculated. Potentiometric sensors are mainly applied to analytes with relatively high concentrations (higher than parts per million, ppm) [51, 52].

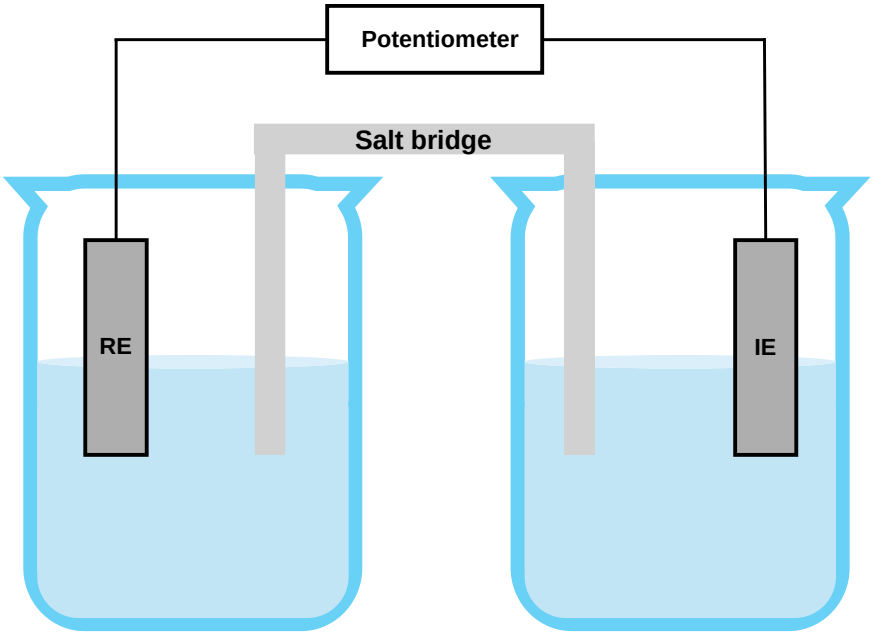

Figure 3. A potentiometric electrochemical cell

Due to the difference in electrochemical activity of the same element in different valence states, it is possible to distinguish the valence states of elements by voltammetry. Here we will be focusing on chromium and arsenic. For chromium, the Eh-pH diagram is shown in Figure 4, where Eh stands for the voltage potential with respect to the standard hydrogen electrode (SHE).

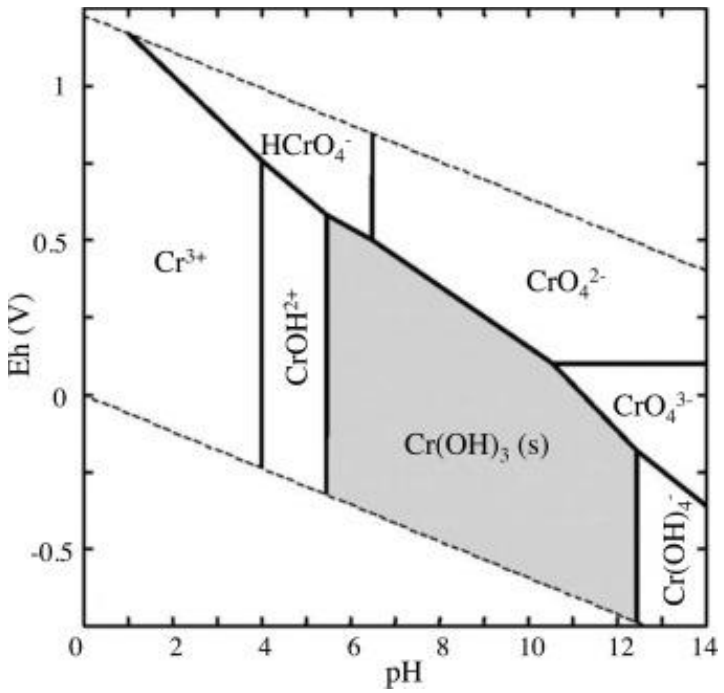

Figure 4. The Eh-pH diagram of Cr–O–H system @298.15 K, 10^5 Pa [53].

The redox reaction between Cr(III) and Cr(VI) in acidic solution can be expressed as [54]:

$$Cr_2O_7{}^{2-} + 6e^- + 14H^+ = 2Cr^{3+} + 7H_2O \qquad E_0 = 1.33\ V$$

and in alkaline solution:

$$CrO_4^{2-} + 3e^- + 4H_2O = Cr(OH)_3 + 5OH^- \qquad E_0 = -0.12\ V$$

Where E_0 is the standard electrochemical potential of oxidation and reduction. Obviously, Cr(VI) is easy to be reduced to Cr(III) in acidic solution and on the contrary, Cr(III) can be oxidized to Cr(VI) in alkaline solution. Using this feature, Cr(VI)/(III) can be detected in acidic/alkaline solutions separately.

Similarly, for arsenic, the Eh-pH diagram is shown in Figure 5. As(III) can be reduced to As(0) under wide pH range while As(V) cannot. In the presence of Mn(0), As(V) can be reduced to As(III) chemically and then further reduced to As(0). Therefore, the addition of Mn can be used to strategically distinguish and detect As(V) and (III).

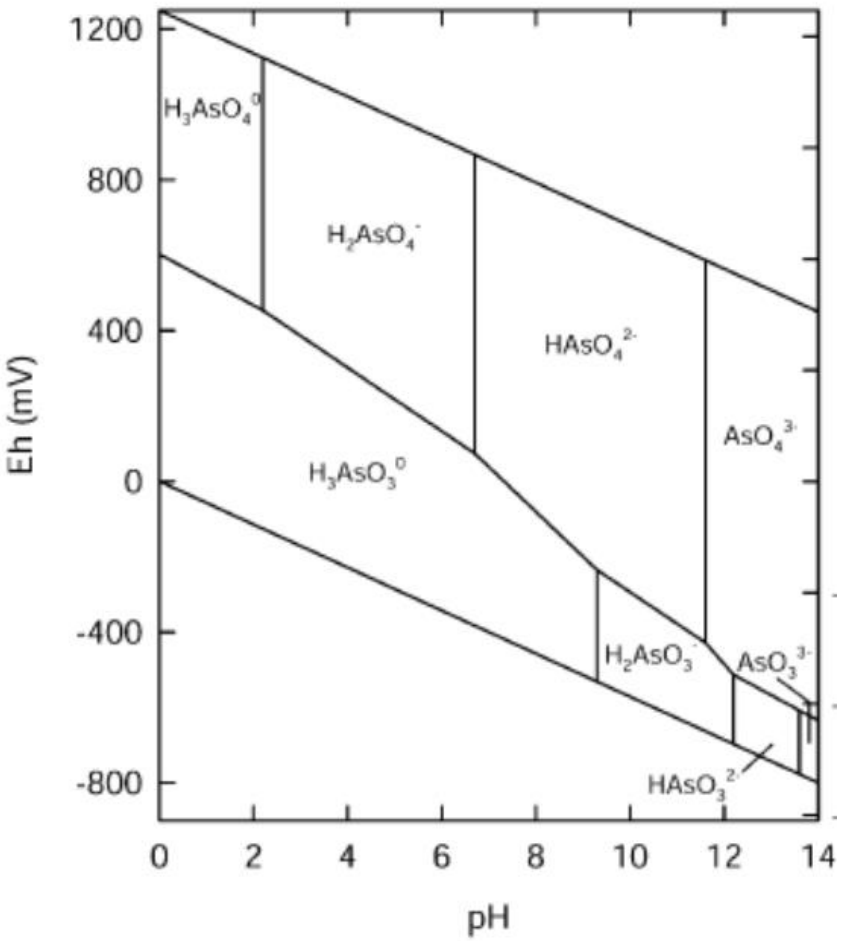

Figure 5. The Eh-pH diagram of Cr–O–H system @298.15 K, 10^5 Pa [55].

Compared with potentiometric sensors, voltammetric sensors are preferred for achieving lower LODs. Beyond measurement parameters, the selection of electrodes is crucial. However, commercially available electrodes, such as glassy carbon electrodes (GCEs), screen-printed carbon electrodes (SPCEs), and graphite electrodes, pose different challenges: they may be unable to reach lower detection ranges, respond to certain pollutants, or avoid interference from other substances in the targeted samples. To address these issues, this research aims to synthesize nanomaterials and modify SPCEs to enhance their sensitivity and selectivity, and thus broaden their applications.

1.2 Purpose and scope

The number or commercially available sensors for targeted on-site monitoring and speciation is scarce, this study focuses on developing new nanomaterials and applying them voltammetric sensors for the detection and speciation of different heavy metal ions. Since different heavy metal ions require targeted engineering, this work focuses on development of three sensitive voltametric type sensors, for detection and speciation of palladium, chromium and arsenic and coupling these into sensing platform that would allow on-site monitoring of those heavy metals. The detailed contents are as follows:

(i) Developed a new method for synthesizing bismuth-derived nanomaterial without adding halogens or metalloids. These nanomaterials were modified onto SPCE and applied to monitor Pd(II) concentrations in pharmaceutical wastewater during the palladium recovery process.

(ii) Developed novel sensors by modifying SPCE with new nanomaterials of stable gold oxide species. These sensors were applied to detect and speciate Cr(III), Cr(VI), and total Cr in various samples, including tap water, artificial saliva, artificial sweat, and during a wastewater treatment process.

(iii) Developed a method for synthesizing a series of Au-Mn oxide nanocomposites with different Au/Mn ratios. A novel sensor was also produced by modifying SPCE with the optimum Au-Mn oxide nanocomposites, which was further applied to the speciation and monitoring of inorganic As(III), As(V), and total As during a wastewater treatment process.

(iv) Developed an accelerated leaching protocol (ultrasound-assisted leaching, UAL) using a homemade ultrasound-assisted tumbler (UAT). This protocol reduces the leaching time from 18 hours to 30 minutes, with results comparable to the Toxicity Characteristic Leaching Procedure (TCLP). The previously developed sensors, along with some commercial sensors, were successfully recalibrated

and applied for simultaneously detecting As(III), As(V), Cd(II), Cr(III), Cr(VI), Hg(II), Pd(II), and Pb(II) in the solid sample leachates.

CHAPTER 2 REVIEW OF THEORY AND PREVIOUS WORK AND RESEARCH GAPS

2.1 Methods for heavy metal detection

Currently, standard methods for the detection of total contents of various heavy metals require the use of bulky lab-scale instruments, such as atomic absorption spectrometry (AAS), inductively coupled plasma optical emission spectroscopy (ICP-OES), and inductively coupled plasma mass spectrometry (ICP-MS) [56, 57]. As shown in Figure 6, electron of heavy metal atom (or ion) on the ground state can absorb light of a specific wavelength (depends on the element) to excited state, by measuring the amount of light absorbed, AAS can calculate the concentration of the element [58]. On the contrary, excited electrons can emit light of a specific wavelength when they return to ground state, which will be detected by ICP-OES detector and then calculate the concentration [59]. ICP-MS has different principle as it measures the ions by mass detector directly [60]. Furthermore, heavy metals presented in various environments can exist in multiple chemical forms and oxidation states, each exhibiting distinct biological activities and toxicological properties [61]. For instance, chromium commonly appears in environmental samples primarily as Cr(III) and Cr(VI), where Cr(VI) is significantly more toxic, acting as a potent mutagen that causes chromosomal aberrations and cancer, whereas Cr(III) is considered an essential nutrient and is beneficial to human health [62, 63]. For speciating these metals in liquid matrices, chromatographic techniques coupled with heavy metal detection methods, such as high-performance liquid chromatography linked with inductively coupled plasma mass spectrometry (HPLC-ICP-MS), prove to be effective [64]. Despite their efficacy, these methods are costly, time-intensive, and require skilled operators, making on-site detection and monitoring of pollutants challenging.

In response to these limitations, recent advancements have led to the development of electrochemical sensors, which offer a rapid method to detect pollutants on-site [65]. These sensors provide the advantages of their high sensitivity,

selectivity, affordability, and portability. Only a set of electrodes, an electrochemical workstation, and a laptop are necessary for this form of electrochemical sensing. Voltammetric techniques employed by these sensors are particularly useful for identifying and quantifying the valence states of metals in environmental samples, and they play a crucial role in research on plant hyperaccumulation and broader environmental and health studies.

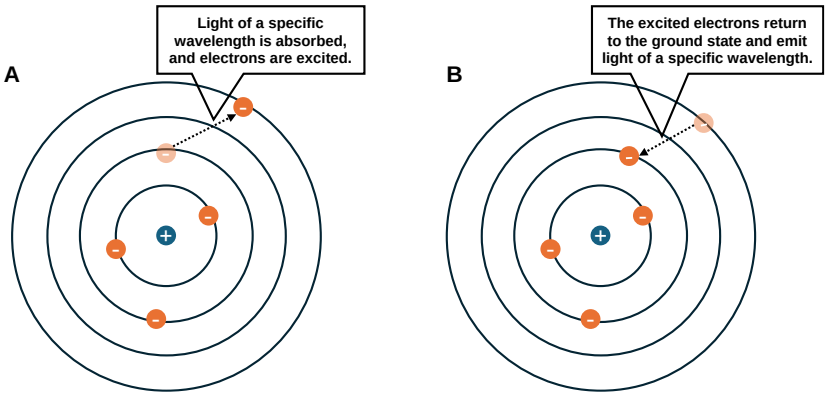

Figure 6. The process of electrons being excited from the ground state to the excited state (A) and back to the ground state (B).

To detect heavy metal ions more quickly and conveniently, researchers have developed many other methods such as electrochemical and optical methods. Since the electrochemical method has been introduced in chapter 1.1.3 and will not be repeated here. Strictly speaking, AAS and ICP-OES are also optical methods, but they are excluded here to distinguish them from conventional optical methods. Usually, metal ions themselves, or after physical or chemical reactions with other substances, develop colors/have specific absorption wavelengths. The color intensity/absorbance of a specific wavelength is related to its concentration within a certain range, so it can be measured by colorimetry with the naked eye or ultraviolet-visible absorption spectroscopy (UV-Vis) [66]. Table 2. shows the comparison of different methods for heavy metal detection, optical and electrochemical are more suitable for on-site analysis as they not only have low LOD for a wide range of analytes but are also more portable and less costly.

Table 2. Comparison of different methods for heavy metal detection.

Parameters/Methods	ICP-OES	ICP-MS	AAS	Optical	Electrochemistry
LOD	ppm	ppt	ppb	ppb	ppt
Analysis range	ppm- %	ppt- ppb	ppb- ppm	ppb- %	ppt- %
Valance distinction	No	No	No	Yes	Yes
Isotope analysis	No	Yes	No	Yes	No
Cost	Upper medium	High	Medium	Low- Medium	Low- Medium
Instrument requirement	Large-scale instrument	Large-scale instrument	Large-scale instrument	Portable device	Portable device
Analysis elements at the same time	Multiple	Multiple	Single	Multiple	Multiple
Reference	[67]	[67]	[67]	[66, 68]	[69-71]

2.2 Palladium and detection of palladium

Palladium (Pd) is considered the most valuable metal out of the four major precious metals, with an acute worldwide resource shortage driving prices to a new height. So far, more than half of the palladium supply has been used for the preparation of catalysts, especially in the pharmaceutical industry [72-75]. According to the World Health Organization (WHO), the median lethal dose (LD_{50}) values for palladium compounds range from 3 to > 4900 mg/kg body weight [76]. Furthermore, some palladium compounds have been found to cause allergic dermatitis, and very low doses of Pd (such as Pd^{2+}, Pd-based complexes, and Pd-based nanoparticles) were sufficient to induce allergic reactions in susceptible individuals [77, 78]. Therefore, from the environmental, health, or cost perspectives, the monitoring of palladium concentration in wastewater is particularly important for assessing the toxicity of the discharge, as well as for adjusting the composition of the reducing agent in the efficient recovery of palladium as a valuable precious metal [79-81].

Electrochemical methods received widespread attention in recent decades, due to their low cost, portability, simple operation, and high sensitivity [82, 83]. However, compared with other heavy metals (such as lead, mercury, cadmium, chromium, and nickel), palladium ions are rather limited to being detected using electrochemical sensors. In early reports, mercury-containing electrodes such as hanging mercury drop electrodes and silver amalgam film electrodes were applied to detect Pd^{2+} [84-86], and those electrodes were gradually replaced by

screen-printed carbon, carbon paste, and glassy carbon electrodes [87-89]. Since unmodified carbon electrodes were characterized by high LOD (~140 ppb Pd^{2+}), modifications of electrodes by complexing reagents (e.g., dimethylglyoxime (DMG)) or bismuth (e.g., bismuth film) were introduced [87, 90]. By introducing complexing reagents, the detectable electrochemical signal shifted from the previous redox signal of Pd^{2+} to the redox signal of Pd complexes (e.g., Pd-DMG complex), which are easier to detect than the free Pd^{2+} ion. However, as many palladium catalysts that participated in the catalytic reactions were in the form of Pd^{2+} complexes [91], it is necessary to consider whether the modified complexing reagent would be affected by the endogenous complexing reagent in the real samples. The common pretreatment methods to release free palladium ions (Pd^{2+}) before subsequent detection, such as microwave acidic digestion and ultraviolet mineralization, require additional apparatus and increase the measurement time [92, 93]. Therefore, a more rapid and straightforward pretreatment method was also desired for on-site palladium (Pd^{2+}) detection.

Furthermore, it has been found that bismuth-based electrode materials are much safer and more sustainable alternatives to traditional mercury-based materials, which also offer the advantages of low background current and favorable potential windows [94-96]. Among the bismuth-based materials, nanosheet-shaped bismuth has been used in electrochemical-related applications, due to their excellent electrochemical performances and strong adhesion to the electrode surfaces [97, 98]. The synthesis of bismuth nano-film materials mainly consists of template method, electrochemical synthesis, and hydrothermal synthesis [99-101]. Notably, all these aforementioned methods require a large number of halogens (chlorine and iodine) or metalloids (selenium and tellurium) during the material synthesis [102-104]. For high-sensitive electrochemical sensors, the background signal generated from the electrode modification should be as low as possible. Reducing or eliminating electrochemical-active moieties (iodine, selenium, and tellurium) would benefit electrochemical sensor design.

2.3 Chromium and detection of chromium

Chromium has been widely used in metallurgical industries, e.g., manufacturing and polishing of steel, stainless steel, and other nonferrous metals, alloying and electroplating, as well as in chemical industries, e.g., leather tanning and finishing, dyes and mordants, pigments, paints, oxidants, catalysts, colored glass, adhesives, and wood preservatives [105-108]. In general, chromium in the environment usually exists in two oxidation states: Cr(III) and Cr(VI) [12, 109-111], and they exhibit pronounced toxicity differences. Cr(III) ion shows low toxicity because it cannot pass through the cell membranes by forming an octahedral coordination moiety. In fact, it has been proven to be an essential micronutrient for living organisms [64, 112-116]. For example, adults need about 50 to 200 mg of Cr(III) daily as an auxiliary factor for insulin to regulate sugar levels [62]. Therefore, Cr(III) has been a nutrient additive in certain foods and health products. However, the toxicity of Cr(VI) is approximately 100 to 300 times that of Cr(III) [117, 118]. The pronounced toxicity is probably due to its strong ability to penetrate biofilms, interfere with the transcription process of DNA, and cause chromosome aberrations and cancer [119, 120].

Chromium that can be in direct contact with the human body is usually found in dental alloys and jewelry [121-123]. These products may undergo corrosive oxidation when in contact with body fluids, such as sweat and saliva, and thus, part of the chromium can be released into the aqueous environment (body fluids) in the form of ions. In laboratory and industrial processes, sulfuric acid acidified potassium dichromate solution (also known as sulfochromic mixture) is usually used for pretreatment of polymer electroless plating, SiO_2 coating and glassware washing [124-126]. The wastewater from these processes, when improperly treated or discharged, may cause serious environmental pollution. Both the International Agency for Research Cancer (IARC) and the United States Environmental Protection Agency (USEPA) consider Cr(VI) to be a human carcinogen [63]. The Brazilian National Council for the Environment (CONAMA) stipulated that Cr(III) and Cr(VI) discharged into water bodies cannot exceed 1

ppm and 0.1 ppm, respectively. In Japan, the total chromium and Cr(VI) discharged by wastewater must not exceed 0.5 ppm and 50 ppb, respectively [127, 128]. In drinking water, the maximum allowable amounts of total chromium given by USEPA and WHO are 100 ppb and 50 ppb, respectively [112]. In general, it is unreasonable to use the total chromium content alone to define the maximum allowable concentration standard for evaluating chromium's actual environmental impact. Therefore, it is necessary to distinguish between these two chromium oxidation states when measuring environmental pollution in various samples.

The standard/conventional methods for chromium content detection include diphenyl carbazide colorimetric method (DCC), AAS and ICP-OES/ ICP-MS [64, 129, 130]. For DCC, a lot of organic reagents are required [64]. While AAS and ICP-OES/ICP-MS can only be used to detect the total chromium content without distinguishing different Cr species. Therefore, ion chromatography (IC) or HPLC had been applied to separate different Cr species, before the detection by ICP-OES/ ICP-MS and AAS [63, 131]. Although some of those standard/conventional methods provide very low detection limits, they require trained expert to complete complicated operations and the use of bulky instruments, which are high cost, inconvenient, and unfeasible for on-site measurement of pollutants. Therefore, a simple, low cost and highly sensitive detection method that can be combined with a portable detector is highly desired for simultaneous determination of Cr(III) and Cr(VI) in various samples.

Electrochemical sensors possess the desired characteristics for on-site measurement [132]. However, when considering these sensors, almost entire attention is focused on Cr(VI) detection. Although some literatures claimed to use electrochemical methods to detect Cr(III), most of them are actually back calculated by measuring the Cr(VI) content after and before oxidizing Cr(III) to Cr(VI) [133-135]. Such indirect determination is rather inconvenient and is expected to be highly interfered by Cr(VI). So far, only small number of scientific reports could "truly" detect Cr(III) directly by electrochemical method [136, 137].

In some previous works, gold was used as an electrode material for electrochemical detection of Cr(VI), but its response to Cr(III) was very poor [136, 138-140]. Welch et al. found that gold oxides could electro-catalyze the oxidation of Cr(III) to produce an electrochemical response, which provided a new approach for detection of Cr(III) [141]. As it is well known, Au (0) is a chemically extremely stable substance. Correspondingly, Au (I/III) oxides are unstable, which can be easily reduced to elemental gold under heat, in the presence of reducing agents or ultraviolet radiation [142, 143]. Therefore, it is crucial to obtain stable Au (I/III) as sensor materials.

2.4 Arsenic and detection of arsenic

Arsenic is considered one of the most hazardous elements within the environment due to its high toxicity [144]. Besides natural phenomena such as mineral leaching and volcanic emissions, industrial activities, including mining, chemical production and utilization, and operations within the glass and ceramic industries contribute to pollution by As [9, 145-147]. Both WHO and USEPA have set stringent guidelines for the total acceptable As content in wastewater discharge and drinking water, with limits set at less than 0.2 ppm and 10 ppb, respectively [148]. Notably, the toxicity of As varies according to its valence. In general, trivalent As exhibits a higher degree of toxicity compared to pentavalent As [9, 148]. Inorganic As mainly exists in the form of arsenate (As(V)) and arsenite (As(III)), being prioritized on the pollutants list of USEPA. Furthermore, As is categorized as a Group 1 carcinogen, denoting its well-established capacity to induce cancer [144]. Given these factors, it is imperative to be able to discriminate between distinct As species.

Conventional methods for As quantification rely on bulky and expensive instruments, such as ICP-OES/MS and AAS, which primarily detect total As content [149, 150]. Notably, ICP-MS, and in particular, triple quadrupole ICP-MS (ICP-QQQ), stands out for its exceptional accuracy, high sensitivity, and minimal background interference in As analysis [151]. For speciation purposes,

HPLC is favored for separating As species in liquid matrices like wastewater, owing to its appropriate flow rate, reduced matrix effects, and superior separation efficiency [149]. The integration of HPLC with ICP-MS provides comprehensive insights into the identification and characterization of As species. HPLC-ICP-MS, utilized in approximately 65% of related studies, is widely regarded as the preferred technique [152]. Consequently, the most sophisticated HPLC-ICP-QQQ method was employed as the benchmark in this study to validate the performance of the newly developed sensors, ensuring their accuracy and reliability.

While conventional methods were recognized for their low limits of detection (LODs), they faced significant challenges for rapid on-site detection of As, including high costs, limited flexibility, and prolonged analysis times. Consequently, there was a growing demand for the development of simpler, more portable, and cost-effective techniques for rapidly and accurately detecting trace As levels. Electrochemical methods, notably DPV, garnered interest for their ability to detect heavy metals and metalloids at trace concentrations, offering an enhanced signal-to-noise ratio compared to other voltammetric techniques [153]. However, as highlighted in recent reviews, while voltammetric sensors demonstrate extremely low LODs for As(III) and As(V) individually, the presence of one species can significantly interfere with the quantification of the other, limiting their applicability in samples containing both species [154, 155]. Furthermore, As(V) presents additional reduction challenges compared to As(III) [155, 156]. To address these issues, reducing agents such as sodium sulfite (for pre-treatment) and manganese (Mn, for in-situ reactions) are employed to convert As(V) to As(III) [157, 158]. As shown in Figure 7., Kristoff et al. found that Mn(0) could reduce As(V) to As(III) through a chemical reaction process (reaction 2) [159]. Based on the theory, the stripping voltammetry method was established. Mn ions were reduced to metallic manganese Mn(0) under a highly negative potential (reaction 3) to facilitate the reduction of As(V) to As(0). Consequently, an anodic sweeping is applied to oxidize As (0) to As(III) (reaction 4) for the

quantification [157]. Apparently, the method suffers from the As(III) originally existed in the samples. As a result, additional steps, such as oxidizing all As(III) to As(V) prior to testing, are necessary.

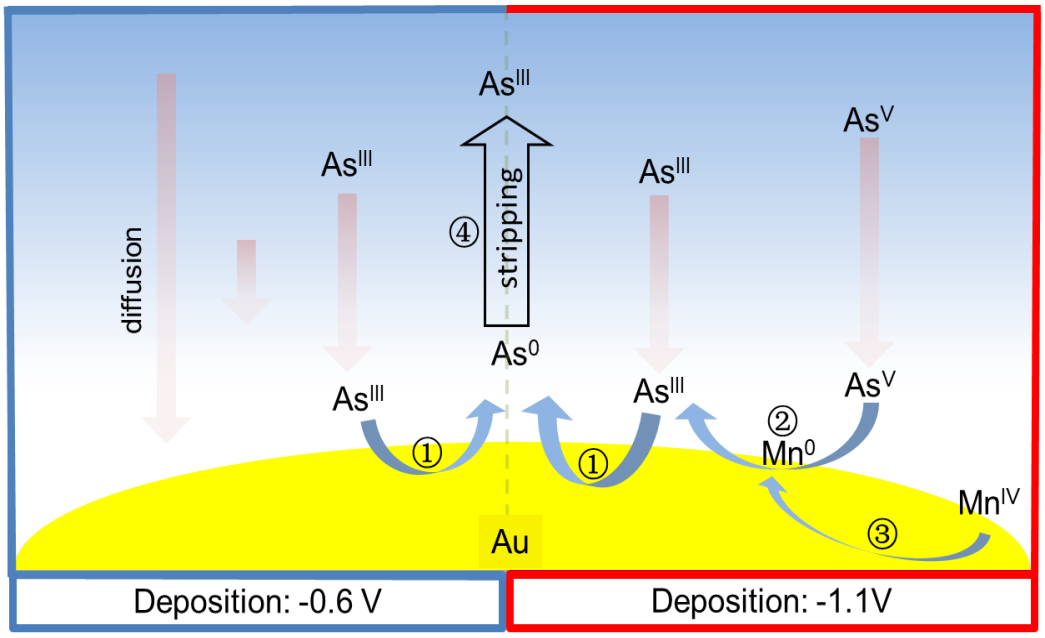

Figure 7. Principle of detection of total As and As(III).

Elza *et al.* introduced a multi-step process based on a similar principle, which could determine the concentration of As(V) directly when the As(III) to As(V) ratio is not greater than 1 [160]. Due to the different reduction mechanisms of As(III) and As(V), the separated calibration curves for both were established, and speciation of As was performed via the standard addition method or applying a masking agent to mask the signal from As(V) [153, 161].

Previous studies reported the electrochemical deposition of manganese on a gold surface typically resulted in a coverage rate of less than 14% [159]. Externally synthesized manganese-gold complexes were also investigated, where the coverage rate of Mn on gold would not be limited. However, these complexes would be mostly applied to detect a single As species [162, 163]. Thus, it is paramount to develop and optimize manganese/gold hybrid materials for direct speciation of inorganic As.

2.5 Leaching and detection of heavy metals from solid waste

As the global population continues to grow, alongside global urbanization, significant environmental challenges arise, particularly connected to the management of solid waste [164]. It is estimated that by 2025, solid waste generation will reach more than 3.4 billion tons, with approximately 70% of waste destined for landfills [165]. Solid waste often contains complex and toxic substances, particularly heavy metals and metalloids, necessitating waste assessments before landfilling. TCLP is a widely adopted standard protocol for evaluating whether solid waste materials are classified as hazardous or non-hazardous under simulated landfill conditions [166]. According to USEPA and Singapore regulations, waste can only be landfilled if it meets TCLP criteria [167, 168]. However, the TCLP process requires 18 hours for heavy metals and metalloids leaching. Moreover, it relies on large, bulky, and costly instruments, such as ICP-OES and ICP-MS, for further heavy metal and metalloid analysis, making it impractical for rapid on-site applications [169, 170].

Pyrolyzing biomass into biochar has been recognized as an effective strategy for combating global warming [171]. Due to its excellent specific surface area, porosity, electrochemical activity, catalytic properties, biochar has been found in a wide range of applications [172]. For example, biochar has been extensively used for heavy metal and metalloid treatment in various applications, including wastewater treatment, soil remediation, gas purification, heavy metal and metalloid adsorbents, metal-reducing agents, and even biogas production [173-179]. However, when biochar is employed for heavy metal and metalloid treatment, it becomes contaminated, requiring disposal or landfilling under stringent environmental standards [180, 181].

Given that current methods for leaching and analyzing heavy metals and metalloids in contaminated biochar and other solid waste materials are often slow, costly, and labour-intensive, there is an urgent need for innovative, cost-effective, and high-performance solutions that can deliver rapid and reliable on-site analyses directly at waste management sites. Ultrasound technology has been

explored as an auxiliary energy source to accelerate leaching processes [182, 183]. In our previous study, it was demonstrated, based on ash samples that the combination of ultrasound with a tumbler could significantly reduce leaching time without compromising the accuracy of results compared to TCLP [184]. Building on this, a portable leaching device incorporating ultrasonics was developed to eliminate the need for bulky equipment, making it a practical and efficient solution for rapid on-site testing [185]. The UAL could accelerate the leaching process by utilizing ultrasound to enhance mass transfer and disrupt particle structures, thus significantly speeding up the leaching of heavy metals and metalloids. For the rapid detection of heavy metals and metalloids, voltammetric sensors have gained attention due to their portability, ease of use, quick response, and high sensitivity to various heavy metal and metalloid ions [186]. Each heavy metal or metalloid ion produces a distinct current peak, allowing precise concentration determination through previously prepared sensor calibration. Furthermore, voltammetric sensors can differentiate between oxidation states of certain heavy metal and metalloid ions, a task that traditionally requires multiple instruments like HPLC coupled with ICP-MS [187, 188].

CHAPTER 3 SYNTHESIS OF ELECTROCATALYTICALLY ACTIVE BISMUTH OXIDE NANOSHEETS FOR DETECTING TRACE PALLADIUM IN PHARMACEUTICAL WASTEWATER

3.1 Introduction

Palladium is one of the precious metals which has wild applications, including catalysis, electronics, and the manufacturing of hydrogen storage materials [189-191]. The increasing demand for palladium in catalytic converters and renewable energy technologies, coupled with its limited natural availability, has necessitated the development of highly sensitive and selective detection methods[192]. Additionally, the potential toxicity of palladium ions in biological and environmental systems underscores the importance of monitoring its presence at trace levels [193]. Voltammetry sensors was found suitable to perform real-time analysis of Pd ions but many of them require complex compound which make the manufacturing cost of sensors high [194].

Herein, a new, facile and low-cost method for synthesizing bismuth oxide (Bi_2O_3) nanosheets (BiONS) without adding halogens or metalloids was developed. The synthesized BiONS were modified onto SPCEs and then successfully applied to monitor the Pd^{2+} concentrations in pharmaceutical wastewater after the palladium recovery process for the first time. Finally, an optimized palladium recovery process was also proposed for pharmaceutical wastewater samples.

3.2 Experimental

3.2.1 Materials and reagents

All the chemicals and solvents used in the study were analytical grade and high purity. Sodium hydroxide (NaOH), sodium borohydride ($NaBH_4$), acetic acid (HAc), sulfuric acid (H_2SO_4), bismuth(III) nitrate pentahydrate ($Bi(NO_3)_3 \cdot 5H_2O$), perchloric acid ($HClO_4$), potassium chloride (KCl), sodium arsenate

($Na_3As(V)O_4$), sodium arsenite ($NaAs(III)O_2$) and individual elemental standards (Pd(II), Pb(II), Cd(II), Zn(II), Cu(II), Ni(II), Cr(III) and Cr(VI)) for ICP-OES were bought from Merck Pte. Ltd (Singapore). Ethylene glycol (EG) was from Sinopharm Chemical Reagent Co., Ltd (China). The wastewater samples containing palladium were obtained from a local pharmaceutical company. Deionized water (DI water, resistivity of 18.2 MΩ·cm) obtained from a Millipore Milli-Q purification system was used in all experiments.

3.2.2 Apparatus

SPCEs (DRP-C110, Metrohm) were used for further modification. DPV was performed by a multi-potentiostat (μstat8000p, Metrohm). The crystalline phase of synthesized BiONS was investigated by powder X-ray diffraction (XRD, AXS D8 diffractometer, Bruker) with Cu Kα radiation. Raman spectroscopy was recorded by a Raman spectrometer (Raman, XploRA™ PLUS, HORIBA Scientific). The speciation of bismuth was identified by an X-ray photoelectron spectrometer (XPS, AXIS Supra, Kratos Analytical Ltd.). The XPS spectra were deconvolved using CASA XPS software after the correction for binding energies of all elements against the adventitious carbon C 1s core level (285 eV). The morphology of the materials and the elemental distributions were investigated by field emission-scanning electron microscopy (FE-SEM) equipped with energy dispersive X-ray (EDX) spectroscopy (JSM-7200F, JEOL Ltd.) first, and then the transmission electron microscopy (TEM, JEM-1400Plus, JEOL Ltd.). The thickness of BiONS was measured by an atomic force microscope (AFM, Park NX10, Park Systems). The quantitative elemental composition and total organic carbon (TOC) in wastewater samples were detected by an ICP-OES instrument (OPTIMA 8300, PerkinElmer) and total organic carbon analyzer (TOC, TOC-L, Shimadzu), respectively.

3.2.3 Synthesis of Bi_2O_3 NS and modification of working electrode

Operationally, $Bi(NO)_3 \cdot 5H_2O$ (0.5 g) was weighed in a glass beaker and

dissolved with 20 mL EG. $NaBH_4$ (0.3 g) was weighed in another beaker and dissolved in 10 mL EG. The two solutions were mixed and placed into a water bath (90°C) while continuously stirring for 80 min. After filtration, the precipitate was simply washed with DI water, followed by ethanol, and then dried at 90°C in an oven overnight to obtain BiONS.

Different amounts of BiONS suspension were weighed and dispersed into DI water, and then sonicated for 10 min to make them evenly dispersed without visible particles or precipitates. The well-dispersed BiONS suspension (10 μL) was used as a modifier to drop onto the working electrodes (WEs) of SPCEs, then dried at 105°C in an oven for 5 min. Finally, the modified electrodes were labeled as BiONS-SPCEs.

3.2.4 Electrochemical measurements

After the preliminary investigation, a buffer solution containing HAc and KCl was used to adjust the pH of Pd^{2+} samples. Parameters, including buffer pH, buffer concentration, modifier amount, deposition potential, and deposition time, were systematically optimized for Pd^{2+} detection. The final measurement protocol was as follows: (i) 100 μL of different concentration Pd^{2+} standard solutions dissolved in 0.1 M acetate/1M KCl buffer (pH 4.0) were dropped onto the previously modified SPCEs with 10 μL of 0.1 mg/mL BiONS; (ii) the samples containing traces of palladium were preconcentrated by applying a potential of -0.8 V on the WE for the duration of 120 s; and (iii) followed by DPV measurement with the potentials from -0.8 to 0.8 V, and the step potential, the pulse potential, the pulse time and scan rate were set at 0.008 V, 0.05 V, 0.08 s and 0.02 $V \cdot s^{-1}$, respectively. All experimental conditions were consistent according to the introduced measurement protocols. The recorded data were processed with DropView 8400 Software. The mean values and standard deviations (SDs) of all the data were obtained from the triplicate measurements.

3.2.5 Interference caused by the presence of other metal ions

Since BiONS-SPCEs were applied to detect Pd^{2+} concentrations in real wastewater samples with complicated matrices, it was necessary to examine the extent of interference between Pd^{2+} and other metal ions in the electroanalysis of palladium. The raw pharmaceutical wastewater sample (S1) was analyzed by ICP-OES for other endogenous metals and metalloids. In addition, to study the effect of other common heavy metals and metalloids, 100 ppb Pd^{2+} standard solutions were spiked with several other metal or metalloid ions (including Pb(II), Cd(II), Cu(II), Ni(II), Cr(III), Cr(VI), Zn(II), As(III) and As(V)) by diluting the standards in 10- and 100-fold concentrations. The electrochemical signals of the spiked samples were detected by BiONS-SPCE with the same optimized parameters and compared to those of the unspiked samples.

3.2.6 Pd recovery and sample pretreatment for electrochemical detection

A simulated Pd recovery process using $NaBH_4$ as a reducing reagent was performed. The raw sample (S1) was treated using $NaBH_4$ during the palladium recovery processes, namely: 100 µL of 0.1 g/mL $NaBH_4$ was added into 10 mL of raw sample (S1); placed into an oven at 80°C for 30 min and then filtered, the filtrate was labeled as sample S2; and 200 µL of 0.1 g/mL $NaBH_4$ was added into 10 mL of raw sample, placed into an oven at 80°C for 30 min and then filtered, the filtrate was labeled as sample S3.

For sample pretreatment prior to electrochemical detection, a mixture of perchloric acid (60%) and sulfuric acid (98%) was prepared in a volume ratio of 1:2 to create Mixed Acid 1. This acid mixture was then combined with the sample in a 1:9 ratio and heated at 80°C for 10 minutes. Following acid treatment, the samples were neutralized using a buffer solution composed of 0.1 M acetate and 1 M KCl, adjusted to pH 4.0, to meet the optimal conditions for electrochemical analysis using BiONS-SPCEs. All the samples were also tested by ICP-OES to verify the accuracy of results obtained using BiONS-SPCEs.

3.2.7 Optimization of Pd recovery process

After the verification, the BiONS-SPCEs were further applied to optimize a new palladium recovery process for another batch of wastewater sample from the same company, namely the raw sample (S4) was transferred into 4 centrifuge tubes (10 mL each); 0.25, 0.30, 0.35 and 0.40 mL of 0.01g/mL $NaBH_4$ solutions were added into the 4 tubes, and they were labeled as samples S5, S6, S7 and S8, respectively. These samples were pretreated and tested by BiONS-SPCEs using the same method as described in Section 3.2.6.

3.3 Results and discussion

3.3.1 Material characterization

Raman spectra (Figure 8 a) revealed that the synthesized material was composed predominantly of β-Bi_2O_3 and a low amount of α-Bi_2O_3. Peaks at 91.6, 123.6, and 310.9 cm^{-1} were attributed to β-Bi_2O_3, while the minor peaks at 222.5 and 450.3 cm^{-1} were attributed to α-Bi_2O_3 [195, 196]. Figure 8 b shows that the crystallinity of the product was rather low, possibly due to the lower synthesis temperature [197]. By comparing with standard PDF cards (PDF#41-1449 for α-Bi_2O_3 and PDF#27-0050 for β-Bi_2O_3), it could be found that the synthesized bismuth oxide was a mixture of α-Bi_2O_3 and β-Bi_2O_3[198-200]. Similarly, the main crystalline phase was β-Bi_2O_3, and thus the results of XRD and Raman were found to be consistent. From Figure 8c, the peak areas of Bi 4f (blue dashed frame) and O 1s (red dashed frame) could be calculated. Based on the peak areas, the atomic ratio of Bi to O was approximately 2 to 3, which confirms the chemical formula as Bi2O3. The binding energies of the Bi 4f 7/2 and Bi 4f 5/2 peaks were 164.4 eV and 159.1 eV, respectively (Figure 8d). A difference in the binding energy of about 5.3 eV between these two peaks indicates that the bismuth existed in the form of Bi^{3+} [201, 202]. Meanwhile, no elemental bismuth peak was found, indicating that $NaBH_4$ was not strong enough to reduce Bi^{3+} in the EG solution.

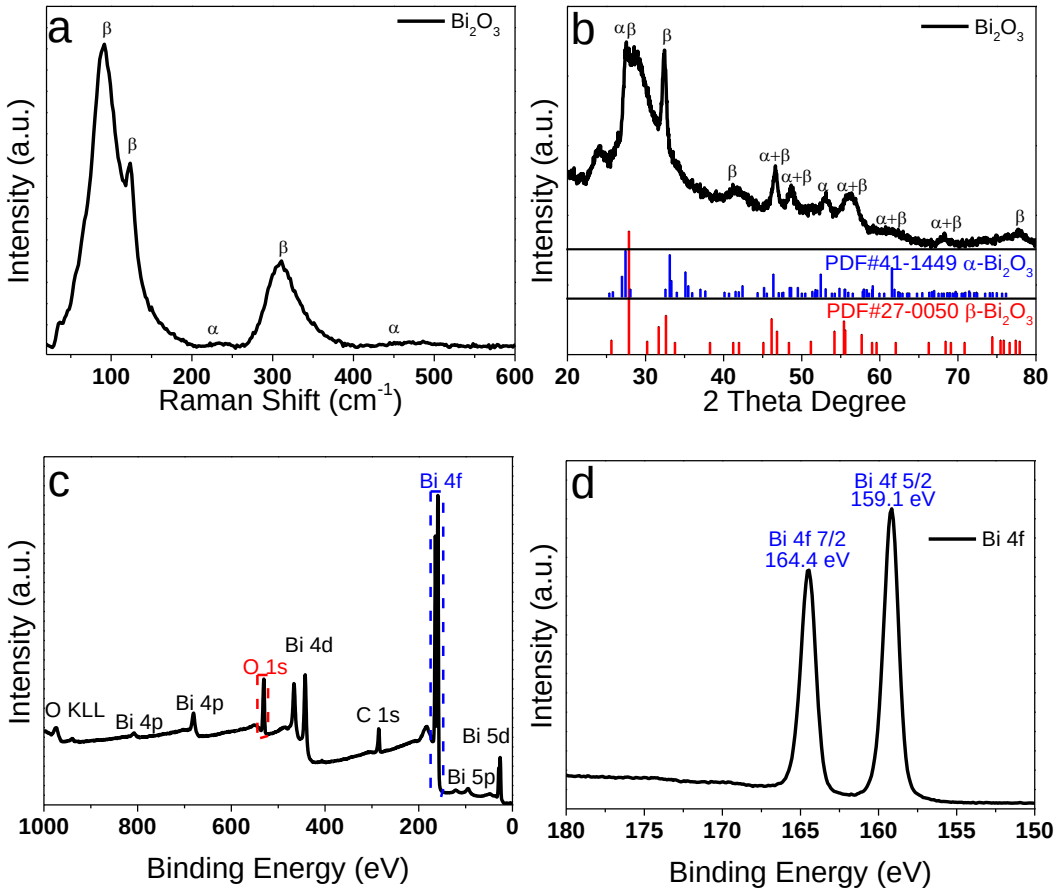

Figure 8. Raman spectrum (a), XRD pattern (b), and XPS spectra (c: wide scan and d: Bi 4f narrow scan) of the prepared BiONS.

The SEM images, as illustrated in Figure 9 a and b, showed that most of the Bi_2O_3 NS were flakes, which were redistributed at the electrode surface. The corresponding EDX spectrum confirmed that the flakes were bismuth oxide. The TEM image (Figure 9. d) clearly showed that the width of these nanosheets was about 300-1000 nm. In addition, the transparent nature of BiONS also indicated that their thickness was minimal, which was measured by AFM. For AFM, BiONS were evenly dispersed at low content on a flat silicon substrate, allowing for scanning a single BiONS. The thickness was determined by measuring the height of the BiONS, which was found to be 8.09 ± 1.36 nm/6-10 nm (Figure 10 and Figure 11). Yang et al. reported chloride-containing bismuth oxide nanosheets with a thickness of around 100 nm, and Han et al. reported bismuth

oxyiodide (BiOI) nanosheets with a thickness of about 8.7 nm [103, 104].

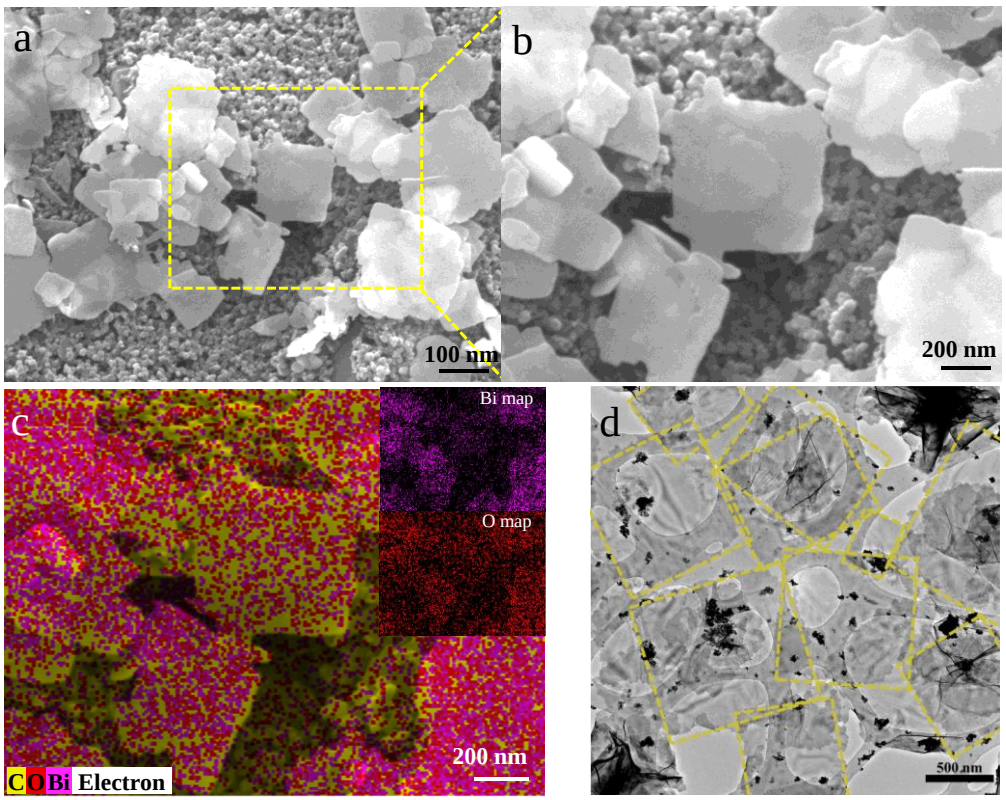

Figure 9. SEM images (a and b), SEM-EDX layered elemental mapping (c, inserts: elemental mapping images of Bi and O), and TEM image (d) of the prepared BiONS.

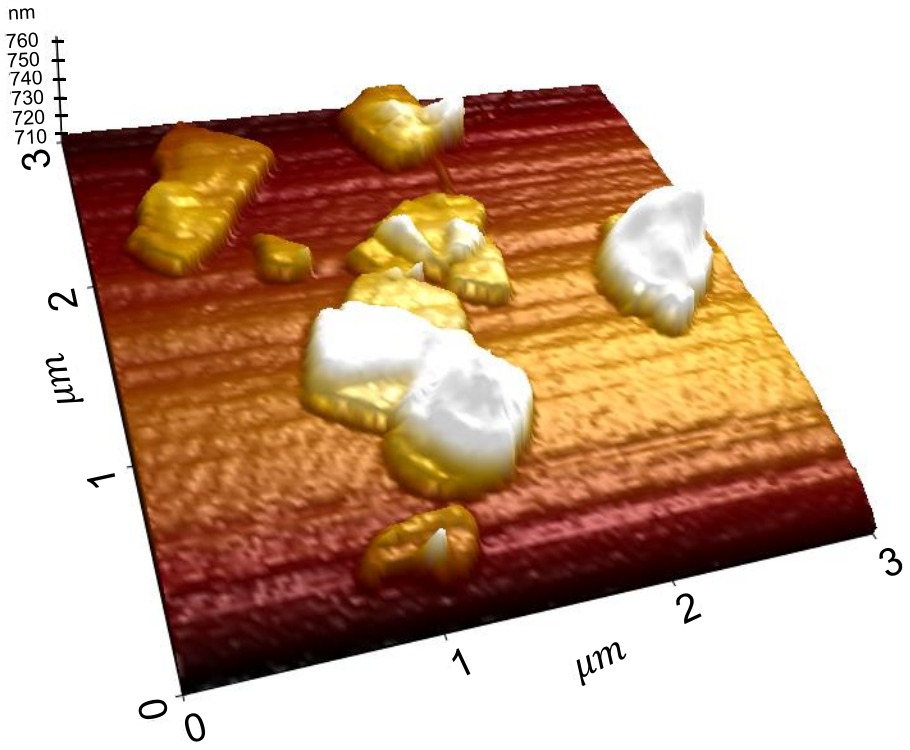

Figure 10. Tapping mode 3D AFM image of the prepared BiONS.

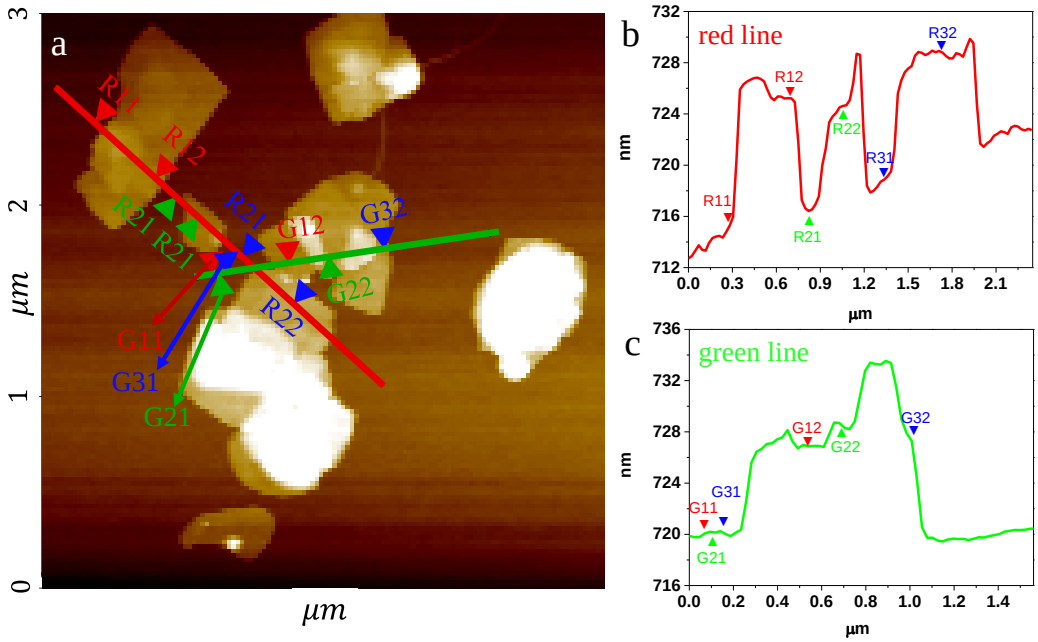

Figure 11. Tapping mode 2D AFM image of the prepared BiONS (a) and marks of selected points to measure the thickness (b and c).

3.3.2 Electrochemical detection of Pd^{2+} in standard solutions

The Pd^{2+} detection was optimized by performing electrochemical measurements in 100 ppb Pd^{2+} standard solution with changing buffer pH, the concentration of KCl in buffer, the concentration of Bi_2O_3 used for electrode modification, deposition potential and deposition time and comparing the oxidation peak heights of previously deposited Pd at around +0.28 V. From Figure 12 a, the peak height firstly increased with the change of pH from acidic to more basic, reaching a maximum at pH 3-4. Then, the peak height decreased when the pH was changed to 5 and 6. This behavior might have been due to the dissolution of BiONS at low pH, and the precipitation of Pd^{2+} at high pH [203, 204], and thus the pH for subsequent measurements was fixed at 4.0. Another phenomenon observed here was that the SDs at lower (1.0-2.0) and higher pH (6.0) appeared to be lower than those at the pH of 3.0, 4.0, and 5.0. The possible reasons include: (i) As BiONS were fully dissolved at lower pH, there was actually the performance of bare carbon electrode in the pH of 1.0-2.0; (ii) As Pd^{2+} was almost fully precipitated at higher pH, the signal was basically only the background noise in the pH of 6.0; and (iii) As the amount of BiONS was much lower than the optimized amount, the BIONS layer could be easily affected.

Pd^{2+} can form a stable square-planar configuration complex with Cl^-, namely $[PdCl_4]^{2-}$ [205, 206]. Herein, it was found that the existence of Cl^- could also enhance the EC signal. Figure 12b shows the current peak of re-oxidation for previously deposited Pd increased with the increasing Cl^- concentration (C_{Cl}), until C_{Cl} reached a concentration of 1 M, and thus the C_{Cl} was fixed at 1 M for subsequent measurements.

Furthermore, in Figure 12c, the amount of BiONS used for the modification of SPCEs also affected the electrochemical performance of the sensor. Firstly, the peak height was negligible when no BiONS was used at the SPCEs, which is consistent with a previous study [90]. After adding a small amount of BiONS (0.1 mg/mL BiONS, Figure 12c), the current peak height increased from 267.9 to

911.8 nA, proving that BiONS played a fundamental role in electro-catalytically enhancing the activity of the electrode towards Pd^{2+} detection. When SPCEs were modified with an even higher concentration of BiONS (1 mg/mL BiONS), the current peak height decreased to 209.0 nA, and the background signal increased significantly. Therefore, the 0.1 mg/mL BiONS were used for SPCE modification in subsequent measurements. During the deposition process, some BiONS could be reduced to Bi(0), with an oxidation peak at ~ -0.2 V during the later electro-oxidization. According to the activity order of the metals, Pd^{2+} was reduced to Pd(0) first, followed by the reduction of Bi^{3+}. For optimization, the Pd2+ deposition potential and time were adjusted in the ranges of -1.0~0.0 V and 60~180 s, respectively (Figure 12 d and e). As expected, lower deposition potential and longer deposition time led to higher peak height. However, when deposition potential was lower than -0.8 V, the current peak height decreased and became unstable (with a greater SD), which was observed probably due to the reduction of BiONS caused by low potentials. Therefore, the deposition potential and time were set for subsequent measurements at -0.8 V and 120 s, respectively.

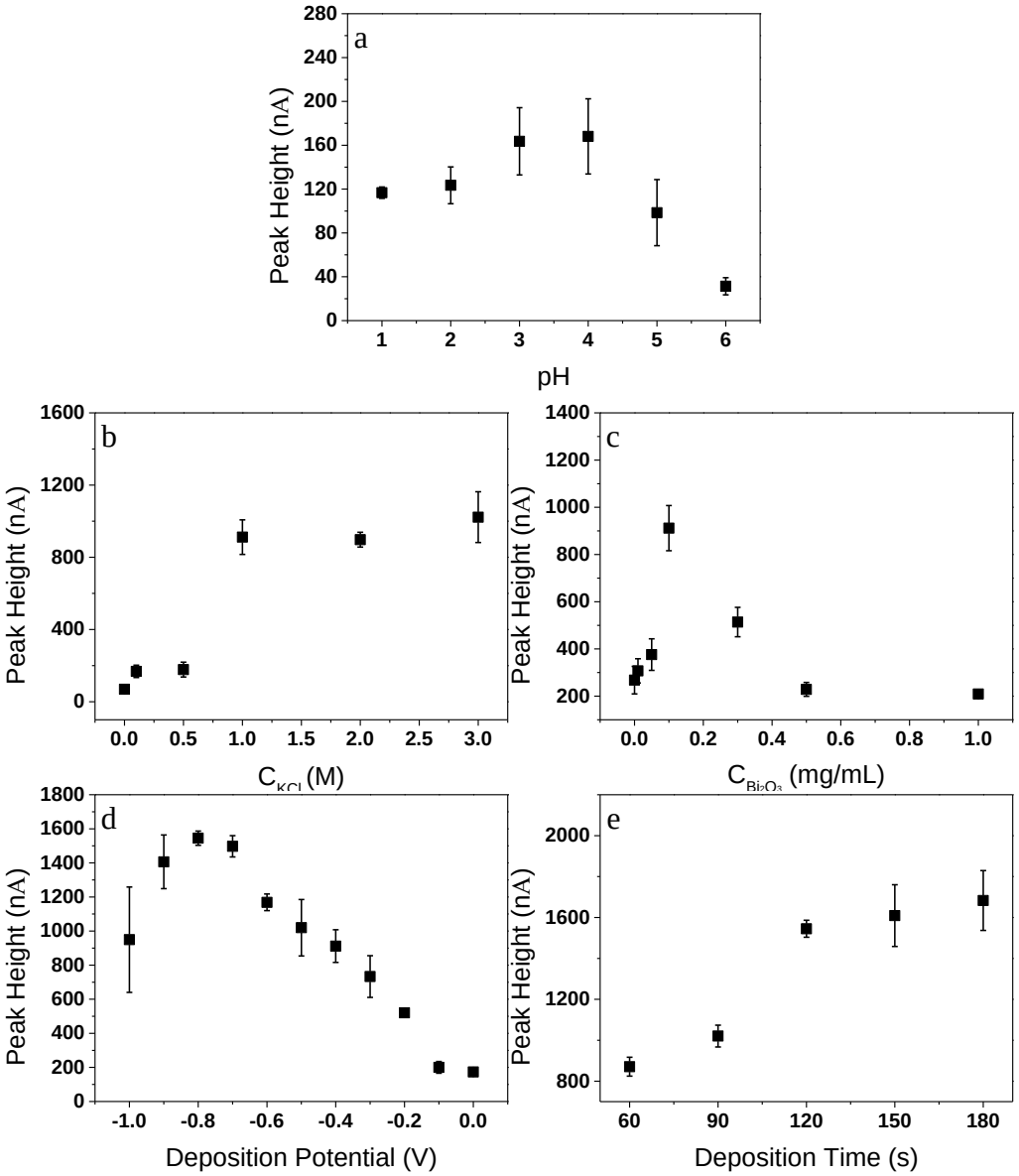

Figure 12. Optimization of parameters for reliable determination of Pd^{2+}: pH of the electrolyte (a), the concentration of KCl in background electrolyte (b), the concentration of BiONS used for modification of SPCEs (c), Pd^{2+} deposition potential (d) and Pd^{2+} deposition time (e).

In addition, the morphology and elemental distribution of the BiONS modified electrode surface were analyzed after the electrochemical deposition of Pd^{2+} (-0.8 V, 120 s). Compared to Figure 9, the originally evenly distributed BiONS were aggregated into micron-sized blocks (Figure 13). At the same time, it was found that palladium was mainly deposited on the newly formed blocks from the

elemental maps. This might have been due to the stronger affinity of palladium to the surface of BiONS than carbon, and the electrodeposited palladium acted as a binder to gather the originally independent BiONS together.

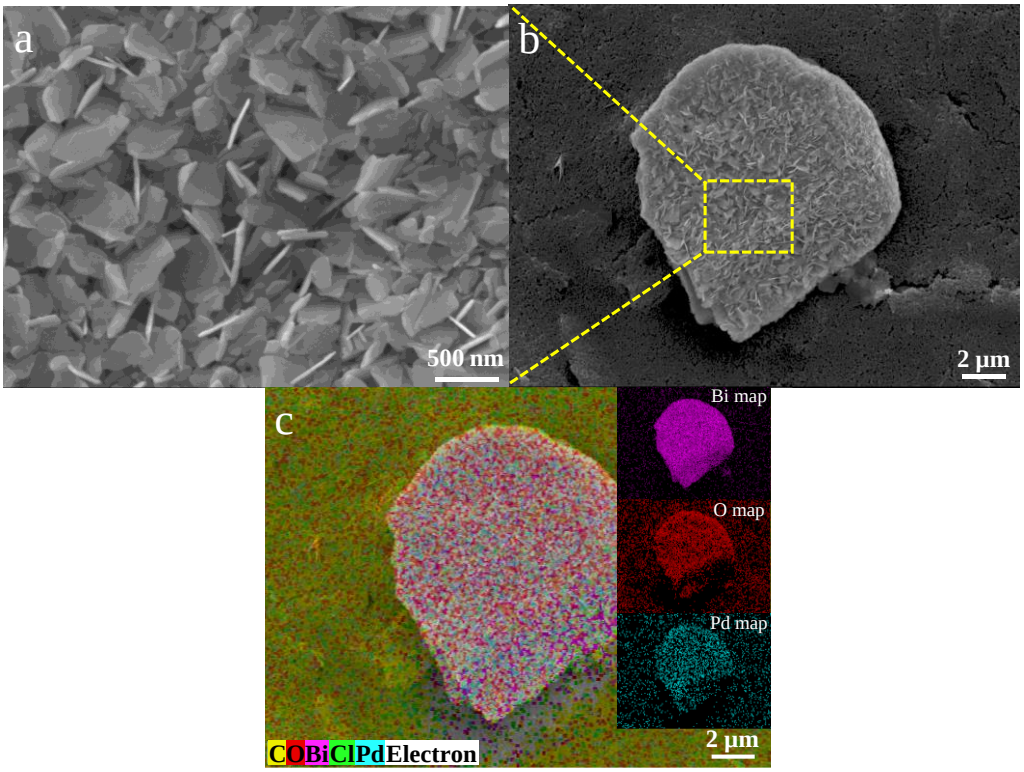

Figure 13. SEM images (a and b) and SEM-EDX layered elemental mapping (c, inserts: elemental mapping of Bi, O and Pd) of the electrode surface after Pd deposition.

Under the optimized conditions, the voltammograms and a linear relationship of the calibration curve are shown in Figure 14. The calibration curve showed good linearity and obeyed the equation: peak height (µA) = 15.622 × concentration (ppb) – 98.37 (r^2 = 0.9985) in the range of 40-400 ppb Pd^{2+}. The LOD was found to be 1.4 ppb Pd^{2+}. A comparison between BiONS-SPCEs and other reported electrochemical sensors developed for the determination of Pd^{2+} was shown in Table 3. The newly developed electrochemical Pd^{2+} sensor provided much higher sensitivity than carbon-based electrodes and was comparable to other complex reagents modified electrodes.

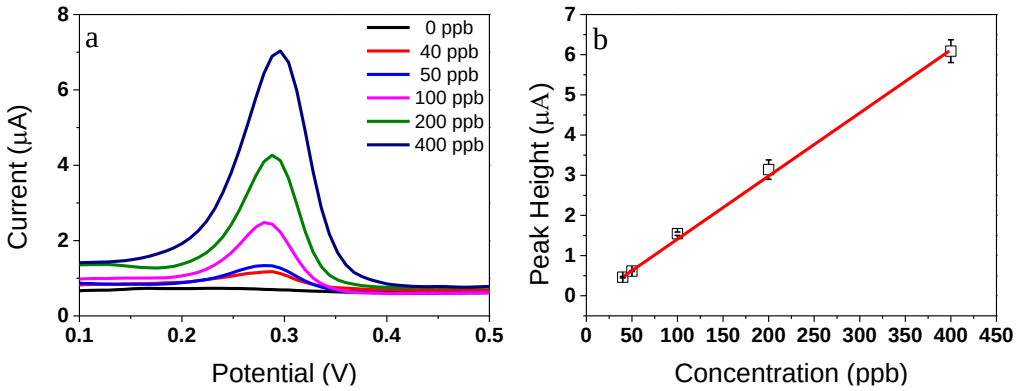

Figure 14. Voltammograms and linear relationship of calibration curve for Pd^{2+} detection.

Table 3. Comparison of results in the present work with other reported electrochemical sensors to determine Pd^{2+}.

Electrode	Linear range (ppb)	LOD (ppb)	Reference
Unmodified SPCE	319 - 14191	140.47	[90]
Dithiooxamidated polysiloxane modified carbon paste electrode	106 - 106400	128.0	[207]
Renewable bismuth bulk annular band working electrode with DMG in buffer	1 - 10 and 10 – 1000	0.12	[93]
Silver amalgam film electrode with DMG in buffer	1 – 50	0.15	[86]
BiONS-SPCE	40 - 400	1.40	This work

* The units were converted to ppb if their original units had been expressed in other forms.

3.3.3 Interference caused by the presence of other metal ions

Since BiONS-SPCEs were applied to detect Pd^{2+} concentrations in real wastewater samples with complicated matrices, it was necessary to examine the extent of interference between Pd^{2+} and other metal ions in the electroanalysis of palladium. The raw pharmaceutical wastewater sample (S1) was analyzed by ICP-OES for other endogenous metals and metalloids. In addition, to study the effect of other common heavy metals and metalloids, 100 ppb Pd^{2+} standard solutions were spiked with several other metal or metalloid ions (including Pb(II), Cd(II), Cu(II), Ni(II), Cr(III), Cr(VI), Zn(II), As(III) and As(V)) by diluting the standards in 10- and 100-fold concentrations. The electrochemical signals of the

spiked samples were detected by BiONS-SPCE with the same optimized parameters and compared to those of the unspiked samples. The results in Table 4 demonstrated that BiONS-SPCEs had a robust electrochemical response towards Pd^{2+} in the presence of other high-concentrated endogenous metals and metalloids. Moreover, the peak height changed after 10- and 100-fold spiked excess concentrations of other metal ions into 100 ppb Pd^{2+} standard solution, as shown in

Table 5. Based on the obtained results, the sensor was found to tolerate higher concentrations of most interfering ions except for Cu(II) and As(III). Notably, the copper peak position is of similar potential as that of palladium (Pd^{2+}). According to several reports, the concentrations of Pb, Cd, Zn, Cu, Ni, Cr and As were in the ranges of <0.002–25.894 ppm, <0.008–12.340 ppm, 0.960-26.21 ppm, 0.100 to 18.342 ppm, 0.300-0.935 ppm, <0.018-17.463 ppm and <0.100-0.830 ppm, respectively [208-210]. Compared to the electrochemical signals of palladium in the current sample, the interferences except Cu(II) and As(III) were considered low. For Cu(II) and As(III), it would be necessary to modify the pretreatment method, if they were in high concentrations. It was reported that gallium could form stable Cu-Ga intermetallic to reduce the interference of Cu(II) on the electrochemical signal [211]. For As(III), advanced oxidation was required to convert As(III) to As(V), and thus, it would hardly affect the detection of Pd^{2+} [212]. In fact, the developed pretreatment method was also an oxidation method, and the As(III) in the samples might be converted to As(V) as well.

Table 4. Contents of other elements in real untreated wastewater sample S1.

Element	Concentration (ppm)
As	1.95
Fe	1.16
Mg	1.64
Ni	0.9
Se	17.55
Si	1207
Zn	0.73

Table 5. Peak height ratio as recorded by BiONS-SPCEs for 100 ppb Pd^{2+} after 10- and 100-fold spiked excess concentrations of other metal ions.

Spiked ion	Peak height ratio (%)	
	10-fold (1 ppm)	100-fold (10 ppm)
Pb(II)	114.3	76.8
Cd(II)	96.7	69.2
Zn(II)	100.4	102.2
Cu(II)	Peaks overlapped	Peaks overlapped
Ni(II)	79.6	63.6
Cr(III)	95.2	78.9
Cr(VI)	92.2	78.1
As(III)	No peak	No peak
As(V)	100.8	100.0

3.3.4 Pd^{2+} concentration monitoring during the Pd recovery process

After the sensor calibration, the BiONS-SPCEs were used to monitor the Pd^{2+} concentration during the palladium recovery process. The exact sample preparation and pretreatment methods were the same as described above. To reflect the necessity of pretreatment, the color change and EC signal comparison of samples before and after pretreatment at the same dilution ratio were shown in Figure 15 and Figure 16. Also, the TOC of the raw pharmaceutical wastewater sample (S1) measured before and after treatment was 7.5% and 6.6%, respectively. The degradation of organic ligands resulted in a TOC decrease, and the remained TOC was from a water-soluble organic solvent [213]. Obviously, when palladium existed in the form of complexes, it was unavailable for the redox reaction at the electrode surface. Therefore, it was necessary to apply the protocol of sample preparation to release bound Pd into ionic form, Pd^{2+}. The comparison of results obtained from BiONS-SPCEs and ICP-OES were shown in Table 6. The data indicated that the developed BiONS-SPCEs sensor was suitable for rapid Pd^{2+} detection in complex industrial wastewater samples, since the results closely matched that obtained by ICP-OES. Moreover, it was also found that as the amount of added $NaBH_4$ increased during palladium recovery, there was a sudden change in the Pd^{2+} concentration. Therefore, monitoring the concentration of Pd^{2+} in the solution would be crucial for efficiently reducing the reagent dosage in pharmaceutical wastewater treatment.

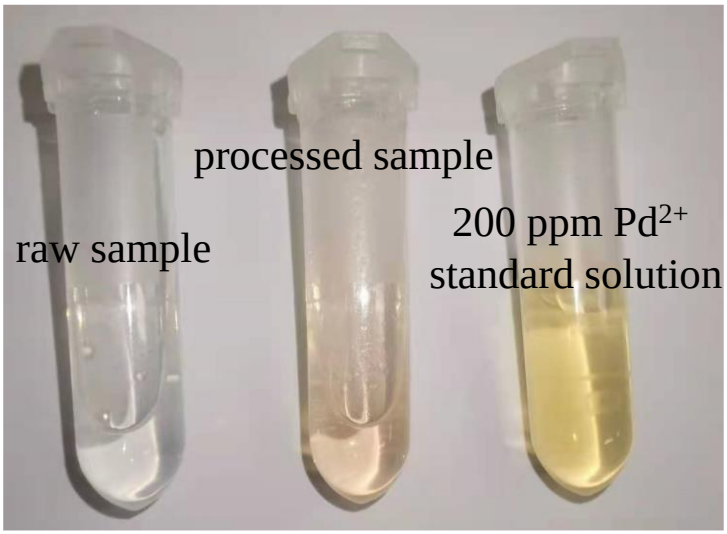

Figure 15. The color change of real wastewater sample before and after pretreatment.

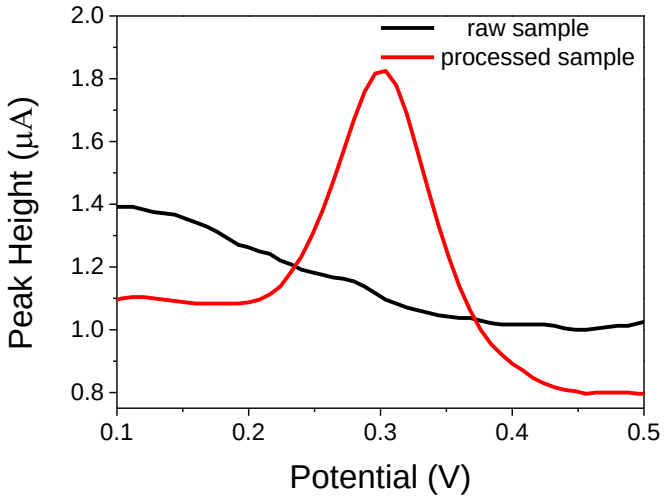

Figure 16. Electrochemical signal comparison of Pd samples before and after pretreatment.

Table 6. Determination of Pd^{2+} in real untreated wastewater and treated wastewater samples.

Sample	S1 (untreated)	S2 (treated)	S3 (treated)
BiONS-SPCEs (ppm)	62.0 ± 2.1	52.0 ± 3.5	below LOD
ICP-OES (ppm)	66.2 ± 2.3	50.6 ± 1.3	below LOD

3.3.5 Monitoring of Pd recovery process using BiONS-SPCEs

The recovered palladium was then filtered out, washed and dried. Figure 17a shows that the recovered palladium appeared as porous nano aggregates. Furthermore, the EDX result (Figure 17b) indicates that the purity of recovered

palladium was as high as 98.8%, which was much higher than that (29.03%) of the reported bio-reduction process [214] and comparable to that (98.8%) of the reported chemical reduction process [215].

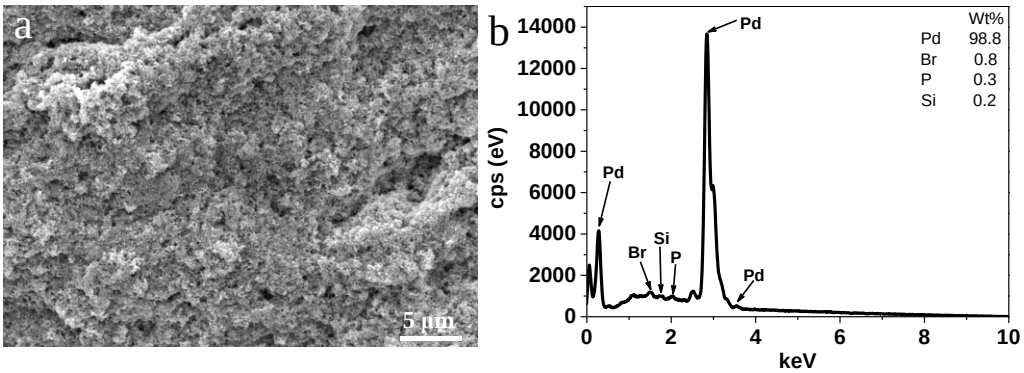

Figure 17. SEM image (a) and corresponding EDX spectrum (b, inset: elemental weight percentage) of the recovered Pd powder.

As shown in Table 7, the sudden change in Pd concentration (S7 to S8) happened again, even when using a small amount and low concentration of $NaBH_4$. Therefore, considering the issue of treatment cost, it is crucial to monitor the residual Pd content in wastewater on-site. With the monitoring of palladium using BiONS-SPCEs, S8 (0.40 mL of 0.01g/mL $NaBH_4$ solutions) was considered the optimized dosage for recovering Pd from 2nd batch of wastewater (10 mL).

Table 7. Pd^{2+} concentrations and recovery rates tested by BiONS-SPCEs during the Pd recovery process.

Sample	Pd concentration (ppm)	Recovery rate [a] (%)
S4	17.5 ± 0.7	0.00
S5	10.5 ± 0.3	39.94
S6	9.0 ± 1.1	48.53
S7	6.9 ± 0.9	60.62
S8	< 1.32 [b]	> 92.47

[a]: Calculated as: recovery rate = (Pd concentration in current sample / Pd concentration in raw sample) × 100%

[b]: As the concentration is lower than LOD, it was calculated as lower than LOD (0.04 ppm) × dilution factor (33 for this sample).

3.4 Conclusion

In this chapter, an innovative method was developed for synthesizing BiONS without adding halogens or doping other metalloids. Raman, XRD, and XPS

spectra showed that the BiONS were mainly β-Bi_2O_3. SEM, TEM, and AFM results confirmed that the BiONS were flake-shaped (300-1000 nm in width), which were ultra-thin (6-10 nm in thickness).

These BiONS were utilized to modify SPCE, leading to the development of a new electrochemical sensor that demonstrated significant electrocatalytic activity towards the redox processes of Pd^{2+}. This sensor exhibited a broad linear detection range from 40 to 400 ppb and a low LOD of 1.4 ppb for Pd^{2+}. Additionally, a rapid and straightforward pretreatment method was developed to decomplex palladium in pharmaceutical wastewater, enhancing the practicality of the sensor.

The combined application of the newly developed sensor and sample pretreatment protocol effectively monitored palladium concentrations during palladium recovery from pharmaceutical wastewater. This breakthrough has the potential to be implemented on-site for near real-time monitoring of palladium content in environmental samples, offering significant techno-economic advantages by improving resource management and recovery processes.

CHAPTER 4 GOLD-SILVER NANOPARTICLES MODIFIED ELECTROCHEMICAL SENSOR ARRAY FOR SIMULTANEOUS DETERMINATION OF CHROMIUM(III) AND CHROMIUM(VI) IN WASTEWATER SAMPLES

4.1 Introduction

Chromium is a transition metal that exists primarily in two stable oxidation states in environmental and biological systems: trivalent chromium (Cr(III)) and hexavalent chromium (Cr(VI)) [216]. These two species exhibit markedly different chemical, toxicological, and environmental behaviors. While Cr(III) is an essential micronutrient for humans, playing a role in glucose and lipid metabolism, Cr(VI) is highly toxic, mutagenic, and carcinogenic. Its high solubility and mobility in water systems further exacerbate environmental and health concerns [217, 218]. Consequently, the selective detection and speciation of Cr(III) and Cr(VI) are critical for environmental monitoring and risk assessment.

Voltammetric methods leverage the distinct redox behaviors of Cr(III) and Cr(VI) under controlled electrochemical conditions, enabling their discrimination and quantification [219].

In this study, two different sensor chips with SPCE modified either by silver-gold bimetallic nanoparticles or silver-gold bimetallic oxide nanoparticles were developed. After characterization, the two sensor chips were integrated as an electrochemical sensor array, which could be applied to detect Cr(VI) and Cr(III). Combined with a handheld dual-channel electrochemical device, the electrochemical sensor array could detect Cr(III), Cr(VI) and the total chromium contents in various samples.

4.2 Experimental

4.1.1 Materials and reagents

Analytical grade reagents and high purity solvents were used throughout the study. Gold standard for ICP (1000 ppm Au(III) in 5% hydrochloric acid), silver standard for ICP (1000 ppm Ag(I) in 2% nitric acid), chromium (III) standard for ICP (1000 ppm Cr(III) in nitric acid), chromium (VI) standard for ICP (1000 ppm Cr(VI) in H_2O), potassium dichromate ($K_2Cr_2O_7$), chromium (III) nitrate nonahydrate (Cr $(NO_3)_3$ $9H_2O$), sulfuric acid (H_2SO_4, 98%), sodium chloride (NaCl), lactic acid, urea, acetic acid (HAc), sodium sulfite (Na_2SO_3) and sodium hydroxide (NaOH) were purchased from Merck Pte. Ltd. (Singapore). Artificial saliva was purchased from ChuangFeng Technology (China). Deionized water (DI water) from a Millipore Milli-Q purification system was used in all experiments. Artificial sweat was prepared by mixing 0.5 wt% of NaCl, 0.1 wt% of urea, and 0.1 wt% of urea lactic acid in DI water [220]. Tap water was obtained from the laboratory of Residues and Resource Reclamation Centre (R3C), Nanyang Environment and Water Research Institute (NEWRI), Nanyang Technological University (NTU).

4.2.2 Apparatus

SPCE (DRP-C110, Metrohm) equipped with a conventional three-electrode system, with carbon as the WE and RE and silver as the CE, was used for further modification. CV, DPV, and SWV were conducted using a portable multi-potentiostat (μstat8000p, Metrohm). The morphology of the electrode surface and the distribution of elements were studied by FESEM (JSM-7200F, Jeol) and TEM (JEM-1400Plus, JEOL) equipped with energy EDS. The valence of elements was determined by XPS (AXIS Supra, Kratos Analytical) equipped with a Monochromatic Aluminium Kα source. CASA XPS software was used for the deconvolution of the XPS spectra after correcting the binding energies of all elements against the adventitious carbon C 1s core level at 285 eV. HPLC (Ultimate 3000, Thermo Fisher Scientific) was used to separate two different Cr ions in chromium-containing wastewater. The contents of Cr were detected by

ICP-OES (OPTIMA 8300, PerkinElmer) and ICP-MS (iCAP Q, Thermo SCIENTIFIC).

4.2.3 Modification of WEs

The newly developed electrodes were prepared using the following steps: firstly, to prevent silver from reacting with gold and nitric acid, the reference electrode was covered with transparent tape during the electrodeposition process. Then, 0.1 mL of 100 ppm Au (III) solution was dropped on the electrode, and the Au nanoparticles were obtained by applying a potential of -0.4 V for 120 s, after washing with DI water and drying at room temperature (25 °C), the obtained electrode was labeled as Au-SPCE. Ag-Au-SPCE was obtained by dropping 0.1 mL of 1 ppm Ag (I) solution on Au-SPCE and then applying a potential of -0.4 V for 120 s. After the electrodeposition process, the tape was removed, and both the electrodes were activated (oxidized) and stabilized in 0.5 M NaOH solution by a CV potential between + 0.6 to 0.0 V at a scan rate of 0.05 $V \cdot s^{-1}$ and step potential of 0.002 V for 10 cycles. These two electrodes were labeled Au-SPCE-a and Ag-Au-SPCE-a, respectively. The whole process is shown in Figure 18. The electrodes modified by only Ag and Ag oxides were also prepared using the same method, labeled as Ag-SPCE and Ag-SPCE-a. However, reusing electrodes for complicated samples is not recommended to ensure the accuracy of the results. Therefore, the electrodes are considered to be disposable in the present study.

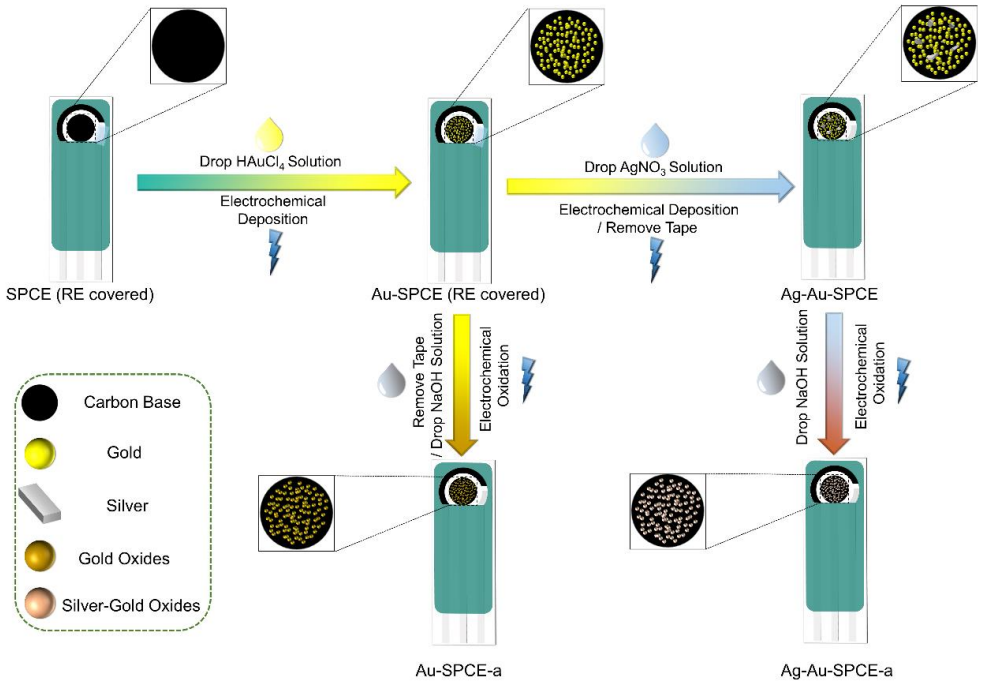

Figure 18. Preparation procedure of electrodes.

4.2.4 Electrochemical measurements

For Cr(III), 100 µL of Cr(III) standard solutions (with different concentrations dissolved in 0.5 M NaOH) were dropped on the Au-SPCE-a and Ag-Au-SPCE-a. The optimized conditions of the electrochemical method were as follows: element deposition at a potential of -0.2 V for 120 s, then tested by DPV with the potential from -0.2 to +0.3 V at a step potential of 0.008 V, pulse potential of 0.05 V, pulse time of 0.08 s and a scan rate of 0.04 $V \cdot s^{-1}$.

Similarly, the optimized parameters and steps for Cr(VI) were as follows: 100 µL of Cr(VI) standard solutions (with different concentrations dissolved in 0.1 M acetic acid buffer, pH = 4.5, adjusted by 1 M NaOH) was dropped on the Au-SPCE and Ag-Au-SPCE, the samples were preconcentrated for 120 s at a voltage of +0.6 V and then tested by SWV with the potential from +0.2 to -0.5 V at a step potential of 0.005 V, amplitude potential of 0.002 V and frequency of 25 Hz. The following experimental conditions were consistent with those mentioned here unless otherwise specified. The data of electrochemical measurements were recorded and analyzed by DropView 8400 software. All the electrochemical data

and error bars (standard deviations) were obtained by averaging three consecutive repetitions.

4.2.5 Preparation of Cr(III/VI) contained samples

Cr (III and VI together) standards were spiked into artificial saliva, artificial sweat, and tap water to obtain representative chromium samples with real sample backgrounds. Furthermore, the used glassware was immersed in sulfochromic mixture for cleaning and the washing solution was used as the original chromium-containing wastewater (labeled as S1); 10 mL of S1 was mixed with 1 mL of 10 mM sodium sulfite solution, which was labeled as S2; another 10 mL of S1 was mixed with 2 mL of 10 mM sodium sulfite solution, which was labeled as S3; 10 mL of S3 was adjusted the pH to 7.4 with 10-50 mM sodium hydroxide solution, filtered, and taken the filtrate, which was labeled as S4. This process simulated the treatment of hexavalent chromium wastewater. The samples were further diluted with NaOH solution for Cr(III) and HAc solution for Cr(VI), adjusted their concentrations to fall within the linear range, and then tested using Ag-Au-SPCE for Cr(VI) and Ag-Au-SPCE-a for Cr(III).

4.2.6 HPLC-ICP-MS analysis

For comparison, the total Cr content and Cr(VI) in chromium-containing wastewater were detected by ICP-OES/MS and HPLC-ICP-MS, respectively. The HPLC-ICP-MS analytical procedures and experimental parameters were as follows: The HPLC injection volume was set at 100 µL, and Dionex AG-7 (2 x 50 mm) guard column was used for the separation [221, 222]. The mobile phase was 0.4 M HNO_3 with a flow rate of 400 µL min^{-1}, and the elution cycle was 180 s. For the ICP-MS part, argon gas flow for plasma was 14 L min^{-1}, helium gas flow was 4.41 L min^{-1} for KED mode, and monitored m/z for Cr was 52. Since some parts of the HPLC system had been made of stainless steel materials, Cr(III) with different amounts could possibly be released during the test (Figure 19 a and b), resulting in inaccurate Cr(III) calibration results (Figure 20a), while the

calibration curve of Cr(VI) could provide good linearity (Figure 20b, R^2 = 0.9968, LOD = 6.421 ppb). Besides, in the real samples, the Cr(III) peak shifted significantly (Figure 19 d), and thus the data for Cr(III) quantification was not used. As previously mentioned, Cr mainly exists in the form of Cr(III) and Cr(VI), and thus, the content of Cr(III) was calculated by subtracting the content of Cr(VI) from total chromium content.

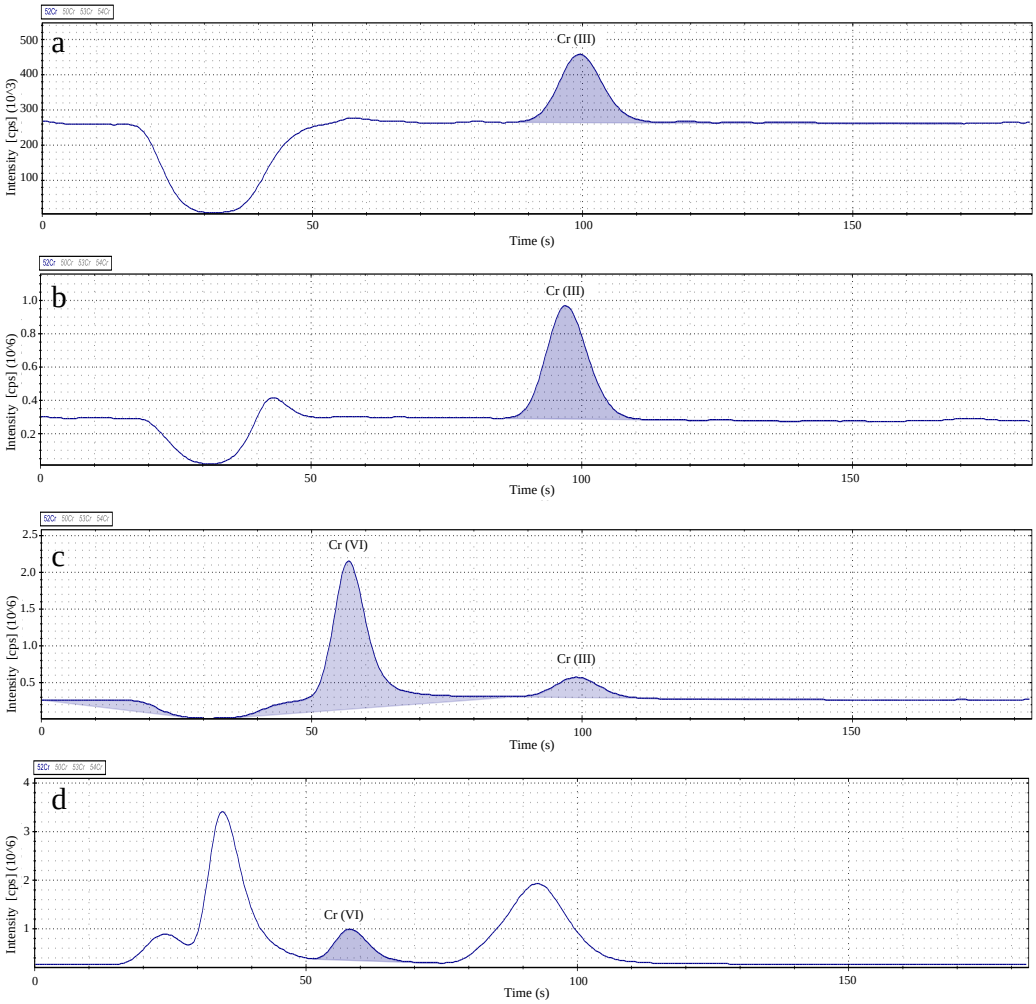

Figure 19. HPLC-ICP-MS spectra of 2 injections of the same DI water sample: a and b (peak area of Cr (III) a: 1,934,645.53 cps·s and b: 6,195,538,48 cps·s); 50 ppb Cr (III) and (VI) standard: c and sample S1: d.

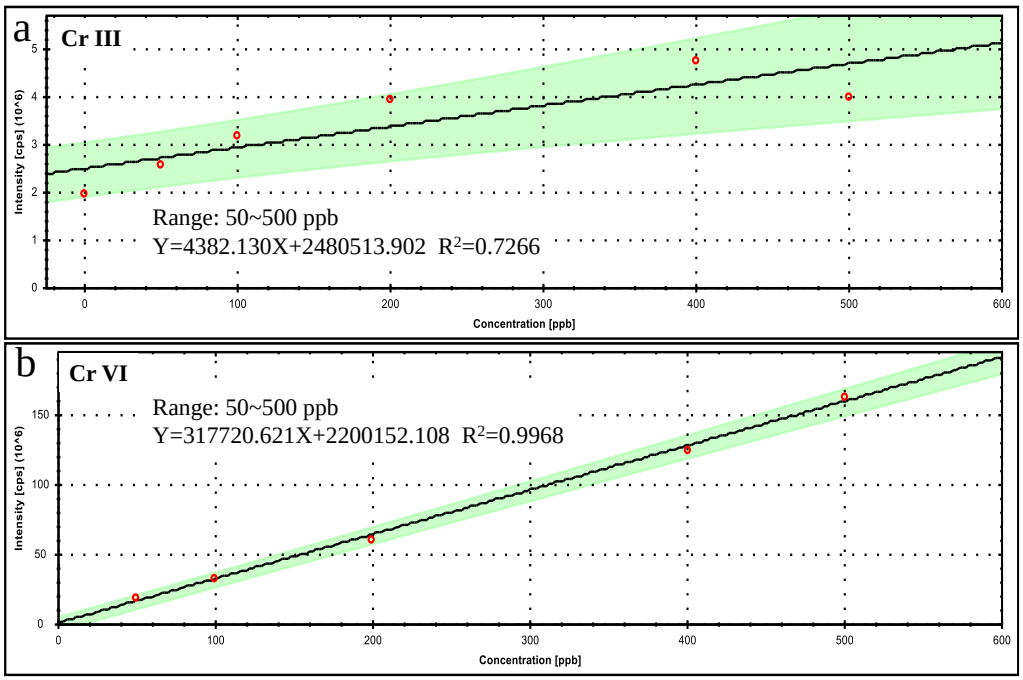

Figure 20 HPLC-ICP-MS calibration curves of Cr (III): a, and (VI): b.

4.3 Results and discussion

4.3.1 Characterization of Au and Ag nanoparticles on the WEs

The morphology of the working electrodes of Au-SPCE and Au-SPCE-a are shown in Figure 21 a1 to i1. From Figure 21 a1 to c1, it could be observed that the freshly prepared gold nanoparticles (AuNPs) were unevenly distributed on the electrode surface, and many particles were concentrated in a small area. It was also found that these AuNPs spontaneously formed micron-sized massive aggregates after being stored in the air for one day (Figure 21 d1 to f1). However, as shown in Figure 21 g1 to i1, Au oxides were much more uniformly distributed than AuNPs after electrochemical oxidation, and no obvious change in morphology and aggregation state was observed after one day of storage.

Similarly, Figure 21 a2 to i2 shows the FESEM images of the AuNP electrode surface further modified with silver nanoparticles. In Figure 21 a2 to c2, the particle sizes of AuNPs after further deposition of silver were much smaller than that of freshly prepared ones, which indicated that even if the $HAuCl_4$ was removed, negative voltage and silver ions could still affect the morphology of

deposited AuNPs. Also, the silver was present in the form of massive particles of different sizes on the surface of the working electrode. Different from Au-SPCE, after the Ag-Au-SPCE was placed in the air for one day (Ag-Au-SPCE-1 day, and the Ag-Au-SPCE tested directly after fresh preparation is marked as Ag-Au-SPCE-0 day), the nanoparticles on the surface did not agglomerate, but spontaneously formed evenly distributed nanocomposite particles with bigger diameters (Figure 21 d2 to f2). This morphology was very close to that of Ag-Au-SPCE after electrochemical oxidation (i.e., Ag-Au-SPCE-a, Figure 21 g2 to i2). Like Au-SPCE-a, the surface of Ag-Au-SPCE-a also did not change after one day of storage at room temperature. Based on this spontaneous conversion phenomenon, it was speculated that there was a silver-gold oxide species that is stable at room temperature, and electro-oxidation helped to form this silver-gold oxide species much faster.

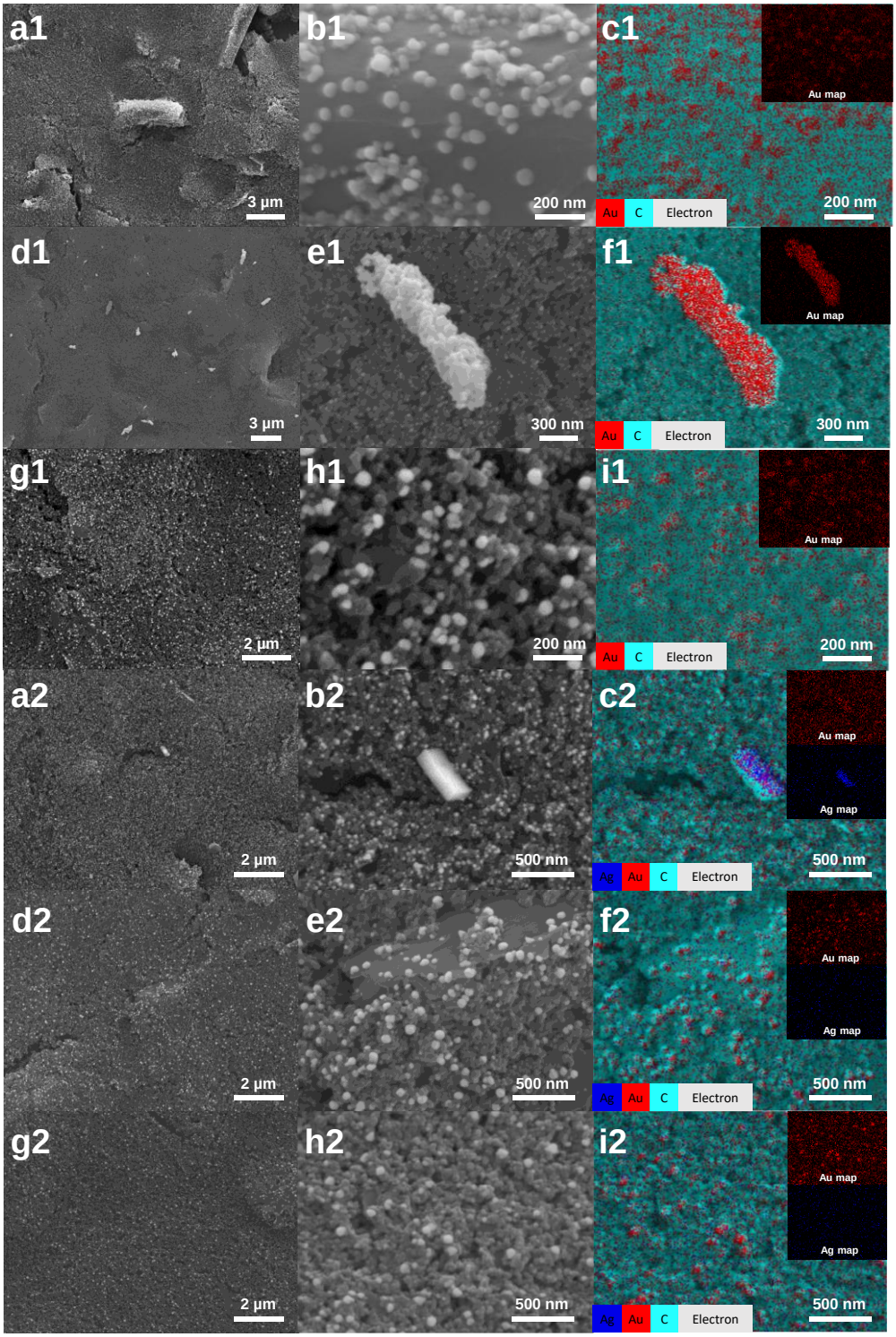

Figure 21. FESEM images of Au-SPCE (a1, b1, d1 and e1), Au-SPCE-a (g1 and h1), Ag-Au-SPCE (a2, b2, d2 and e2) and Ag-Au-SPCE-a (g2 and h2); layered element mappings of Au-SPCE (c1 and f1), Au-SPCE-a (i1), Au-SPCE (c2 and f2) and Au-SPCE-a (i2). Insert: element mapping of gold and silver. Among these images, a1, b1, c1, g1, h1, i1, a2, b2, c2, g2, h2, and i2 were taken within one hour after the preparation

of the electrodes, while d1, e1, f1, d2, e2 and f2 were taken one day after the preparation.

The particle size distributions of the particles on the surface of freshly prepared Au-SPCE-a, Ag-Au-SPCE-1 day, and Ag-Au-SPCE-a were measured by NanoMeasure 1.2 Software. As shown in Figure 22 a to c, their average sizes were 46.4 ± 9.9 nm, 56.7 ± 13.7 nm, and 67.8 ± 18.0 nm, respectively. It could be seen that as the oxidation degree of the gold/silver-gold particles increased, the particle size also increased. At the same time, the spontaneous bonding process of the silver-gold particles was also observed.

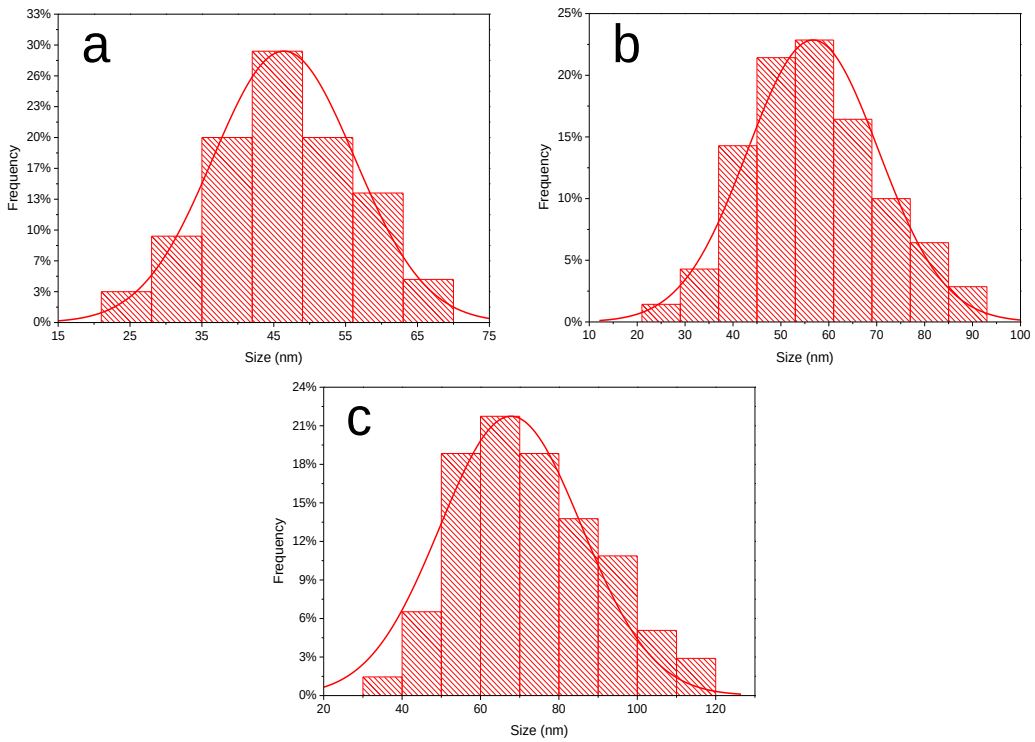

Figure 22. Particle size distribution of the particles on the surface of freshly prepared Au-SPCE-a (a), Ag-Au-SPCE-a (c), and Ag-Au-SPCE after being left in the air for one day (b).

After scraping the working electrode with a blade, the powdered sample was dispersed in water and sonicated for 20 minutes, then dropped onto a copper grid and dried in a nitrogen atmosphere for TEM testing. Due to the long preparation time of the sample, the silver particles in the mapping image were not as obvious as those in the FESEM images (Figure 23 a and b). Nevertheless, comparing the electrode surface particles after a day of storage (Figure 23 c and d) and

electrochemical oxidation (Figure 23 e and f), its distribution was still more aggregated. In addition, the weak signal of silver might be caused by the higher voltage and the stronger penetrability of TEM than FESEM, which could also be used to support the theory that silver species exist on the outer surface of gold and silver particles after oxidation on the electrode surface.

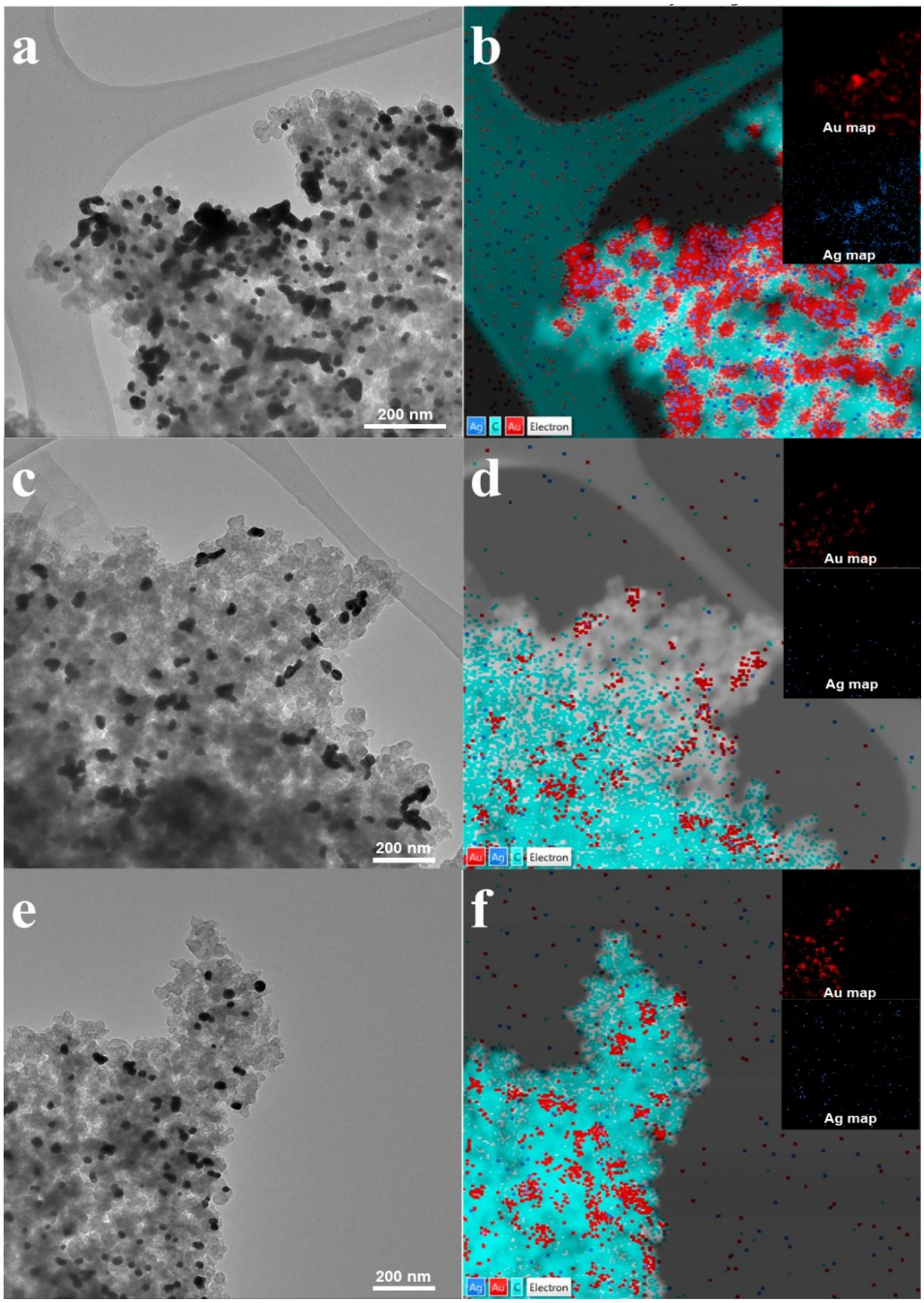

Figure 23. TEM images of Ag-Au-SPCE (a and c) and Ag-Au-SPCE-a (e); layered element mappings of Au-SPCE (b and d) and Au-SPCE-a (f), insert: element mapping

of gold and silver. Among these images, a, b, e, and f were taken within two hours after the preparation of the electrodes, while c and d were taken one day after the preparation of Ag-Au-SPCE.

The oxidation states of Ag and Au elements on Ag-Au-SPCE-a were also investigated by XPS. Due to the shallow electron escape depth (usually less than 10 nm) in the XPS test, the obtained results could be correlated only to the properties of the outermost layer of the nanoparticles. As shown in Figure 24a, the binding energies of [374.2, 368.2] and [373.8 eV, 367.8] eV with an energy difference of 6.0 eV indicated that the silver exists in the form of Ag (0) and Ag (I), respectively [223, 224]. The gold on the particle surface was found to exist in the form of Au(0), Au(I), and Au(III), and the corresponding binding energies were [87.6, 83.9], [88.1, 84.4] and [89.5, 86.1] eV, respectively [225]. In general, the freshly prepared Ag-Au-SPCE contained only elemental gold and silver. However, after one day, the peaks of Ag and Au shifted to their respective oxidation states. Especially for Au, the peaks fully shifted to Au(I) peak, which indicated the Au on the surface was oxidized. Finally, after the electrochemical oxidation, all the silver and gold in the outer layer reached the oxidation state and were not in the elementary state. Considering the small amount of silver (theoretically 1% of the amount of Au), there was almost no signal of individual silver particles in the element mapping (Figure 21 i2). It is speculated that silver was distributed on the surface of AuNPs and formed stable Ag-O-Au moieties. The results here further proved the previous speculation: a small amount of silver on the gold surface could induce spontaneous oxidation of gold in the air.

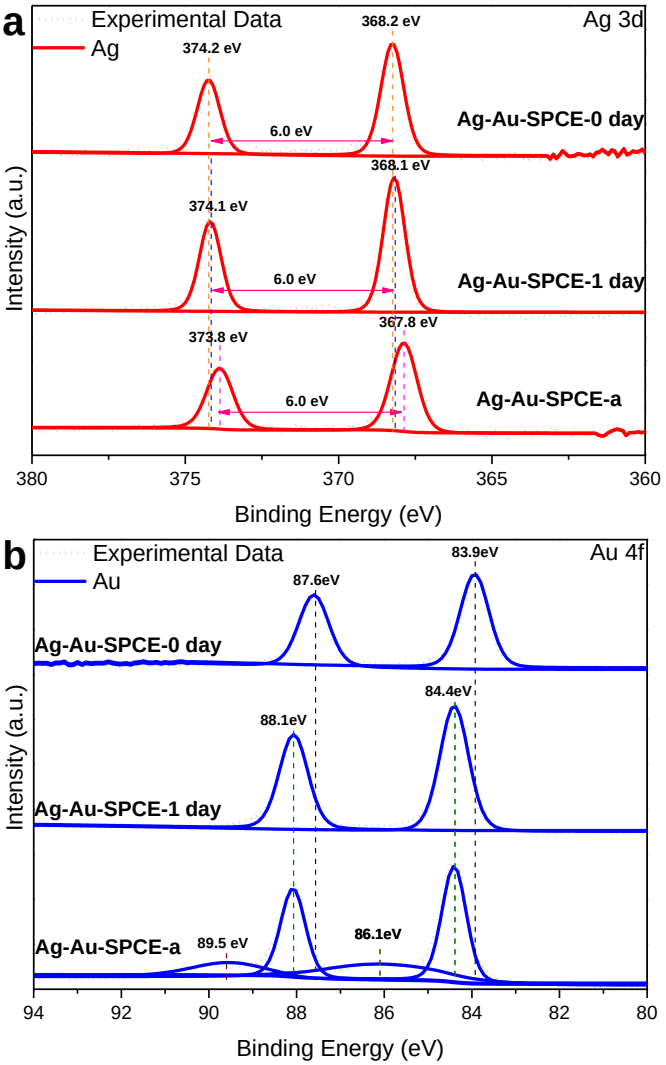

Figure 24. XPS spectra of Ag 3d (a) and Au 4f (b) of Ag-Au-SPCEs.

4.3.2 Electrochemical detection of Cr(III) and Cr(VI)

Au-SPCE-a and Ag-Au-SPCE-a were used to test their response to 1 ppm of Cr(III) under the same conditions. As shown in Figure 25, the electrochemical response signal intensity of Ag-Au-SPCE-a was approximately twice that of Au-SPCE-a, while there was almost no signal from Ag-SPCE-a. Recalling the particle size distribution of these two types of gold/silver-gold oxide nanoparticles, the average particle size of gold oxides is 21.4 nm smaller than that of silver-gold oxide particles. In classical theory, the larger surface area and more reactive sites resulting from smaller particle sizes tend to enhance the activity of

the reaction. The phenomenon appeared to contradict this theory. However, it is believed that this precisely reflects the fact that 1% of the theoretical addition of silver had a great effect on the formation and stabilization of gold oxides, so it could overcome the adverse effects of the particle size effect and showed better response than smaller sized gold oxides nanoparticles. In addition, as the positions of the Cr(III) oxidation peaks produced by these two electrodes were almost the same, it is speculated that silver species did not participate in the electrode reaction.

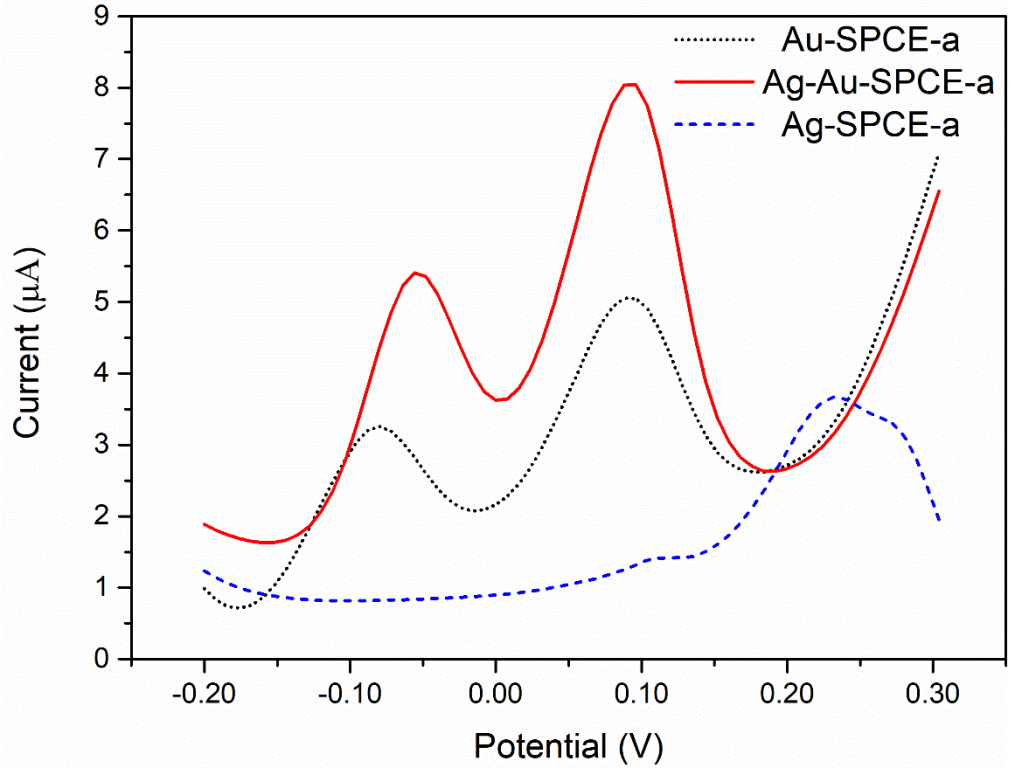

Figure 25. Comparison between the electrochemical signal of Au-SPCE-a and Ag-Au-SPCE-a to 1 ppm of Cr (III).

Although the silver-gold oxides appeared to be more stable than gold oxides, it was still easily electrochemically reduced during the deposition process. Therefore, the deposition potential and time were optimized as shown in Figure 26 a and b. The lowest deposition potential was chosen to be -0.4 V, which was the same for the deposition of both Au and Ag. From -0.4 V to -0.2 V, the peak height first increased slightly, but from -0.2 V to 0.1 V, the peak height decreased

rapidly, indicating that the negative voltage is more suitable for the enrichment of Cr(III) species in this case. On the one hand, a long deposition time is beneficial for pre-concentration of Cr(III) on the electrode surface. On the other hand, -0.2 V was sufficient negative to reduce silver-gold oxides. Hence, it was not conducive to the retention of silver-gold oxides. As a result, the peak height decreased first, and then increased with the increase of deposition time, and finally decreased from a downward trend. Eventually, a deposition time of 120 s was tested in the standard solution of Cr(III). Chromatograms and calibration curves (linear relationship between peak height and standard solution concentrations) are shown in Figure 28 a and b, with a linear range of 0.05~1 ppm and LOD of 0.1 ppb Cr(III).

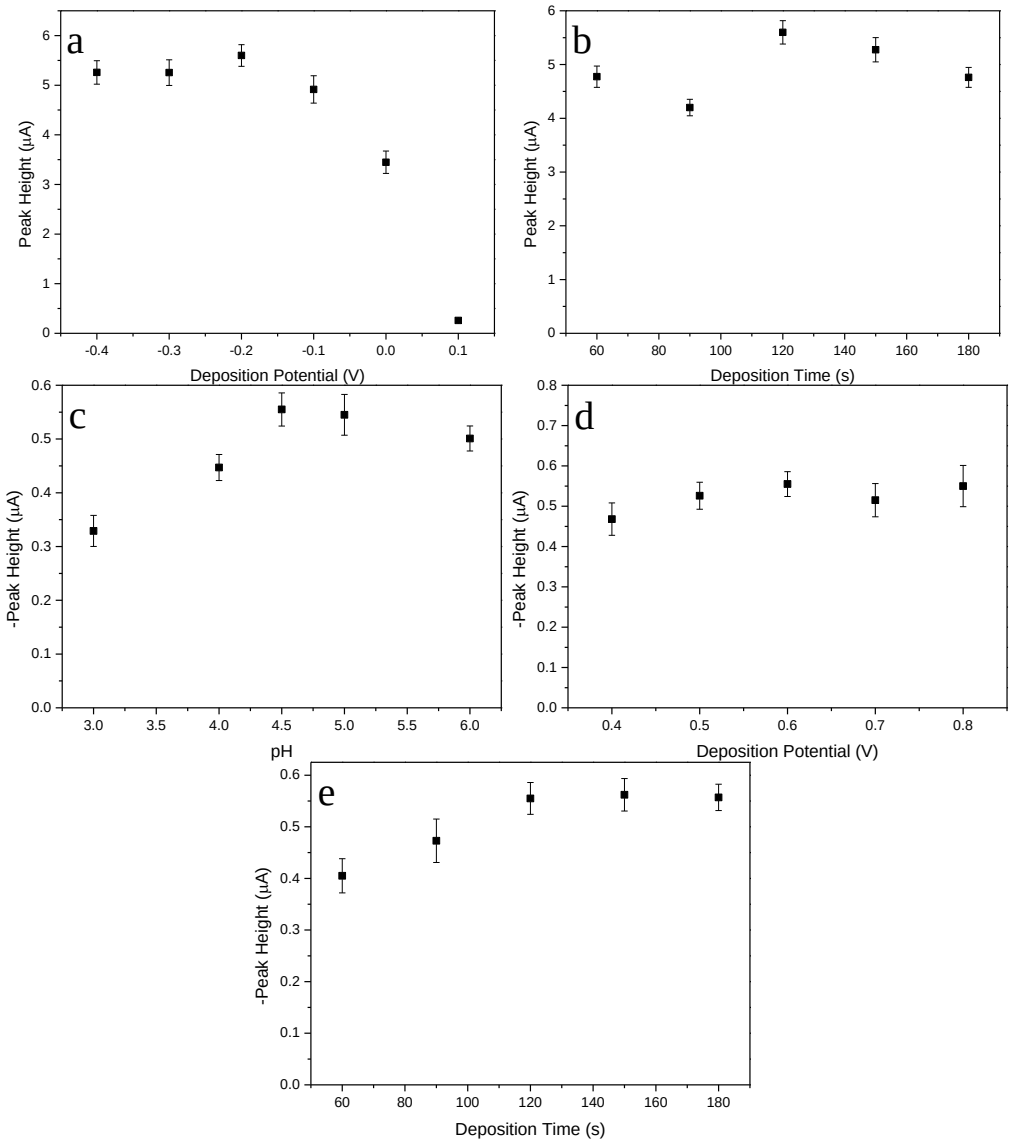

Figure 26. Optimize Cr(III) detection parameters: deposition potential (a) and deposition time (b); optimize Cr(VI) detection parameters: pH (c), deposition potential (d) and deposition time (e).

Ag-Au-SPCE was used for the electrochemical detection of Cr(VI), with the comparison of Au-SPCE. Their response to 1 ppm of Cr(VI) is shown in Figure 27. The signal generated by Ag-Au-SPCE was about 50% higher than that of Au-SPCE, while Ag-SPCE did not provide a peak. This could be explained by the size effect, AuNPs from Ag-Au-SPCE were much smaller than those from Au-SPCE.

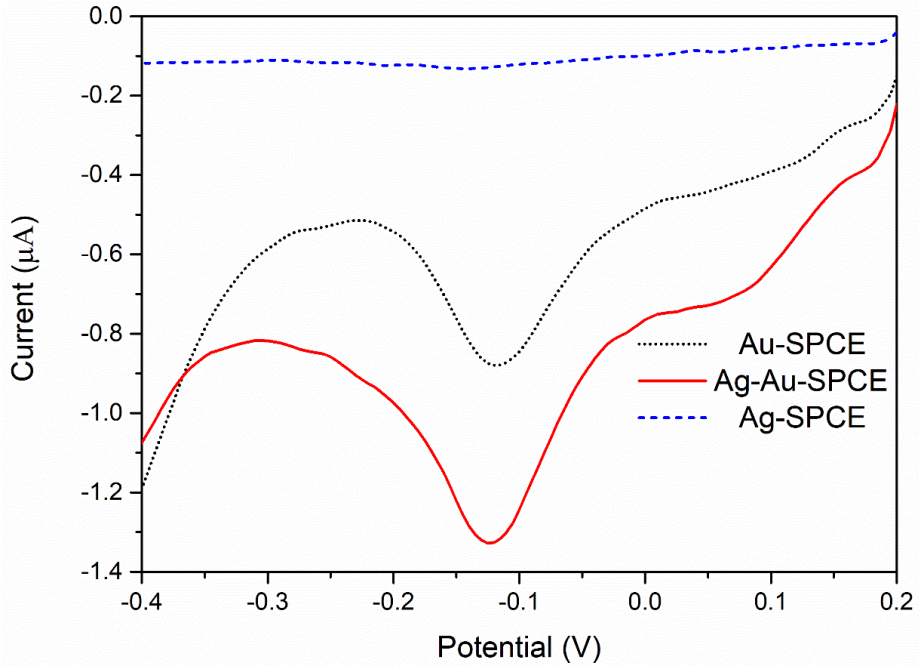

Figure 27. Comparison between the electrochemical signal of Au-SPCE and Ag-Au-SPCE to 1 ppm of Cr (VI).

After optimizing the detection parameters (Figure 26 c, d and e,), this electrode was further used to detect Cr(VI) with different concentrations under the optimum conditions (pH 4.5, deposition potential 0.6 V, deposition time 120 s), and the results are shown in Figure 28 c and d. The linear range and LOD were found to be 0.05~5 ppm and 0.1 ppb Cr(VI), respectively. The linear ranges and LODs of both Cr(III) and Cr(VI) could meet the different standards from CONAMA, Japan, US EPA and WHO.

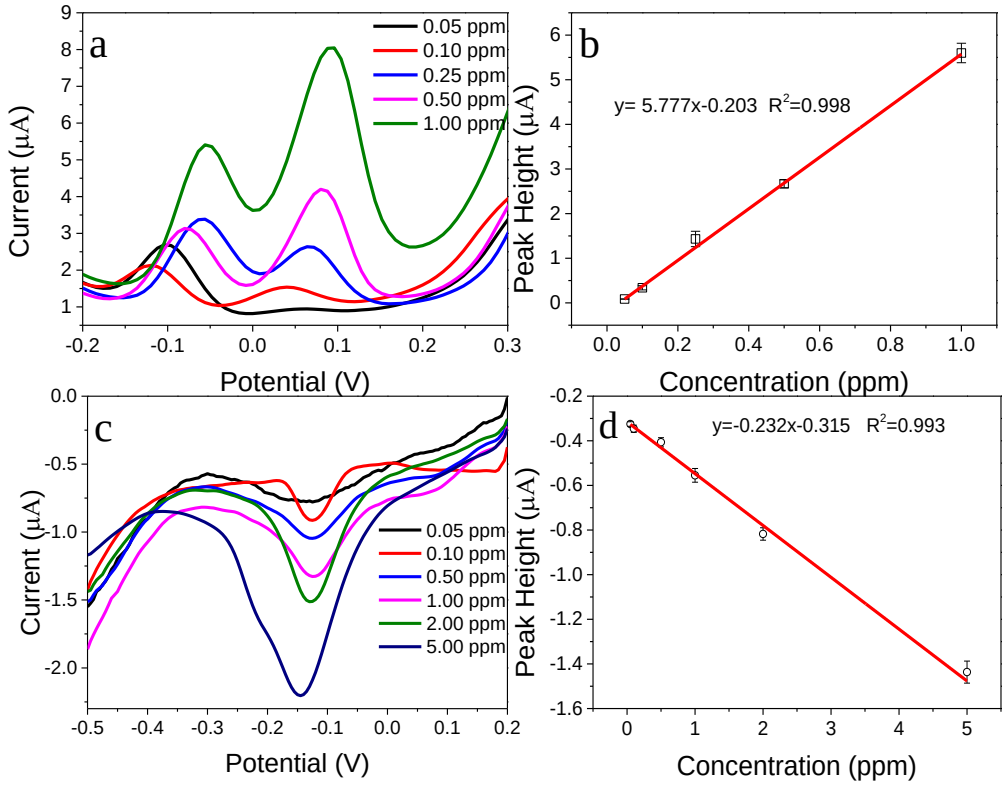

Figure 28. DPV response (a) and linearity (b) of 0.05~1 ppm Cr(III) detected with Ag-Au-SPCE-a under optimized conditions; SWV response (c) and linearity (d) of 0.5~5 ppm Cr(VI) detected with Ag-Au-SPCE.

Under the optimized conditions, the responses of 0.1 ppm Cr(III) and 0.5 ppm of Cr(VI) with Au-SPCE-a and Au-SPCE were low (Figure 29), which indicated that the detection ranges of these two electrodes were higher than the electrodes with both Ag and Au.

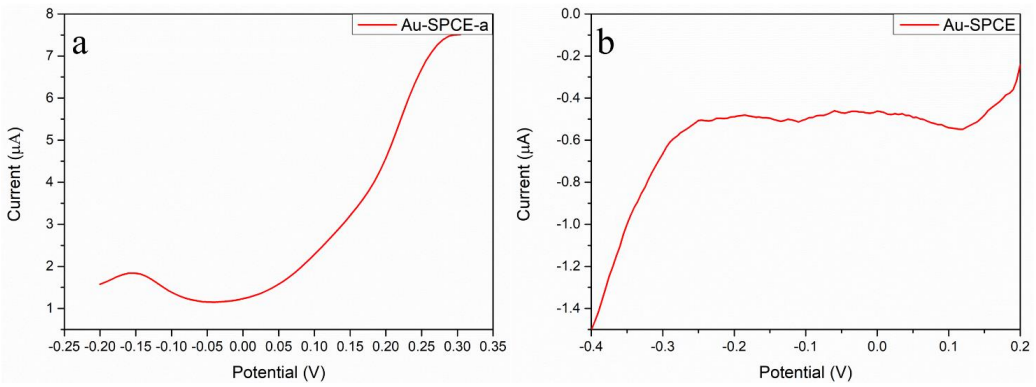

Figure 29. DPV response of 0.1 ppm Cr (III) detecting with Au-SPCE-a (a) and SWV response of 0.5 ppm Cr (VI) detecting with Au-SPCE (b).

The anti-interference performances of the developed electrodes were studied by adding different metal ions to 1 ppm Cr(III/VI) standards, and the electrochemical response was measured under the optimized conditions. As shown in Table 8, most of the common metal ions did not affect the detection of Cr(III/VI). However, a few metal ions could co-precipitate (Cu (II), Zn (II), and Pb (II)) or react (As (III)) with Cr species, leading to a significant decline in the signals.

Table 8. Change of peak height of Cr(III/VI) caused by interferent.

Interference	Concentration	Change of peak of Cr(III) height in %	Change of peak of Cr(VI) height in %
Na(I)	11500 ppm (0.5M)	100%	101%
K(I)	19500 ppm (0.5M)	99%	99%
As(III)	1 ppm	95%	65%
As(VI)	1 ppm	99%	97%
Cu(II)	1 ppm	63%	102%
Zn(II)	1 ppm	74%	105%
Hg(II)	1 ppm	81%	101%
Pb(II)	1 ppm	34%	82%
Cd(II)	1 ppm	96%	95%

As shown in Table 9, the performances of the developed sensors are better than or comparable to those in previous works. More importantly, the sensors developed in the current study provided lower LODs, and their application ranges could also be expanded.

Table 9. Comparison of the performances of different modified electrodes for determining Cr(III) and Cr(VI).

	Electrode	Method	Linear range	LOD	Sample(s) applied	Ref
Cr(III)	GC/Chit/MWCNTs/MnOxNPHCA		156~10400 ppb	0.0156 ppb	-	[137]
	Chi–Au-SPEs	DPV	52~5200 ppb	20.8 ppb	Industrial wastewater	[226]
	CrIP-CCE	DPV	5.2~520 ppb	0.9125 ppb	River/sea water, urine	[227]
	Ag-Au-SPCE-a	DPV	50~1000 ppb	0.1 ppb	Artificial saliva/sweat, tap water, sulfochromic mixture	Current work

Cr(VI)	Gold screen printed macro electrodes	LSV	0.52~83.2 ppm	0.2288 ppm	Canal water	[136]
	Ag-doped TiO_2 on glassy carbon	Amperometry	5.2~161.2 ppb	1.716 ppb	Tap/lake water	[228]
	Nickel oxide nanoparticles	CV	5~50 ppm	-	-	[229]
	Ag-Au-SPCE	SWV	50~5000 ppb	0.1 ppb	Artificial saliva/sweat, tap water, sulfochromic mixture	Current work

GC: glassy carbon; Chit: chitosan; MWCNTs: multiwalled carbon nanotubes; MnOxNP: manganese oxide nanocomposite; HCA: hydrodynamic chronoamperometric; Chi–Au-SPEs: chitosan–gold nanocomposites modified screen printed electrodes; DPV: differential pulse voltammetry; CrIP-CCE: Cr(III)-imprinted polymer-modified carbon composite electrode; LSV: linear sweep voltammetry; CV: cyclic voltammetry; SWV: square wave voltammetry.

4.3.3 Detection of Cr(III) and Cr(VI) in chromium spiked samples

To evaluate their application capabilities, Ag-Au-SPCE and Ag-Au-SPCE-a were used to quantify the concentrations of Cr(VI) and Cr(III) in different chromium spiked samples, and total chromium contents were also calculated. The chromium-spiked artificial saliva, artificial sweat, and tap water were analyzed using the proposed method. The results, shown in Table 10, indicated that the developed sensors were suitable for analyzing Cr(VI) and Cr(III) in these three chromium-spiked samples.

Table 10. Determination of chromium (III/VI) and total chromium in chromium spiked samples using Ag-Au-SPCE and Ag-Au-SPCE-a.

	Sample	artificial saliva	artificial sweat	tap water
Cr (III)	added/ppm	2.8	0.8	0.4
	found/ppm [a]	2.720 ± 0.133	0.811 ± 0.105	0.382 ± 0.077
	recovery/%	97.1	101.4	95.5
Cr (VI)	added/ppm	0.4	0.8	2.8
	found/ppm [a]	0.362 ± 0.093	0.897 ± 0.256	2.720 ± 0.188
	recovery/%	90.5	112.1	97.1
Cr (total)	added/ppm	3.2	1.6	3.2
	found/ppm [b]	3.082	1.708	3.102
	recovery/%	96.3	106.8	96.9

[a] Mean value of 3 measurements ± standard deviation.
[b] The sum of Cr(III) and Cr(VI) contents.

4.3.4 Detection of Cr(III) and Cr(VI) in wastewater samples

Chromium-containing wastewater and the wastewater generated during its

treatment were also used as real samples further to verify the practical application capabilities of the sensors. The pretreatment and testing methods were the same as in the previous section. The values measured by sensors were consistent with those measured by ICP and HPLC-ICP-MS (Table 11), indicating that the developed sensors were suitable for determining chromium in these types of wastewater. The results for S3 and S4 samples also demonstrated that the treatment process of hexavalent chromium wastewater simulated in this work is highly effective in removing toxic pollutants.

Table 11. Determination of chromium (III/VI) and total chromium in chromium-containing wastewater samples using Ag-Au-SPCE and Ag-Au-SPCE-a.

Sample		S1	S2	S3	S4
Cr (III)	Calculated/ppm [a]	4.641	13.685	13.53	N.D.
	Sensor/ppm [b]	4.239 ± 0.030	14.738 ± 0.214	15.676 ± 0.428	N.D.
Cr (VI)	HPLC-ICP-MS/ppm [b]	10.539 ± 1.015	1.425 ± 1.191	N.D.	N.D.
	Sensor/ppm [b]	11.892 ± 0.522	1.170 ± 0.114	N.D.	N.D.
Cr (total)	ICP/ppm [b]	15.18 ± 0.216	15.11 ± 0.364	13.53 ± 0.339	N.D.
	Sensor/ppm [c]	16.131	15.907	15.676	N.D.

[a] Calculated by mean value of Cr (total) - mean value of Cr(VI)
[b] Mean value of 3 measurements ± standard deviation.
[c] Calculated by mean value of Cr(III) + mean value of Cr(VI)
N.D.: Not detected, and the value was counted as below LOD.

4.4 Conclusion

In this chapter, a silver-gold bimetallic nanoparticles modified electrode (Ag-Au-SPCE) and a silver-gold bimetallic oxide nanoparticles modified electrode (Ag-Au-SPCE-a) were developed to detect Cr(VI) and Cr(III), respectively. The silver-gold bimetallic oxide nanoparticles were proved to be stable and sensitive to Cr(III), in which the addition of silver with a theoretical value of 1% of gold played a key role in the formation and stabilization of oxides on the surface of gold nanoparticles.

These sensors were successfully deployed to measure concentrations of Cr(III), Cr(VI), and total chromium in various samples, including tap water, artificial saliva, and artificial sweat, as well as to monitor the treatment processes in

chromium-containing wastewater. The potential for these sensors to be integrated with a handheld dual-channel electrochemical device suggests a promising future for developing laboratory-free, portable chromium detection systems. Such systems are expected to be especially beneficial for *in-situ* monitoring of chromium content across various environmental samples, including chemical plating facilities.

CHAPTER 5 SIMULTANEOUS SPECIATION OF INORGANIC ARSENIC (III AND V) UTILIZING GOLD-MANGANESE OXIDE NANOPARTICLES MODIFIED ELECTROCHEMICAL SENSORS

5.1 Introduction

Arsenic, a toxic metalloid, is a significant environmental and public health concern due to its widespread occurrence and severe toxicological effects [230]. It exists primarily in two oxidation states in natural systems: arsenite (As(III)) and arsenate (As(V)). These two forms differ significantly in their toxicity, mobility, and bioavailability, with As(III) being significantly more toxic and mobile than As(V) [231, 232]. The speciation of these arsenic forms is critical for assessing environmental risks, understanding biogeochemical processes, and implementing effective remediation strategies. The difference in electrochemical activity of the two species makes it possible to distinguish them electrochemically, especially through voltammetry methods [233].

The performance of voltammetric speciation relies on the optimization of various factors, such as electrode material, pH of electrolyte, and applied potential. Hence, a series of Au-Mn oxides nanocomposites were designed and applied to the speciation of inorganic As. Moreover, using developed electrodes, the total As and As(III) can be easily determined simultaneously by dual measurement (using two channels of the electrochemical working station). The accuracy of the sensor outcomes was further validated by HPLC-ICP-QQQ, ensuring reliability in our speciation analysis.

5.2 Experimental

5.2.1 Materials and reagents

The chemicals, reagents, and solvents used are of analytical grade and high purity and were used without further purification. Sodium hydroxide (NaOH), acetic

acid (HAc), sodium dimethyldithiocarbamate (SDDC), tetrachloroauric(III) acid ($HAuCl_4 \cdot 3H_2O$), sodium borohydride ($NaBH_4$), hydrochloric acid (37%, HCl), potassium permanganate ($KMnO_4$), sodium arsenate (Na_3AsO_4), sodium arsenite ($NaAsO_2$), ammonium hydroxide solution (28~30% NH_3 basis, NH_4OH), iron(III) chloride hexahydrate ($FeCl_3 \cdot 6H_2O$), ethylene glycol (EG), sodium dodecyl sulfate (SDS), polyethylenimine (PEI) and individual standard ion solutions of lead, cadmium, zinc, copper, nickel, cobalt, mercury and chromium (III and VI) for ICP-OES were purchased from Merck Pte. Ltd (Singapore). 1000 ppm As(III) and 1000 ppm As(V) standards were purchased from inorganic Ventures (Singapore). DI water with a resistivity of less than 18.2 MΩ·cm was obtained from a Millipore Milli-Q purification system to prepare solutions.

5.2.2 Apparatus

Commercial SPCE (DRP-C110, Metrohm) was modified for further use. The electrochemical measurements were performed by a multi-potentiostat (μstat8000p, Metrohm). XRD (SmartLab SE) with Cu-Kα radiation, operated at 40 kV and 30 mA, was used to investigate the crystalline phase of synthesized materials. The oxidation states of the elements in the synthesized materials were identified by XPS (K-Alpha, Thermo Scientific). The XPS spectra underwent deconvolution through CASA XPS software following the adjustment for binding energies across all elements relative to the adventitious carbon C 1s core level (285 eV). The material morphology and elemental distributions were examined initially using FE-SEM coupled with EDX spectroscopy (JSM-7200F, JEOL Ltd.), followed by TEM (JEM-1400Plus, JEOL Ltd.). HPLC (1260 Infinity II LC System, Agilent Technologies, Inc.) coupled to ICP-QQQ (8900 Triple Quadrupole ICP-MS, Agilent Technologies, Inc.) as a standard method for As speciation.

5.2.3 Synthesis of nanomaterials and fabrication of working electrode

30 mg of Au (~60 mg of $HAuCl_4 \cdot 3H_2O$) and 3 mg of Mn (~8.616 mg of $KMnO_4$,

Au: Mn = 10:1, m/m) were dissolved in 15 mL and 30 mL of DI water separately, and then the two solutions were mixed with 0.5 mL of EG. Subsequently, the pH of the mixture solution was adjusted to 7 by 0.25 ~ 2.5% ammonium hydroxide solution and 0.01 M HCl. Then, the mixture was stirred overnight at room temperature, followed by solids extraction by centrifugation, and finally freeze-dried. The synthesized material was labeled as AuMnNPs-10 and dispersed in DI water at different concentrations for further use.

For comparison, diverse compositions of nanoparticles, such as Au-only, Mn-only, and various gold-to-manganese ratios of Au: Mn = 20: 1, 5: 1, and 2: 1 (m/m), were synthesized while keeping all the parameters constant, except for the amount of Au and Mn precursors. The synthesized materials were labeled as AuNPs, MnNSs, AuMnNPs-20, AuMnNPs-5, and AuMnNPs-2, respectively. The WE was modified by drop-casting method: the dispersed nanomaterial was dropped onto the WE of the SPCE, and then dried in an oven at 60 °C for further use.

5.2.4 Electrochemical measurements

The experiments were performed in a buffer containing 0.1 M HAc, and the pH was adjusted by adding 0.1 M NaOH and 1 M HCl. Parameters such as pH, deposition potential and time, and the type and amount of synthesized material were further optimized. The final protocol for total As content detection was as follows: 100 µL of the sample (in acetic-acetate/ HCl buffer, pH = 2) was dropped on the electrode modified with 10 µL of 0.7 mg/mL of AuMnNPs-10 (the electrode was labeled as AuMn-10-SPCE), covering all 3 electrodes, and a voltage of -1.1 V was applied for 180 s. Subsequently, DPV measurements were conducted, scanning potentials from -1.1 V to 0.2 V. The parameters for step potential, pulse potential, pulse time, and scan rate were established at 0.004 V, 0.04 V, 80 ms, and 0.02 V/s, respectively. All parameters for the detection of As(III) were the same as that for total As content, except the deposition potential was -0.6 V, and DPV sweep was from -0.6 V to 0.2 V. The two different methods

can be applied together on the multi-channel potentiostat so that speciation can be carried out simultaneously. Triplicated measurements obtained from the presented mean value and standard deviation (SD) are shown in the form of error bars.

5.2.5 Treatment and monitoring of As-contained wastewater

$Fe(OH)_3$ suspension was synthesized by boiling 50 mL of solution containing 20 g/L $FeCl_3 \cdot 6H_2O$ for 10 min and topping up to 100 mL. It was used as the precipitant during the As-contained wastewater treatment process. An artificial wastewater containing both As(III) and As(V) was prepared by mixing As(III) and As(V) standards. 5 mL of the original sample was distributed into 5 test tubes and then treated by introducing 0.5, 1, 1.5, and 2 mL of $Fe(OH)_3$ suspension into samples and topped up to the same final volume of 10 mL (labeled as raw, S1, S2, S3, and S4, respectively). The samples were kept overnight, filtered by a 0.45 µm membrane filter, diluted, and analyzed by HPLC-ICP-QQQ and the developed sensor (AuMn-10-SPCE).

The HPLC-ICP-QQQ methods were as follows: the separation was conducted using a column (G3288-80000, Agilent Technologies, Inc.) with a 100 µL injection volume. The mobile phase was A: 5 mM $(NH_3)_2CO_3$ and B: 50 mM $(NH_3)_2CO_3$ with a flow rate of 1 $mL \cdot min^{-1}$. The specific elution procedure was as follows: 100% A at 0~2 min, 100% B at 2~17 min, and 100% A at 17~24 min. For the ICP-QQQ part, the monitored m/z for As as a product ion was 75.

5.3Results and discussion

5.3.1 Material characterization

Figure 30 (a) shows the XRD patterns of the synthesized materials. It is evident that without mixing with gold and manganese precursors, both AuNPs and MnNSs formed amorphous structures (no obvious diffraction peak) [234]. With both gold and manganese precursors, crystalline gold was formed while the Mn species remained amorphous. According to the standard PDF card of gold: #04-

0784, the diffraction peak at 2θ degree = 38.2°, 44.4°, 64.6°, and 77.5° corresponds to 111, 200, 220 and 311 crystal planes, respectively [235]. The intensity of the gold peak in AuMnNPs exhibited an initial increment with the increased amount of Mn, subsequently showing a slight decrease as the mass ratio of Au-Mn decreased to 2 to 1. This indicates the addition of Mn promotes the formation of crystalline gold and reaches a 'saturation point' when the amount of Mn reaches a certain level. As shown in the XPS wide scan spectrum (Figure 30 (b)), the peak area of Mn and Au followed the added amount trend. The oxygen found in Au-contained materials indicates the Au on the material surface could be oxidized. The details can be further investigated by analyzing the narrow scan spectrum. Figure 30 (c) shows gold has two oxidation states among all the materials, which are Au(0) peaks at ~ 84.5 to 85 eV and 88.3 to 88.7 eV and Au(III) peaks at 86.7 to 87 eV and 90.4 to 90.8 eV [236]. The peaks of Au(III) in Mn-contained materials significantly shifted to a higher binding energy level (~0.4 eV), while the Au(0) peaks were relatively consistent. This could be explained by the oxidation of small Au clusters on other oxide surfaces [237, 238]. As a characterization method for shallow surface analysis, the Au signal can still be detected when the Mn content increases, indicating that the thickness of the Mn cladding layer is relatively thin, probably less than 10 nm [239, 240]. The peaks of Mn are highly consistent regardless of the presence or absence of Au (Figure 30 (d)). Two main peaks are at ~654.0 and 642.3 eV, with a distance of 11.7 eV, indicating that the main species is MnO_2 (Mn(IV)) [241]. Another two smaller peaks at ~658.1 and 645.8 eV could be assigned to Mn(II) [242].

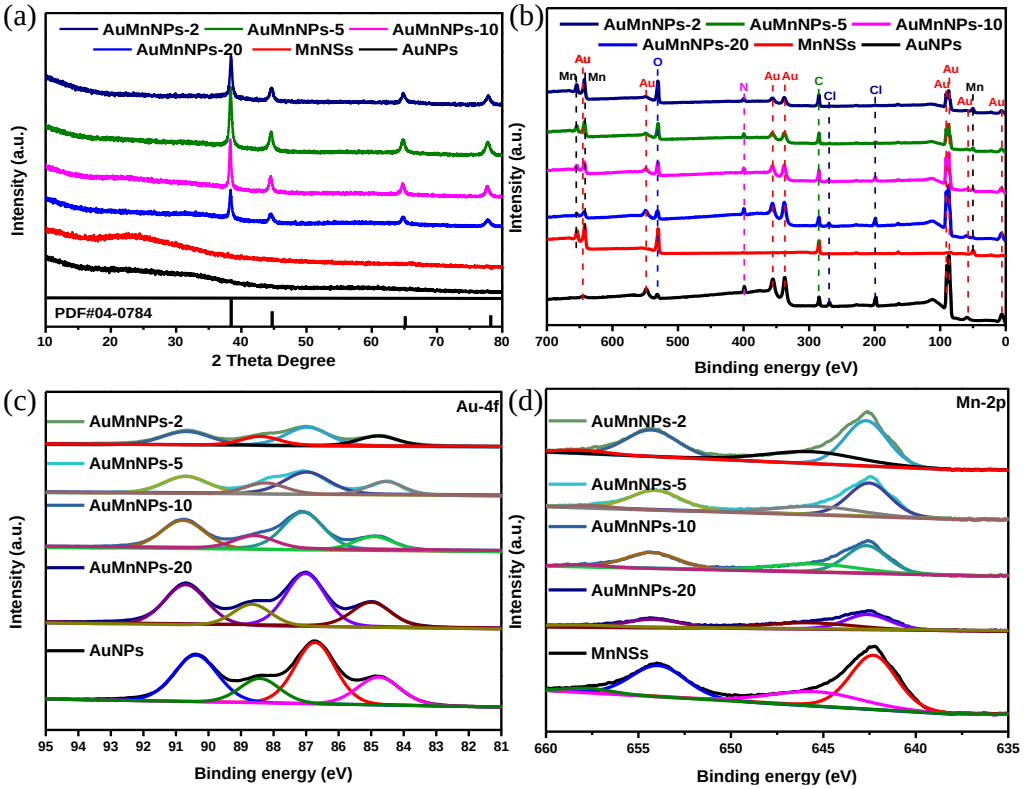

Figure 30. XRD patterns (a), XPS spectra of wide scan (b), and Au-4f (c) and Mn-2p (d) narrow scan of the synthesized nanomaterials.

Figure 31 to Figure 36 show the SEM and TEM characterization of the synthesized materials. From the SEM images, the AuNPs and MnNSs are apparently different from AuMnNPs, especially for MnNSs. A phenomenon was observed: the precipitation rate of Au species was much faster than that of Mn species during the synthesis of AuNPs and MnNSs separately. This leads to the fact that during the synthesis of AuMnNPs, the Mn species that precipitated later may coat the surface of the Au species that precipitated previously. The diameter of AuNPs was around 100 nm while that of Mn-contained nanoparticles was ~75 nm, 94 nm, 105 nm, and 68 nm for AuMnNPs-20, AuMnNPs-10, AuMnNPs-5 and AuMnNPs-2, respectively. On the contrary, MnNSs formed flaky structures instead of spheres. The addition of Mn into Au helped the formation of crystalline Au (refer to XRD result), and no flaky structure was obtained. This indicated that Mn species have an affinity for Au species and helped the crystallization of gold, while Au species also changed the morphology of Mn species. Through the

elemental mapping, it was clear that Mn species were wrapped on the surface of Au species, and the Mn oxides layer grew thicker when the amount of Mn precursors increased. When the Au: Mn ratio reached 2: 1 (AuMnNPs-2), flaky-shaped and bigger spheres (~350 nm) of Mn oxides were formed, while the AuMnNPs grew smaller (~68 nm), indicating the affinity of Mn species to Au species decreased when Mn precursors are in higher concentration. From the EDX spectra, the ratios of Au-Mn in AuMnNPs were consistent with the amount added, suggesting that Au and Mn species were completely precipitated.

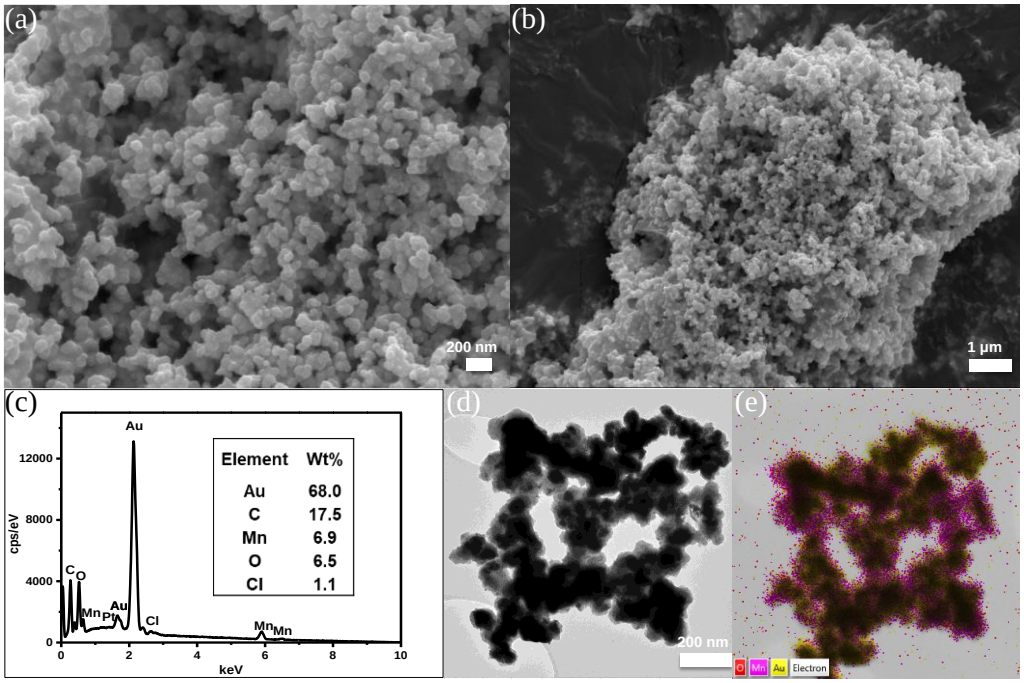

Figure 31. SEM images (a) and (b), EDX spectrum (c), TEM image (d), and EDX layered elemental mapping (e) of AuMnNPs-10.

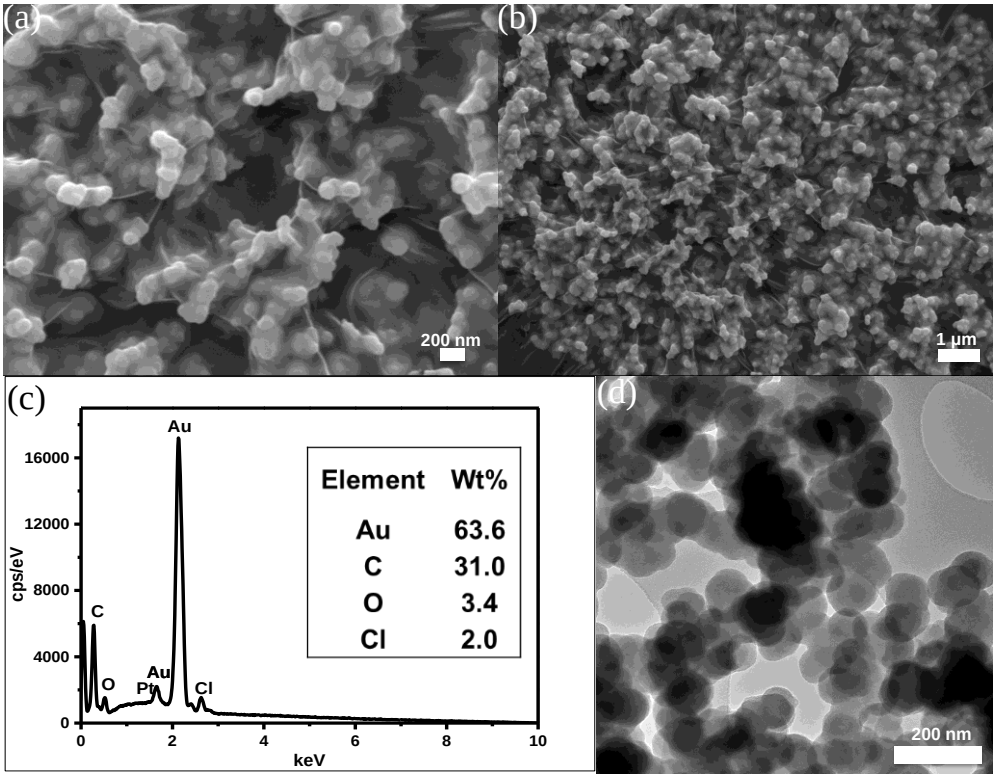

Figure 32. SEM images (a) and (b), EDX spectrum (c), and TEM image (d) of AuNPs.

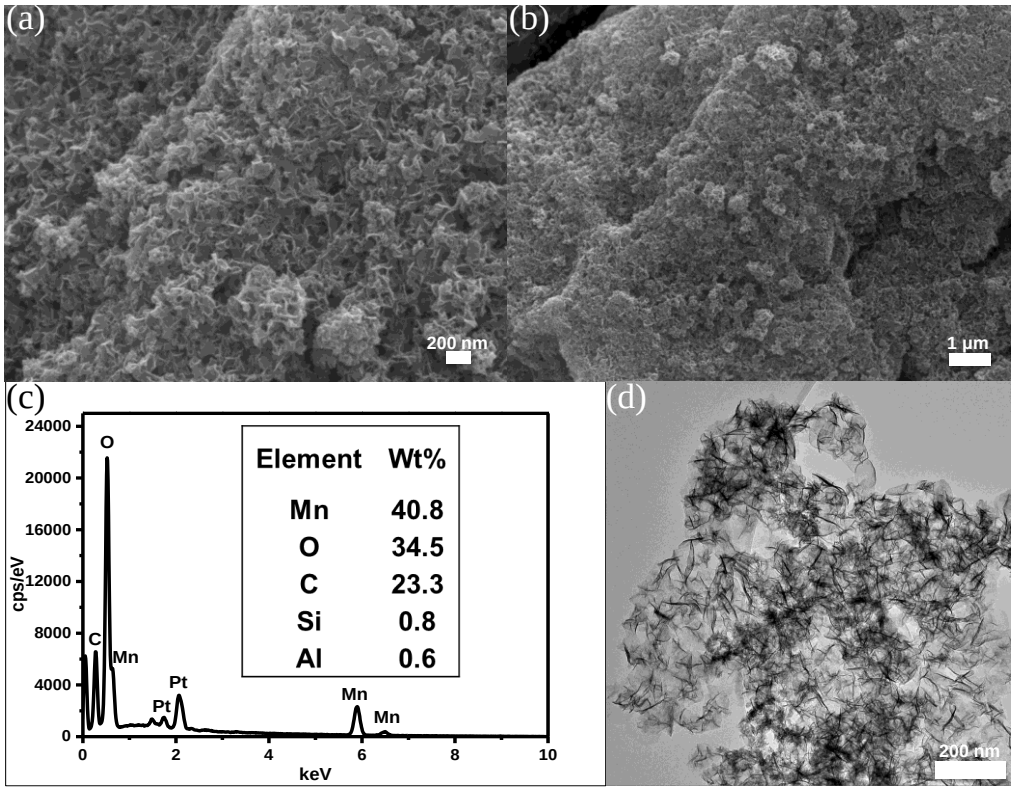

Figure 33. SEM images (a) and (b), EDX spectrum (c), and TEM image (d) of MnNSs.

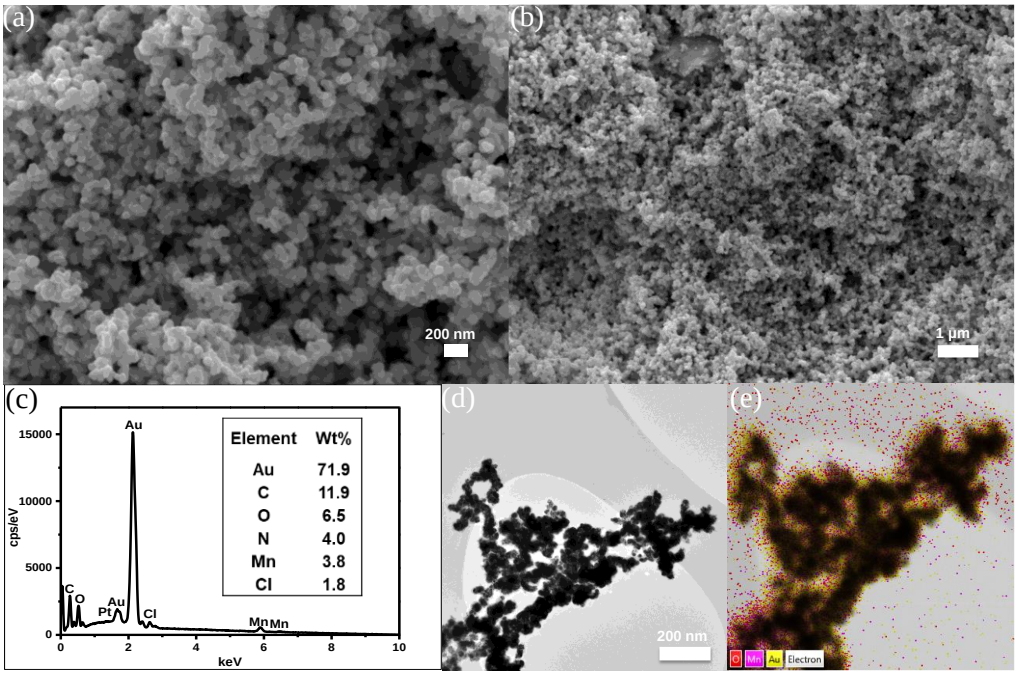

Figure 34. SEM images (a) and (b), EDX spectrum (c), TEM image (d), and EDX layered elemental mapping (e) of AuMnNPs-20.

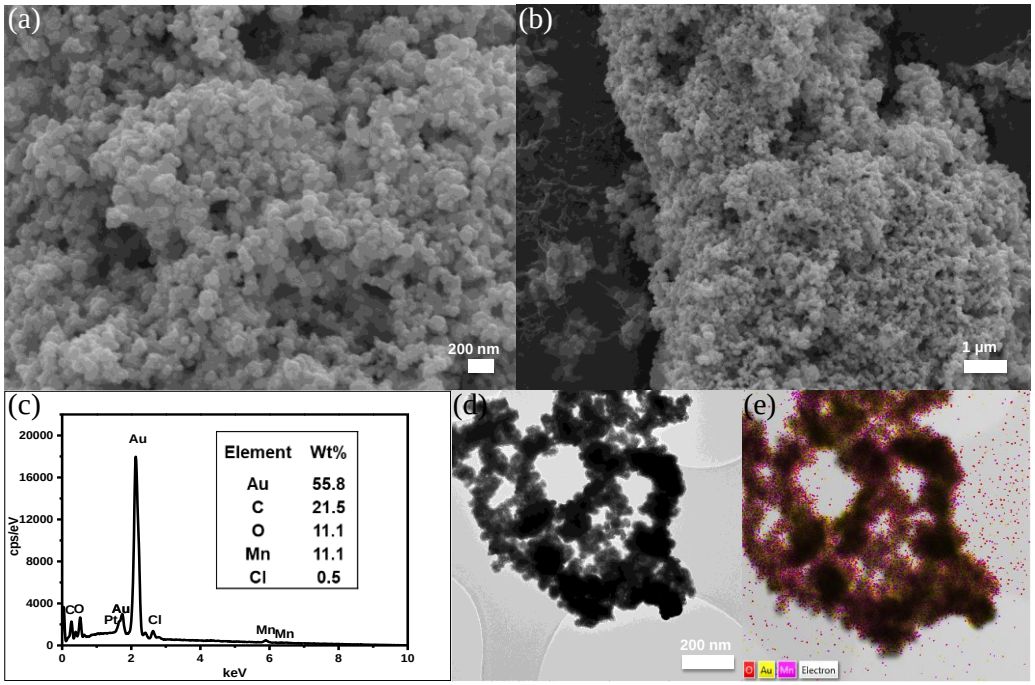

Figure 35. SEM images (a) and (b), EDX spectrum (c), TEM image (d), and EDX layered elemental mapping (e) of AuMnNPs-5.

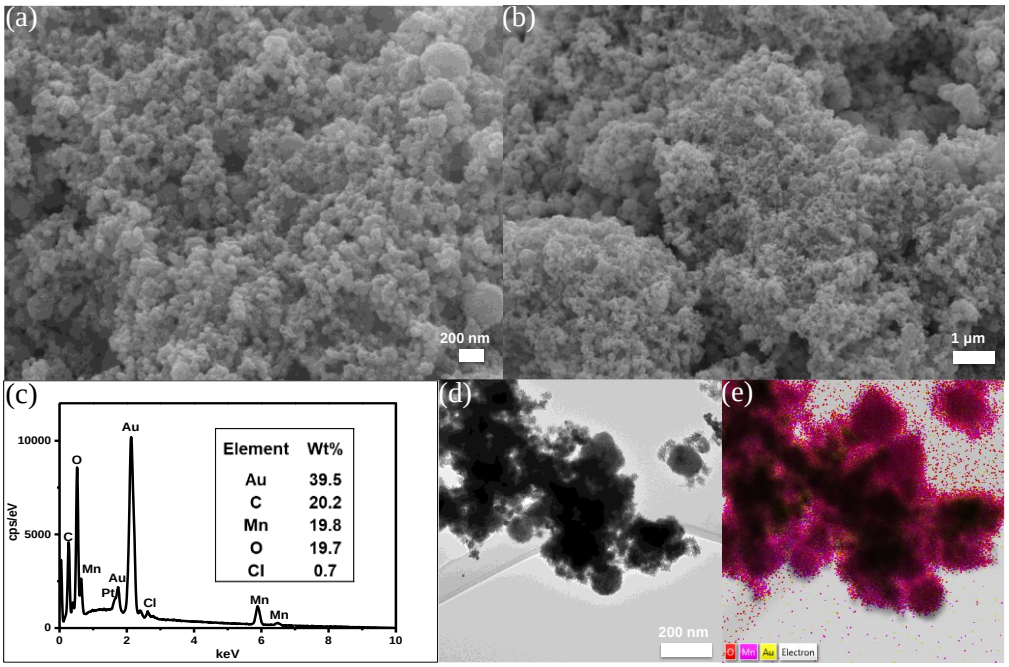

Figure 36. SEM images (a) and (b), EDX spectrum (c), TEM image (d), and EDX layered elemental mapping (e) of AuMnNPs-2.

5.3.2 Electrochemical speciation of As III and V

The synthesized nanomaterials were applied to perform the speciation of As III and V, as illustrated in Figure 7. For total As, a lower reduction potential (-1.1 V) was applied to prompt reactions 2 and 3 to occur during deposition. Simultaneously, both the newly generated As(III) and the As(III) that originally existed in the sample were reduced on a gold electrode (reaction 1) and then determined through the subsequent stripping process (reaction 4). Thus, the rate of reduction of As(V) (reaction 2) cannot be the speed-determining step of the whole As detection process, which leads to an undefined composition ratio of As(V) and As(III). The rate of reaction 2 needs to be greater than reaction 1, and then the signal from total As detection could be obtained. For As(III), a higher reduction potential (0.6 V) was applied to prevent reactions 2 and 3 from occurring so that As(V) would not affect the signal. Consequently, the concentration of As(V) could be calculated by deducting the concentration of As(III) from total As. To prevent reaction 2 from becoming the rate-determining step, efforts were made to enhance both the diffusion rate and the reaction rate.

Since As(V) is more challenging to detect, the optimization was specifically focused on As(V).

As shown in Figure 37, pH, deposition potential, deposition time, Au/Mn ratio in AuMnNPs, and the concentration of AuMnNPs were optimized. Since a highly negative potential was applied to the WE, and As ions are typically negatively charged, the effect of the electric field on the diffusion of As ions must be considered.

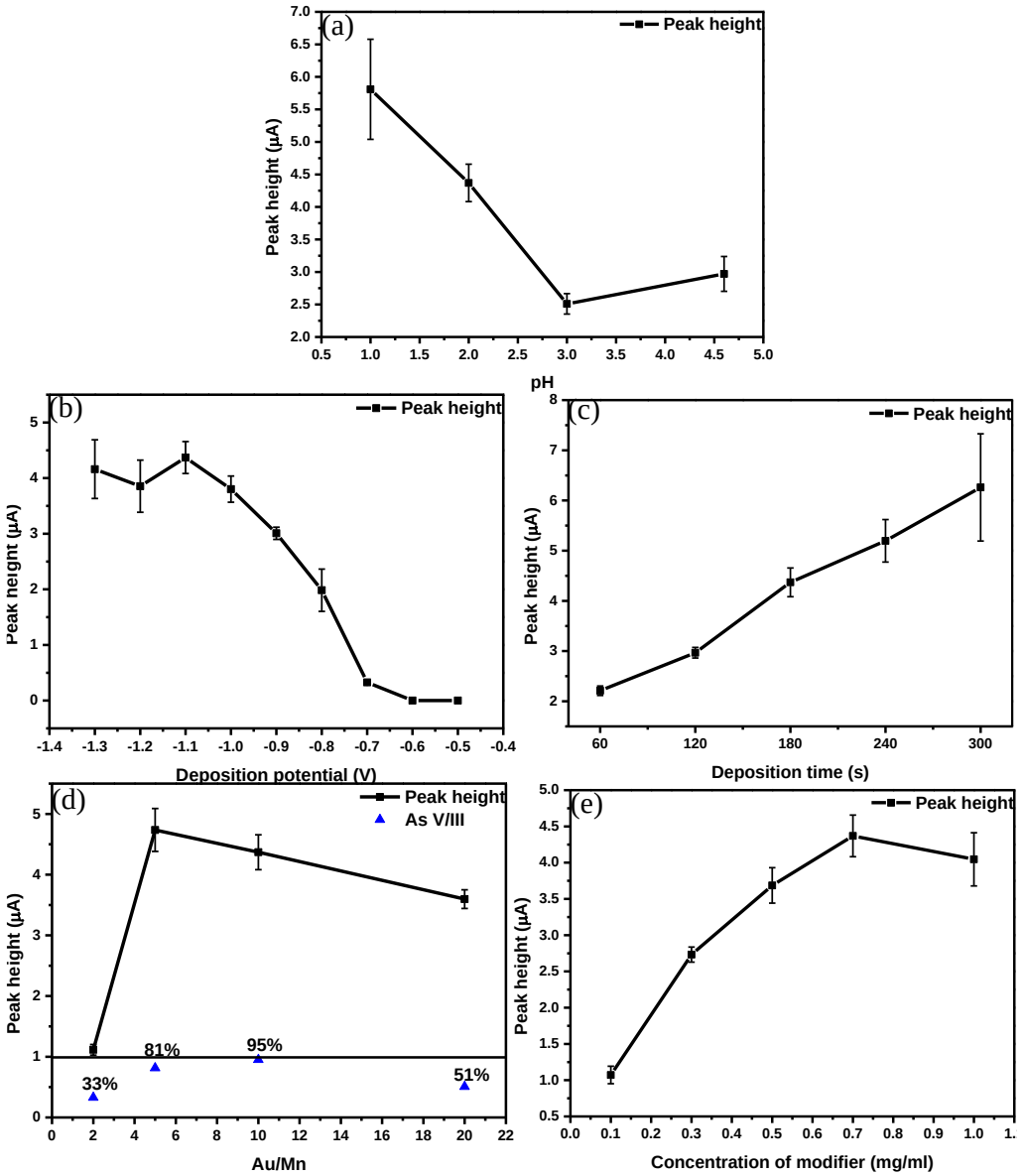

Figure 37. Optimization of parameters for determination of As(V): pH of the electrolyte (a), deposition potential (b), deposition time (c), Au-to-Mn ratio (m/m) in the nanomaterial (d), and concentration of the modifier (e).

According to diffusion simulation with the Nernst-Planck equation [243], the concentration profile near the electrode surface is demonstrated in Figure 38. The numerical simulation parameters: r (electrode radius): 0.2 cm, F (Faraday's constant): 96842, D (diffusion coefficient): $1.11x10^{-5}$ cm^2/s, dt (time interval): 1s, dx (distant increment):50 µm, c0 (initial bulk concentration): 5 µM, R (The gas constant): 8.314 $J \cdot mol^{-1} \cdot K^{-1}$, T (Temperature): 298 K [244]. At the diffusion rate, species with negative charges could be depleted more quickly than the neutral species. As in the case of As(V), the diffusion of charged As(V) towards the electrode surface and the As(V) reduction reaction with metallic Mn (reduced on the electrode) lessen, and thus, reaction 3 is the rate-determined step. If the charges on the As(V) species are eliminated, the issue might be resolved. The pKa values of As(III) are: $pKa_1 = 9.23$, $pKa_2 = 12.13$, $pKa_3 = 13.4$ and that for As(V) are: $pKa_1 = 2.19$, $pKa_2 = 6.89$, $pKa_3 = 11.53$ [145]. As(III) species mainly exist in the form of arsenous acid (H_3AsO_3) when the pH is lower than 9.23, while As(V) species mainly exist in the form of arsenic acid (H_3AsO_4) only when the pH is lower than 2.19. From Figure 37 (a), the signal height increases with a decrease in pH level, and this can be attributed to the fact that the weaker electric field force allows more As(V) to approach the WE surface to facilitate the reaction. However, when the pH reached 1, the phenomenon of hydrogen evolution reaction (HER) became readily apparent, observed by the generation of bubbles. HER represents a competing reaction with reactions 1 and 2, and is able to alter the surface properties of the WE due to the presence of gas bubbles. Thus, although the signal became higher, it was observed that the stability decreased. Consequently, pH 2 was chosen as the optimal condition, which agreed with the hypothesis of the electric migration effect.

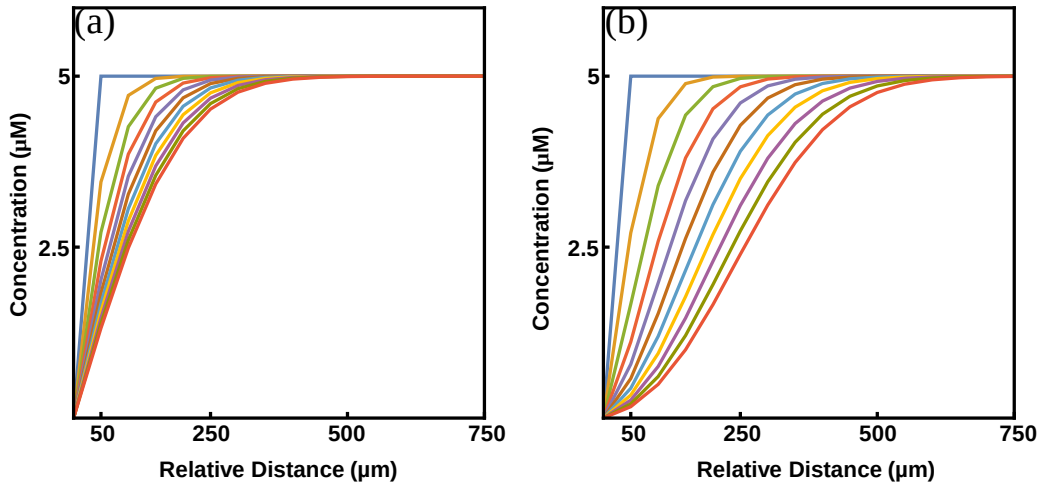

Figure 38. Simulated concentration profile associated with the distance away from electrode surface of As species diffusion (a) with electrical migration , and (b) without electrical migration.

Deposition potential is a critical factor for reaction 1. Due to the high manganese activity, low potential is needed. In Figure 37 (b), the peak appeared only when the potential did not exceed -0.7 V, and it increased as the potential became lower, indicating that the reduction of Mn(II/IV) to Mn(0) starts at -0.7 V. In addition to reaction 3, reactions 1 and 2 also occurred during the deposition process. Consequently, the deposition time was also fine-tuned for optimization. Figure 37 (c) demonstrates an increase in peak height corresponding to an extension in deposition time. However, it is accompanied by a concomitant rise in deviation. Reducing the deposition potential and extending the deposition time resulted in enhanced (HER) and altered the characteristics of the WE. Therefore, a deposition potential of -1.1 V and a deposition time of 180 s were used in further experiments. From the perspective of reaction kinetics, increasing the concentration of reactants is conducive to the forward progress of the reaction. Consequently, increasing the amount of Mn in the nanocomposite is conducive to the progress of reaction 3, leading to a higher production of elemental manganese, thereby accelerating the rate of reaction 2. Furthermore, reaction 1 happens at the active sites on the surface of Au, and since Mn oxides cover the surface of Au, the ratio of Au-Mn and the concentration of AuMnNPs should also

be optimized. Figure 37 (d) shows the peak height increased with the decrease of Au-Mn ratio, indicating that within the ratio of 5~ 20 :1, the increase of Mn does promote the forward progress of reactions 2 and 3, and there are sufficient Au sites for reactions 1 and 4 to proceed. However, the signal decreased dramatically when the Au-Mn ratio reached 2 to 1, which could be caused by the blockage of the Au site by Mn. Moreover, the As(III) with the same concentration was also tested under the same parameters, and the peak height ratio of As(III) to As(V) is also shown. When the Au-Mn ratio is 10 to 1 (AuMnNPs-10), the overlap of peaks of As(III) and As(V) reaches a maximum of 95%. After fixing the Au-Mn ratio, another way to promote the reactions is by increasing the concentration of the reactant (i.e., AuMnNPs). As expected, in Figure 37 (e), the signal increased with the increasing concentration of AuMnNPs. However, the signal decreased a bit when the concentration of AuMnNPs reached 1 mg/mL, which can be attributed to the lower conductivity of AuMnNPs-10 (compared to Au), and the thick layer is not conducive to the conduction of electrical signals. Thus, 0.7 mg/mL of AuMnNPs-10 was considered optimum. It is important to note the differential responses observed with different electrode modifications: using a 0.7 mg/mL AuNPs modified electrode, the response to 2 ppm of As(V) was approximately 0.675 µA, while with the AuMnNPs-10 composite, the response significantly increased to approximately 4.370 µA. Conversely, electrodes modified solely with MnNSs showed no detectable response to 2 ppm of As(V). Due to these disparities in sensitivity and detection capabilities, further studies exclusively utilized the AuMnNPs-10 modified electrodes, as the single-metal modifications (AuNPs and MnNSs) did not yield adequate responses for reliable arsenic speciation.

Under the optimized conditions, the DPV response, the standard calibration curve of As(III) and As(V) separately, and the peak height ratio of As(V) to As(III) are shown in Figure 39 (a) and (b). The peaks for As(III) and As(V), appearing in the range of approximately -0.2 to -0.05 V, did not completely overlap at identical concentration levels; however, the signal ratios remain within 94 to 108% for

concentrations ranging from 0.2 to 2 ppm, which adequately supported effective speciation. Additionally, the oxidation peak observed from 0.05 to 1 V was attributed primarily to the oxidation of molecular hydrogen, a byproduct generated during the deposition process [245, 246].

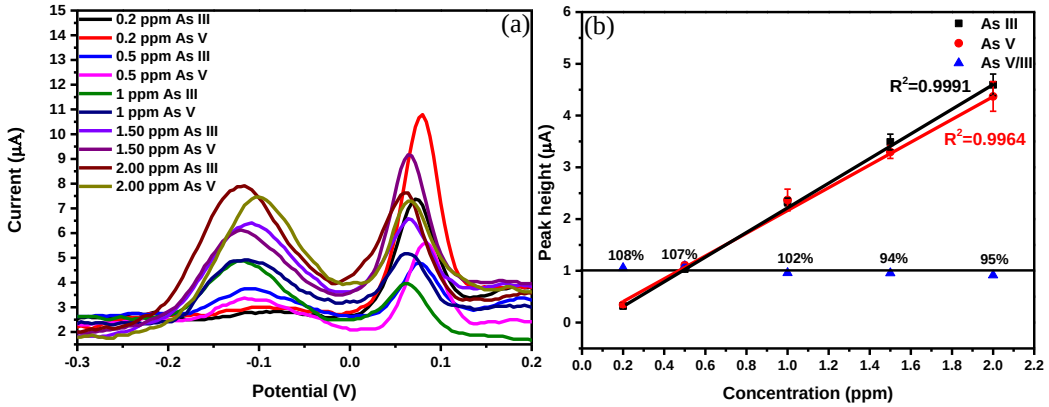

Figure 39. DPV response (a) and calibration curves (b) of 0.2 to 2 ppm As (III and V) standards with linearity.

To get a common calibration curve, the 1: 1(v/v) mixtures of As(III and V) standards were tested, and the response and linearity are shown in Figure 40. The LOD is 0.048 ppm, calculated by 3 times the standard deviation divided by slope, and the linear regression equation was I (µA) = 2.3599C(ppm) − 0.0583.

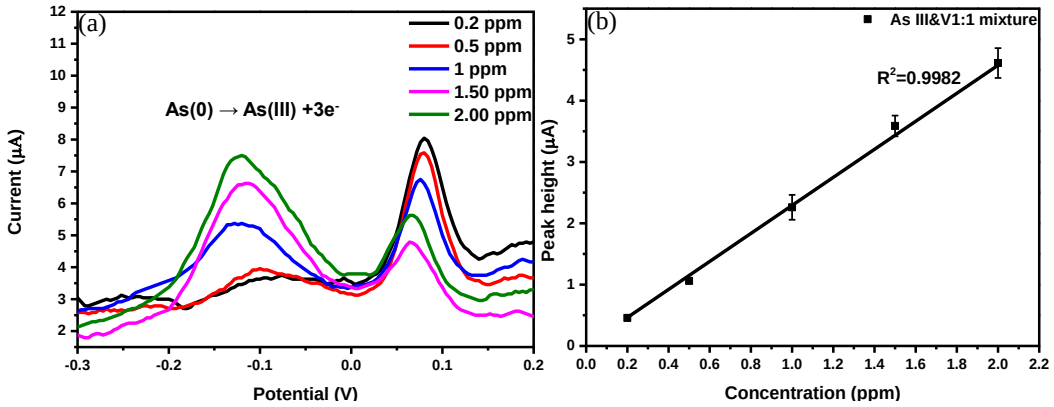

Figure 40. DPV responses (a) and calibration curves (b) of 0.2 to 2 ppm As standards (III and V mixture, 1:1, v/v)

Similarly, the optimization of detecting As(III) under a lower potential was also performed. As shown in Figure 41 (a) and (b), the peak height of As(III) exhibited an increase as the deposition potential decreased and time extended, respectively.

Considering both the prevention of reduction of As(V) and the stability of the electrode signal, -0.6 V and 180 s were identified as the optimal parameters.

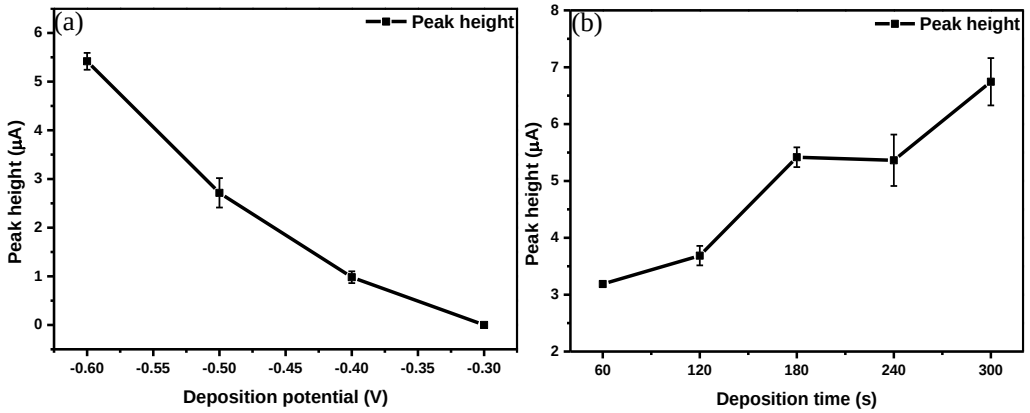

Figure 41. Optimization of parameters for determination of As(III) under lower deposition potentials: deposition potential (a) and deposition time (b).

The DPV response and linearity of As(III) are shown in Figure 42. The LOD was calculated as 0.07 ppm, and the linear regression equation was I (µA)= 2.8361C(ppm) − 0.2917.

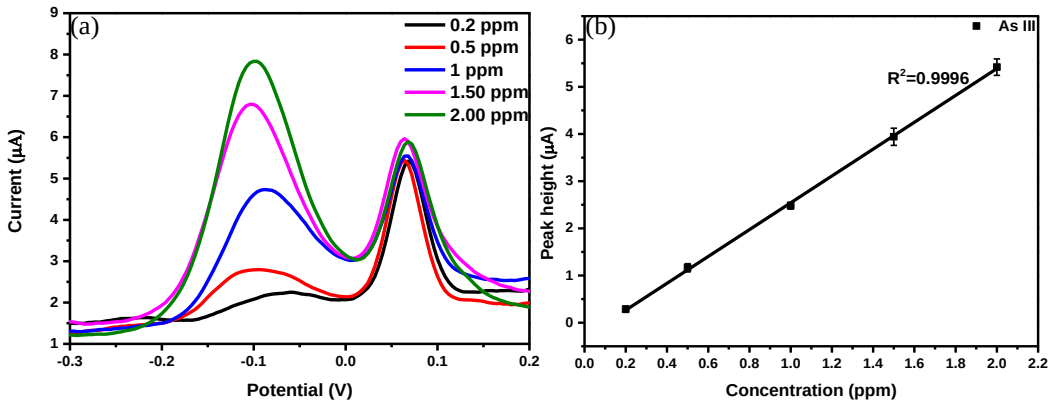

Figure 42. DPV responses (a) and calibration curves (b) of 0.2 to 2 ppm As(III) standards.

As shown in Table 12. Comparative analysis of methodologies between existing studies and current work, a comparative analysis of methodologies between existing studies and current work, previous studies predominantly utilized gold or gold-related materials. These methods often applied relatively higher potentials for detecting As(III), and required lower deposition potentials with the addition of other components (such as Mn and Fe) for As(V) detection. While the

LODs reported in these studies were low, they generally focused on single species of As, necessitating additional treatments to convert and analyze total As. The current work addressed these limitations by enabling simultaneous speciation of As, even though there remained scope for improving the LODs.

Table 12. Comparative analysis of methodologies between existing studies and current work

Analyte	WE	RE	Deposition potential/V	Detection range	LOD	Reference
As(III)	Au	Ag|AgCl	-0.344	10-80 ppb	0.763 ppb	[157]
As(III)	AuNPs	Not mentioned	-0.8	0-150 ppb	16.73 ppb	[247]
As(III)	AuNPs/g-C_3N_4	Calomel electrode	-0.45	0.37-74.92 ppb	0.22 ppb	[248]
As(V)	Mn/Au microwire	Ag|AgCl	-1.35	0-7.49 ppb	0.015 ppb	[159]
As(V)	Fe-based NPs	Ag|AgCl	-1.1	0.025-1 ppm	10 ppb	[249]
As(III)	AuMnNPs-10	Ag|AgCl	-0.6	0.2-2 ppm	70 ppb	This work
As(total)	AuMnNPs-10	Ag|AgCl	-1.1	0.2-2 ppm	48 ppb	This work

5.3.3 Selectivity of AuMnNPs-10-SPCE

The solubilities of common heavy metal arsenates/arsenites (such as $Cu(AsO_2)_2$, $PbHAsO_4$, and $Hg(H_2AsO_3)_2$) are generally very low in most conditions [250-252]. Consequently, the introduction of interfering heavy metal ions into the As standard sample might cause As ions to precipitate, leading to a reduction in peak height. This reduction should not be attributed to a deficiency in the selectivity of the sensors. Therefore, to accurately evaluate the selectivity of the sensors, the peak heights of various interfering ions at the peak position typically observed for As were measured. Nine commonly heavy metal ions (10 and 100 ppm) were tested separately, and their peak height ratios to 1 ppm As(III/V= 1/1, v/v) at ~-0.12 V were recorded. As shown in Figure 43, most of the interfering ions did not show responses at the specific potential, but Cd, Cu, Ni, Hg, and Pb exhibited

high currents. The peaks of Cd, Cu, Ni, Hg, and Pb were not exactly at -0.12 V, but large adjacent peaks could lead to a false signal. In order to mitigate this, SDDC solution was used as a precipitant. Specifically, 10 mg of SDDC was added into a solution (5 mL) containing 100 ppm of all 9 interfering ions, and then the mixture was stirred for 10 min, filtered through a Ø 0.45 µm membrane filter, and tested by AuMn-10-SPCE. After treatment with SDDC, only a 9.82% interference signal was observed, which was considered acceptable. In addition, the presence of surfactants could also influence the performance of the electrode. To evaluate this effect, 10 and 100 ppm of SDS (an anionic surfactant) and PEI (a cationic surfactant) were each added to a 1 ppm mixture of As(III) and As(V) in a 1:1 v/v ratio. As depicted in Figure 43, SDS had minimal impact on the signal, whereas PEI significantly reduced it to less than half. This reduction can be attributed to the adsorption of cationic surfactants on the cathode during the electrodeposition process, leading to the blockage of active sites [253, 254].

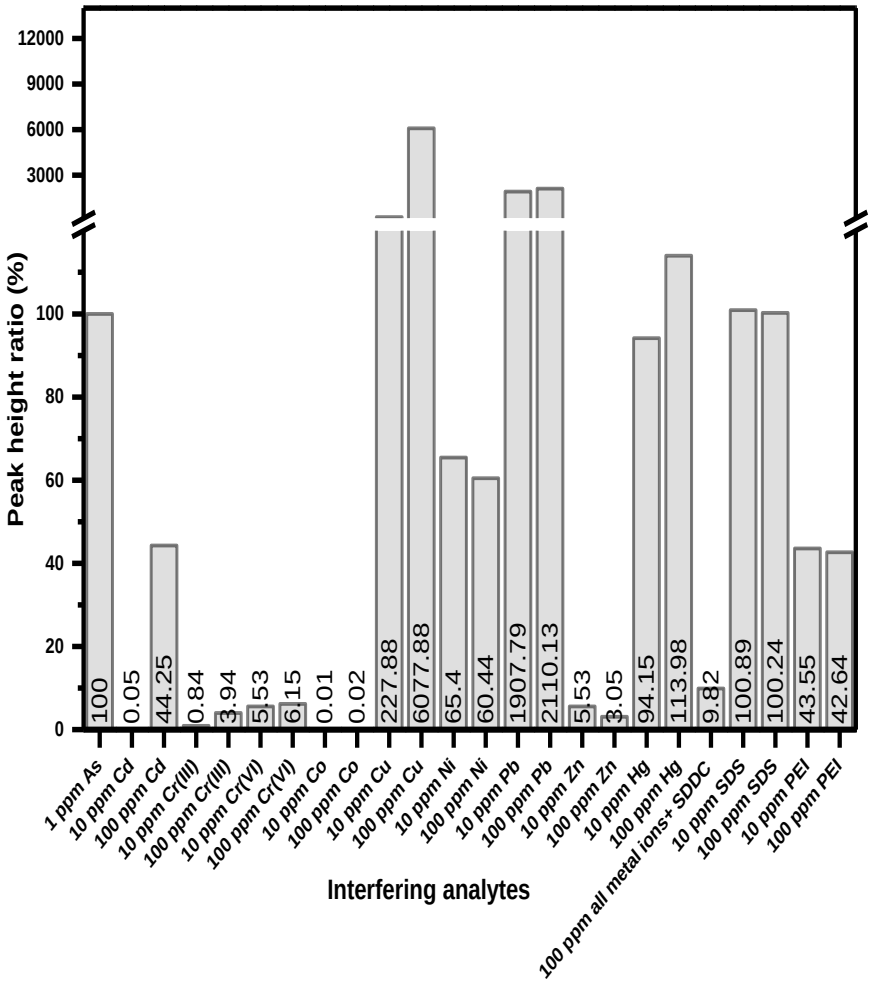

Figure 43. Peak height/current ratio (%, at~ -0.12 V) of interfering ions and surfactants to 1 ppm As (III/V= 1/1, v/v).

5.3.4 Monitoring & speciation of As during wastewater treatment

The HPLC-ICP-QQQ curve and calibration of As (III and V) are shown in Figure 44.

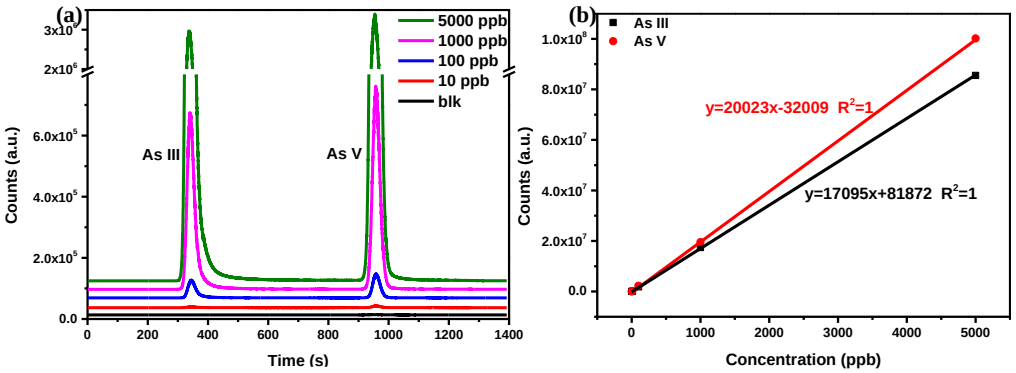

Figure 44. HPLC-ICP-QQQ chromatograms (a) and calibration curves with linearity (b) for As (III and V) standards

For voltammetry detection and speciation, As(III) and total As contents were measured separately, and then the concentration of As(V) was calculated by $C_{As(V)} = C_{As(total)} - C_{As(III)}$. The comparison of results between AnMn-10-SPCE and HPLC-ICP-QQQ is shown in Figure 45 (raw data in Table 13). The observed lower As(III) content compared to As(V) in samples S1 and S2 might be attributed to the oxidation of As(III) to As(V) in the presence of iron hydroxide and oxygen [255]. As in some other studies, the removal efficiency of As(III) by iron hydroxide is not as good as that of As(V) [256, 257]. Consequently, the oxidation of As(III) to As(V) is a necessary step in the treatment of arsenic-contaminated wastewater using iron hydroxides [258]. Notably, the results from both HPLC-ICP-QQQ and AnMn-10-SPCE correlated well across varying ratios of As(III) to As(V) from 0.52 to 4.76. This consistency not only validated the effectiveness of the sensors across different arsenic ratios but also could expand their utility for studying the kinetics of arsenic adsorption by various adsorbents under different conditions.

Table 13. Comparison of results between HPLC-ICP-QQQ and AnMn-10-SPCE

	HPLC-ICP-QQQ			AuMn-10-SPCE		
	As(III)	As(V)	As(total)=As(III)+As(V)	As(total)	As(III)	As(V)=As(total)-As (III)
Raw	6.66	8.63	15.30	15.06 0.10	±6.53 0.22	±8.53

S1	2.28	4.39	6.67	6.6 0.09	±2.37 0.16	±4.23
S2	2.41	2.76	5.17	5.37 0.13	±2.43 0.07	±2.94
S3	2.27	2.20	4.47	4.94 0.22	±2.45 0.05	±2.49
S4	2.76	0.58	3.34	3.47 0.14	±2.41 0.06	±1.06

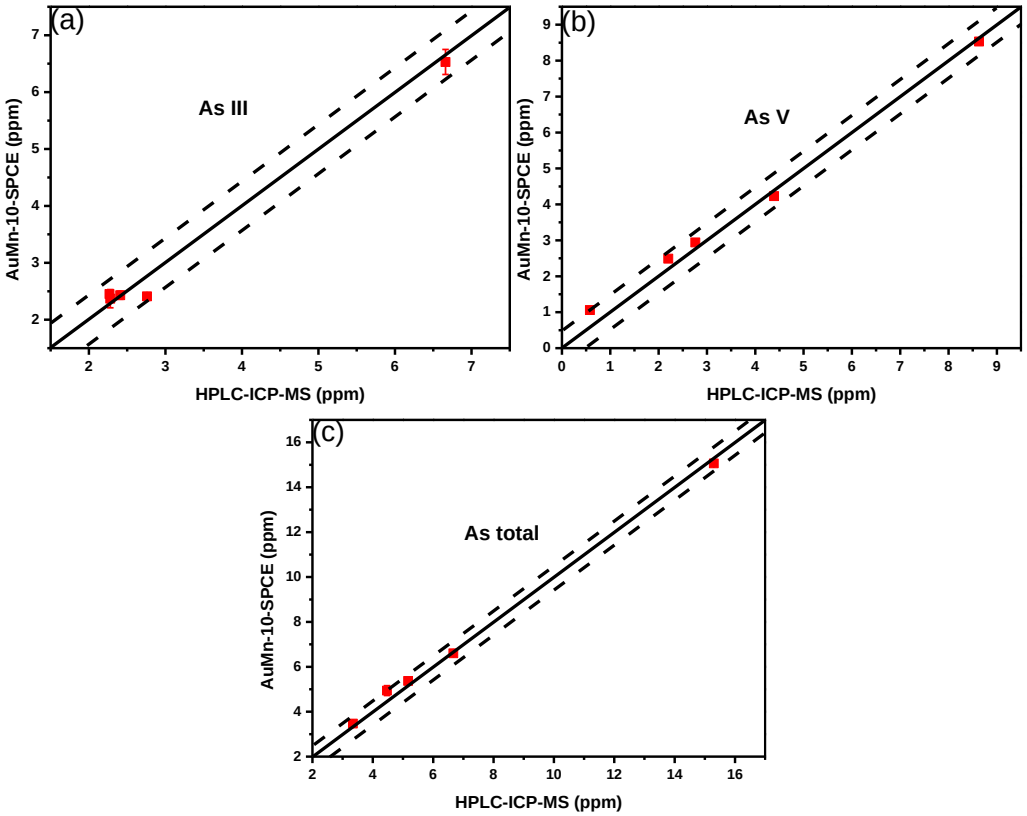

Figure 45. Comparison of monitoring and speciation results of As III (a), As V (b) and As total (c) from As wastewater treatment process obtained by HPLC-ICP-QQQ and AuMn-10-SPCE.

5.4 Conclusion

In this chapter, nanocomposites were synthesized with varying gold-manganese ratios, designed specifically for the speciation of inorganic arsenic (As(III) and As(V)) through voltammetry. The Au-Mn-10 nanocomposite was identified as the optimal formulation, featuring a gold-core-manganese oxide-shell structure

that provided excellent physical characteristics.

Upon optimization, the modified sensor demonstrated robust selectivity for As, achieving a linear detection range from 0.2 to 2 ppm. It exhibited a low LOD of 0.048 ppm for total arsenic and 0.07 ppm for As(III). By applying a dual-channel or multi-channel electrochemical working station, the measurement and speciation of As could be carried out simultaneously.

The sensor was successfully applied to monitor the speciation of As during the treatment process of arsenic-containing environmental samples, with the results aligned closely with those obtained from HPLC-ICP-QQQ.

This study introduces a promising and practical approach for the concurrent determination and speciation of inorganic arsenic using electrochemical sensors modified with gold-manganese oxide nanoparticles.

CHAPTER 6 RAPID ON-SITE DETERMINATION OF HEAVY METALS AND METALLOIDS IN CONTAMINATED BIOCHAR SAMPLES BY ACCELERATED LEACHING PROCESS COUPLED WITH VOLTAMMETRIC SENSORS

6.1 Introduction

The increasing prevalence of industrial waste and environmental contamination has heightened the need for efficient methods to assess the mobility and potential toxicity of heavy metals in various waste materials [2]. TCLP is widely used to determine whether a waste material is classified as hazardous based on its potential to release toxic substances into the environment [259]. Traditionally, TCLP and heavy metal analysis have been performed in laboratory settings, requiring time-consuming sample preparation and complex instrumentation [260]. However, the need for rapid, cost-effective, and field-deployable methods has driven the development of on-site analytical techniques.

In this study, UAL parameters were optimized using a custom-made and portable leaching device to enhance heavy metal and metalloid leaching from biochar samples. The optimized method closely aligned with TCLP results while significantly reducing leaching time from 18 hours to just 30 minutes. After leaching, nanomaterial engineered voltammetric sensors were applied for the simultaneous detection and speciation of As(III and total), Cd(II), Cr(III and VI), Hg(II), Pd(II), and Pb(II) in biochar leachates using screen-printed electrode chips integrated with a portable 8-channel electrochemical working station. Contaminated biochar samples were employed to validate this rapid on-site heavy metal and metalloid analysis approach, and the results were benchmarked against standard techniques, including ICP-OES and HPLC-ICP-QQQ.

6.2 Experimental

6.2.1 Materials and reagents

Sodium(I) hydroxide (NaOH), acetic acid (HAc), sodium(I) arsenite ($NaAsO_2$), sodium(I) arsenate (Na_3AsO_4), chromium(III) nitrate nonahydrate ($Cr(NO_3)_3 \cdot 9 H_2O$), potassium(I) dichromate(VI) ($K_2Cr_2O_7$), lead(II) nitrate ($Pb(NO_3)_2$), cadmium(II) nitrate tetrahydrate ($Cd(NO_3)_2 \cdot 4 H_2O$), palladium(II) acetate ($Pd(OCOCH_3)_2$), sodium(I) phosphate monobasic (NaH_2PO_4), sodium(I) sulfate (Na_2SO_4), ethylenediaminetetraacetic acid disodium(I) salt dihydrate ($Na_2EDTA \cdot 2 H_2O$), ammonium carbonate ($(NH_3)_2CO_3$) and individual standard ion solutions of 1000 ppm lead (Pb II), cadmium (Cd II), chromium (Cr III and VI), palladium (Pd II) and mercury (Hg II) for ICP-OES were purchased from Merck Pte. Ltd (Singapore). 1000 ppm As(III) and 1000 ppm As(V) standards were purchased from inorganic Ventures (Singapore). DI water with a resistivity of less than 18.2 MΩ·cm was obtained from a Millipore Milli-Q purification system to prepare solutions. Raw biochar samples were obtained from Bluefield Renewable Energy Pte. Ltd. (BRE, Singapore).

6.2.2 Apparatus

The commercial SPCE (DRP-C110, Metrohm) was used directly for Cd(II) and Pb(II); screen-printed gold electrode (DRP-220BT, Metrohm) was used for Hg(II), screen-printed carbon electrode modified with bismuth oxide nanosheets (BiONS), activated/non-activated silver-gold nanoparticles (Ag-Au-SPCE-a/ Ag-AuNPs) and Au-Mn oxides nanoparticles (Au-MnNps) by the previously developed methods (the corresponding names of modified electrodes are BiONS-SPCE, Ag-Au-SPCE-a, Ag-Au-SPCE and AuMnNPs-10-SPCE, respectively) was used for Pd(II), Cr(III), Cr(VI), As(III and total), respectively. All the electrodes are disposable and designed for single use. The electrochemical measurements were performed by a multi-potentiostat (µstat8000p, Metrohm). The conventional TCLP process (USEPA SW-846 Method 1311) was conducted using a TCLP Heavy Duty LE tumbler (Reax 20/8) [166]. The UAL was performed by a homemade UAT, as shown in Figure 46. In the middle, there is a

stainless-steel barrel to accommodate a standard TCLP bottle. According to the TCLP standard, 100 g of solid sample should be soaked in 2 L of TCLP solution, and to use 100 g of solid sample is to ensure that enough solid sample volume is included in the test to avoid large deviations of the test results from one batch of sample to another batch of sample [261]. To fulfill this requirement, the barrel was designed to accommodate a TCLP bottle at the size of 2.2 L. Before the UAT was operated, the gap between the barrel and the TCLP bottle was filled with water to minimize the ultrasonic transmission loss from ultrasonic transducers to the bottle. The left side of the UAT includes (1) a motor to rotate the barrel through a shaft; (2) an electronic system to provide high power to ultrasonic transducers and the motor, as well as controlling the device with a microcontroller; and (3) a touch screen to control the operation of UAT through a user-friendly user interface (UI). The right side of the UAT includes two high-power (each at 100W) ultrasonic transducers and a shaft to rotate the transducers together with the barrel. Figure 46 (b) shows that the size of the UAT is 532 mm (L) × 208 mm (W) × 264 mm (H). Figure 46 (c) displays more detail about the components inside the UAT. On the left side, a direct current (DC) motor (with a tunable speed from zero to 60 rpm) was selected to drive the rotation of the barrel for its ease of control in speed. The ultrasound generator is a driver for piezoelectric materials inside the ultrasonic transducers to radiate ultrasonic waves, and the ultrasonic generator is purchased together with the ultrasonic transducer. Arduino Mega 2560 microcontroller is used to program software for controlling the UAT operation through a thin film transistor (TFT) touchscreen's user interface. Arduino sends low-power transistor-transistor logic (TLL) digital signals to solid-state switches connecting to Arduino through a customized home-designed adapter board (customized HAT), and the solid-state switches controlled by TLL signals will turn on the high-power DC motor or ultrasonic generator and tune the motor speed based on settings keyed in via the touch screen. The electronics part also comprises a temperature sensor to monitor the operational temperature inside the left enclosure, and a fan will be turned on to cool down the electronics sealed

in the enclosure when the temperature is high. DC power supply is integrated to supply 5 V and 24 V voltages to Arduino, DC motor, and fan. On the right side, two transducers of 100 W each were selected, operating at 21.7 kHz to sonicate for solid sample leaching. Total element content in the liquid samples was measured by ICP-OES (Avio 550 Max, PerkinElmer, Inc.) HPLC (1260 Infinity II LC System, Agilent Technologies, Inc.) coupled to triple quadrupole ICP-MS (ICP-QQQ, 8900 Triple Quadrupole ICP-MS, Agilent Technologies, Inc.) as a standard method for the speciation of As and Cr.

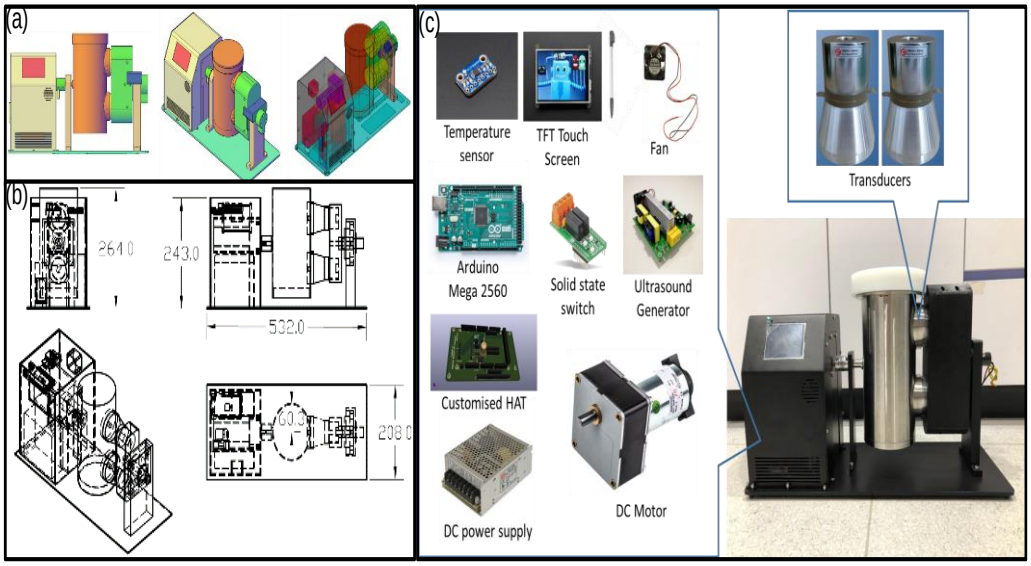

Figure 46. Schematic views of ultrasonic assisted tumbler (UAT). 3D prototype design view and the view of the components inside the tumbler (a), the size of the UAT at 532mm (L) x 208mm (W) x 264mm (H) (b), the components inside UAT and the assembled UAT (c).

6.2.3 Preparation of artificially contaminated biochar (ACB), spiked biochar leachate (SBL), and rapid adsorption (RA) test samples

Due to the low heavy metal and metalloid contents in the raw biochar TCLP leachate samples, specific heavy metal and metalloid ions were spiked into the biochar to simulate spent/contaminated biochar typically generated after water purification. The artificially contaminated biochar (ACB) samples were prepared in three separate groups to prevent interaction and precipitation: (i) ACB1: 0.274 g of $Cd(NO_3)_2 \cdot 4H_2O$, 0.160 g of $Pb(NO_3)_2$, 0.211 g of $Pd(OCOCH_3)_2$, 100 mL of Hg(II) standard (1000 ppm) and 400 mL of DI water; (ii) ACB2: 0.770 g of

$Cr(NO_3)_3 \cdot 9H_2O$, 0.566 g of $K_2Cr_2O_7$ and 500 mL of DI water, and (iii) ACB3: 0.173 g of $NaAsO_2$, 0.277 g of Na_3AsO_4 and 500 mL of DI water.

Each heavy metal or metalloid salt was dissolved in DI and then added to 100 g of raw biochar, achieving a final concentration of 0.1 mg g^{-1} in biochar. The volume of liquid was sufficient to fully submerge the biochar. The samples were kept at room temperature (RT) for three days, then dried in an oven at 70 °C in preparation for leaching tests. No interactions or precipitation occurred within the groups, either in solution or after drying. After sieving, all biochar samples were found to have diameters of less than 1 cm, meeting TCLP requirements. A workflow diagram was provided in Figure 47 to illustrate the process and methodology.

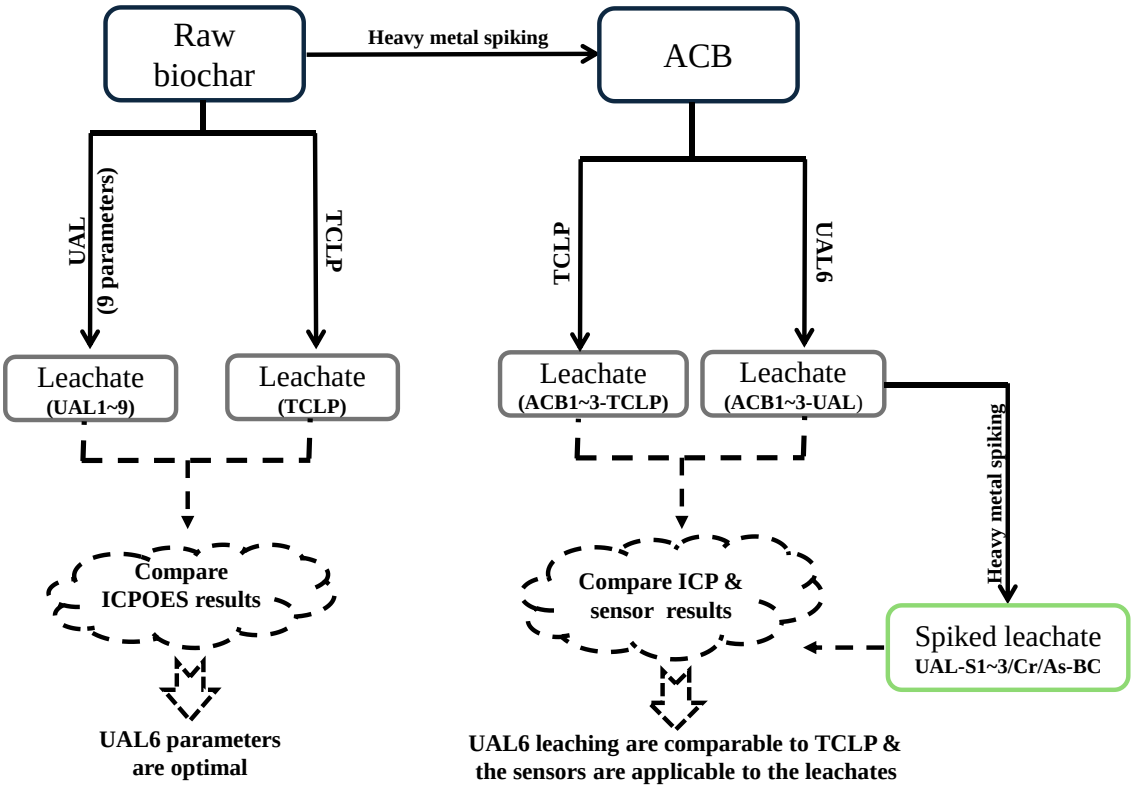

Figure 47. Workflow diagram of the process and methodology.

After TCLP and UAL leaching, the leachates from them were labeled as ACB1/2/3-TCLP, ACB1/2/3-UAL. To further evaluate the performance of the sensors for the leachate samples, all ions were spiked into raw UAL leachate

(UAL6) at different concentrations (listed in Table 14) and kept at RT for ten days to study the concentration change (for all ions) and valance change (for Cr and As). To further investigate the adsorption properties of biochar and better understand the leaching behaviour of ACB samples, the biochar was added to the SBL at a liquid-to-solid ratio of 20:1 and the mixture was rotated in the tumbler at 30 rpm. The leaching tests for each UAL or TCLP condition were conducted in triplicate. The labels of the samples are also listed in Table 14. All the samples were tested by voltammetric sensors and verified by ICP-OES and/or HPLC-ICP-QQQ.

Table 14. Spiking details and treatments of the samples.

Sample label	Spiked ions & concentrations	Treatment
UAL-As-1	As(III and V), 0.5 ppm each	Kept at room temperature(RT) for 10 days
UAL-As-2	As(III and V), 5 ppm each	Kept at RT for 10 days
UAL-As-3	As(III and V), 50 ppm each	Kept at RT for 10 days
UAL-As-BC	As(III and V), 50 ppm each	Treated by biochar
UAL-Cr-1	Cr(III and VI), 5 ppm each	Kept at RT for 10 days
UAL-Cr-2	Cr(III and VI), 50 ppm each	Kept at RT for 10 days
UAL-Cr-3	Cr(III and VI), 100 ppm each	Kept at RT for 10 days
UAL-Cr-BC	Cr(III and VI), 100 ppm each	Treated by biochar
UAL-S1	0.1 ppm Hg(II) and Cd(II); 1 ppm Pb(II) and Pd(II)	Kept at RT for 10 days
UAL-S2	1 ppm Hg(II) and Cd(II); 10 ppm Pb(II) and Pd(II)	Kept at RT for 10 days
UAL-S3	10 ppm Hg(II) and Cd(II); 100 ppm Pb(II) and Pd(II)	Kept at RT for 10 days
UAL-BC	10 ppm Hg(II) and Cd(II); 100 ppm Pb(II) and Pd(II)	Treated by biochar

6.2.4 Ultrasonic-assisted leaching parameters

UAL parameters are listed in Table 15. The total tumbling time was fixed at 30 min, while the tumbling speed changed from 30 rpm to 60 rpm, and the sonication time changed from 10 min to 30 min to evaluate the effects of each parameter.

Table 15. UAL parameters.

UAL No.	Tumbling speed/rpm	Sonication time/min	Tumbling time/min

1		10	
2	30	20	
3		30	
4		10	
5	45	20	30
6		30	
7		10	
8	60	20	
9		30	

6.2.5 Electrochemical measurements

The electrochemical measurements were conducted by directly applying 100 µL of leachate solutions obtained from spiked biochar samples onto the electrodes. Exceptions included Cr(III), which was adjusted to pH 13 using 1 M NaOH, and As(III and V), which was adjusted to pH 2 using 1 M HCl. Differential pulse voltammetry (DPV) was employed for all heavy metal and metalloid ions, except Cr(VI), for which linear sweep voltammetry (LSV) was used. Deposition potentials and times were optimized for Pb(II), Cd(II), and Hg(II), while previously established protocols were applied for Cr(III/VI), As(III/total), and Pd(II) [187, 188, 262]. Specifically, Cr(III) and Cr(VI) were measured using Ag-Au-SPCE-a and Ag-AuNPs, respectively, and Cr(total) was calculated by summing the contents of Cr(III) and Cr(VI). While As(total) and As(III) were determined using AuMnNPs-10-SPCE at -1.1 V and -0.6 V, respectively, and the content of As(V) was calculated by subtracting As(III) from As(total). The final protocols for the ions are listed in Table 16.

Table 16. Electrochemical protocols of the heavy metal ions.

Ions	As(III)	As(V)	Cd(II)	Cr(III)	Cr(V)	Hg(II)	Pb(II)	Pd(II)
Method	DPV	DPV	DPV	DPV	LSV	DPV	DPV	DPV
Deposition potential/V	-0.6	-1.1	-1.2	-0.2	0.6	-0.3	-1.5	-0.8
Deposition time/s	180	180	150	120	120	120	180	120
Begin potential/V	-0.6	-1.1	-1.2	-0.2	0.6	-0.3	-1.5	-0.8
End potential/V	0.5	0.5	0	0.3	-0.6	0.7	-0.2	0.8
Step potential/V	0.004	0.004	0.005	0.008	0.005	0.002	0.005	0.008
Amplitude potential/V	/	/	/	/	0.002	/	/	/
Frequency/Hz	/	/	/	/	25	/	/	/
Puls potential/V	0.04	0.04	0.1	0.05	/	0.05	0.1	0.05
Puls time/ms	80	80	80	80	/	80	80	80
Scan rate/$V \cdot s^{-1}$	0.02	0.02	0.01	0.04	/	0.04	0.01	0.02

All of these parameters were simultaneously applied together on the 8-channel potentiostat, enabling the concurrent detection of 8 different heavy metal and metalloids ions. The mean values and standard deviations (SD) were calculated from triplicated measurements and are presented numerically or as error bars. The whole on-site testing process, including sample weighing, extraction fluid addition, sample loading, accelerated leaching, leachate filtration, leachate application, and voltammetric analysis, is illustrated in Figure 48.

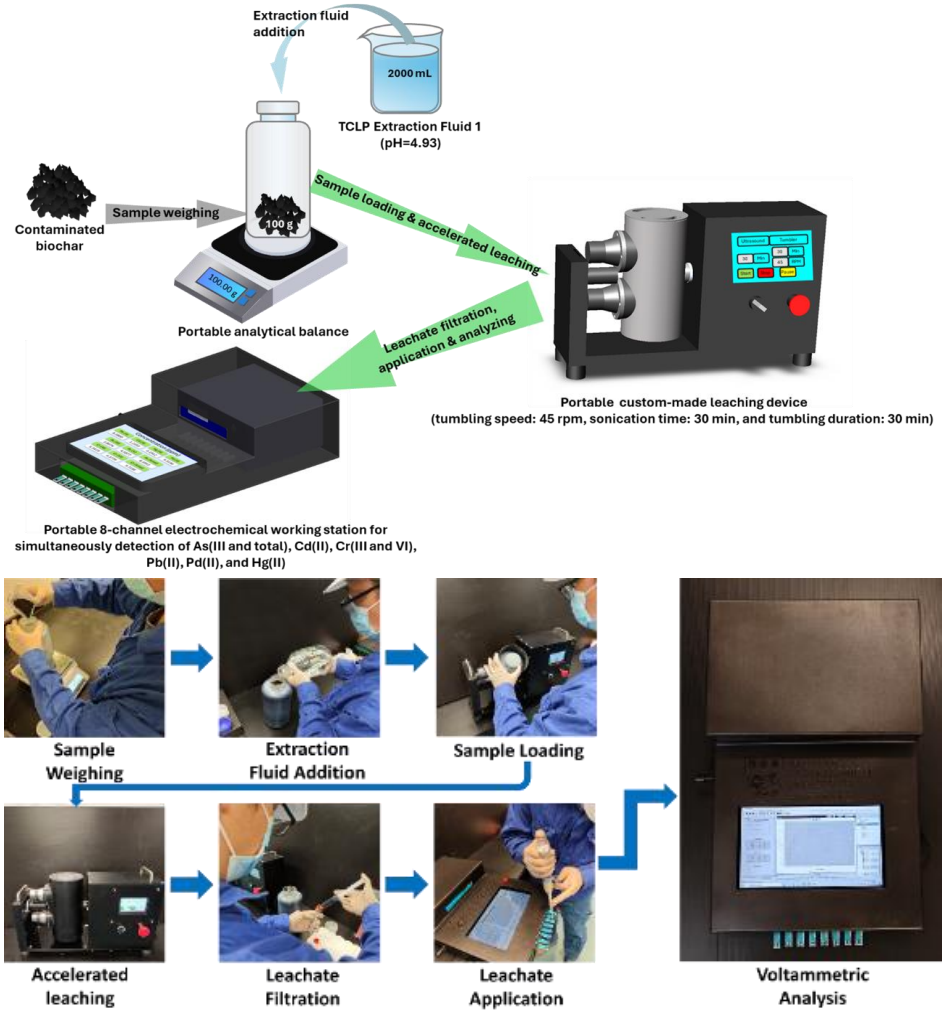

Figure 48. Detailed illustration of the complete on-site sample testing workflow

6.2.6 ICP-OES and HPLC-ICP-QQQ analysis

The concentrations of various elements (Ag, Al, As, Ba, Cd, Cr, Cu, Fe, Mn, Ni, Pb, Se, Sn, Ti, Zn, and Hg) in the samples were measured using ICP-OES, with calibration standards set at 0.1, 1, 10, 20, and 50 ppm. The calibration curves for each element exhibited R^2 values greater than 0.999, indicating high accuracy.

For the speciation of Cr(III) and Cr(VI), samples were mixed with 100 mM Na_2EDTA solution (pH= 6, with 1/9 volume of the sample) and incubated in an oven at 60 °C for 1 hour to complex Cr(III) with EDTA. Notably, Cr(VI) was not reduced to Cr(III) under these conditions [188]. HPLC analysis was performed using a 100 µL injection volume and a G3268-80001 column (Agilent Technologies, Inc.). The mobile phase consisted of 5 mM NaH_2PO_4, 15 mM Na_2SO_4, and 5 mM Na_2EDTA (pH = 7), with a flow rate of 1 $mL \cdot min^{-1}$ and an elution cycle of 5 minutes. The monitored mass-to-charge ratio (m/z) for Cr was 52 in the ICP-QQQ analysis.

For As(III) and As(V) speciation, HPLC-ICP-QQQ analysis was conducted using a G3288-80000 column (Agilent Technologies, Inc.) with a 100 µL injection volume. The mobile phase consisted of solutions A (5 mM $(NH_3)_2CO_3$) and B (50 mM $(NH_3)_2CO_3$) with a flow rate of 1 $mL \cdot min^{-1}$. The elution procedure was as follows: 100% A from 0 to 1 minute, 100% B from 6 to 16 minutes, and 100% A from 16 to 19 minutes. The monitored m/z for As was 75 in the ICP-QQQ analysis.

6.3 Results and discussion

6.3.1 Comparison between UAL and TCLP

As the concentrations of most analytes, including those more concerned heavy metals and metalloids such as As, Cd, Cr, Pb, Pd, and Hg, were below the lowest standard concentration (0.1 ppm) in the raw biochar leachate samples, only five elements (Al, Fe, Si, Ti and Zn) with higher concentrations are listed and compared in Table 17. The leaching behaviors of Al and Si were more related to the tumbling speed as their concentrations increased with the increase in tumbling speed. For Fe, Ti, and Zn, the concentrations were more or less at the same level of TCLP, indicating they are easier to reach equilibrium with than other elements.

The *t*-test was conducted for each set, and the *p* values are also shown in the table. Most ions show no statistical significance ($p > 0.05$) with TCLP. Since UAL6 result has the least number of ions that have statistically significant differences with TCLP, it was selected as the optimized UAL method. The following UAL of ACBs were performed with UAL6 parameters.

Table 17. Comparison of UAL and TCLP results of raw biochar.

Sample/element (ppm)		Al	Fe	Si	Ti	Zn
UAL1	Mean value ± SD	0.14±0.004	0.373±0.104	4.4135±0.104	0.1635±0.0242	0.11±0.008
	p-value (Vs. TCLP)	0.1489	0.7903	0.2307	< 0.0001	0.0697
UAL2	Mean value ± SD	0.138±0.003	0.502±0.175	4.3578±0.0267	0.1982±0.0087	0.105±0.007
	p-value (Vs. TCLP)	0.1699	0.2640	0.0012	< 0.0001	0.0602
UAL3	Mean value ± SD	0.111±0.048	1.317±0.482	5.2459±0.7497	0.3017±0.0463	0.228±0.084
	p-value (Vs. TCLP)	0.8345	0.0273	0.1595	0.0015	0.6393
UAL4	Mean value ± SD	0.1892±0.0039	0.5224±0.1502	6.0349±0.0153	0.2322±0.0214	0.108±0.016
	p-value (Vs. TCLP)	0.0138	0.1776	< 0.0001	< 0.0001	0.0707
UAL5	Mean value ± SD	0.1919±0.0034	0.4434±0.0403	6.0282±0.0521	0.2199±0.0216	0.1±0.009
	p-value (Vs. TCLP)	0.0123	0.2229	< 0.0001	< 0.0001	0.0514
UAL6	Mean value ± SD	0.1171±0.029	0.383±0.0317	5.644±0.7618	0.2865±0.0696	0.169±0.071
	p-value (Vs. TCLP)	0.6360	0.6108	0.0599	0.0043	0.6224
UAL7	Mean value ± SD	0.1984±0.005	0.4029±0.0108	6.3814±0.2262	0.2151±0.0191	0.1±0.007
	p-value (Vs. TCLP)	0.0098	0.4299	0.0001	< 0.0001	0.0482
UAL8	Mean value ± SD	0.1978±0.0064	0.539±0.3138	6.5619±0.036	0.2594±0.0361	0.113±0.016
	p-value (Vs. TCLP)	0.0102	0.3762	< 0.0001	0.0004	0.0814
UAL9	Mean value ± SD	0.2039±0.0028	0.5027±0.2314	6.5674±0.0096	0.2196±0.0663	0.102±0.036
	p-value (Vs. TCLP)	0.0078	0.3541	< 0.0001	0.0015	0.0809
TCLP	Mean value ± SD	0.1037±0.0351	0.3488±0.1062	4.4989±0.0128	0.5361±0.0246	0.198±0.062

After spiking heavy metal and metalloid ions, the leaching behavior of ACBs was changed accordingly. As shown in Table 18 to Table 20, slightly more Al was leached, resulting in higher concentrations in ACB samples compared to raw biochar [263, 264]. Heavy metal and metalloid ions such as Fe, Cr, and As might interact with other heavy metals through redox reactions and co-precipitation/adsorption effects [265-269]. The concentrations of Zn in As- and Cr-spiked ACBs, as well as those of Fe and Ti in all ACBs, fell below the detection limits of ICP-OES.

It was observed that the leaching amounts of the spiked heavy metal and metalloid ions varied despite all ions being initially added in equal quantities, with most being partially immobilized by the biochar. Notably, the concentrations of Cr in

spiked samples were significantly reduced to less than 0.1 ppm, highlighting the strong retention capability of biochar for Cr. Although the leaching behaviors of other spiked ions differed between TCLP and UAL, their concentrations were numerically stable and within the same order of magnitude, allowing for correction factors.

For As-spiked samples, speciation results obtained from HPLC-ICP-QQQ indicated concentrations of 4.9750 ± 0.0014 and 4.2590 ± 0.0011 ppm for As(III) and 42.9085 ± 0.0121 and 32.0007 ± 0.0105 ppm for As(V) in ACB3-TCLP and ACB3-UAL, respectively. Speciation analysis revealed that the differences in total arsenic content between TCLP and UAL leachates were primarily due to variations in As(V) concentrations, underscoring the critical role of speciation in understanding the leaching process.

The primary advantage of the UAL is its ability to significantly reduce the leaching time of TCLP (from 18 hours to 30 min), enabling rapid on-site detection. While UAL results differed slightly from TCLP in some cases, the optimization of UAL parameters ensured that the leaching performance was closely aligned with TCLP outcomes. This makes the proposed leaching device and UAL a practical and efficient alternative for field applications, particularly for biochar samples.

Table 18. Comparison of UAL and TCLP results of ACB 1

Element/sample (ppm)	ACB1-TCLP Mean value ± SD	ACB1-UAL Mean value ± SD	Factor (TCLP/UAL)	*p*-value (Vs. TCLP)
Al	0.2101 ± 0.026	0.2979 ± 0.0315	0.7053	0.0204
Fe	< 0.1	< 0.1	/	/
Si	13.2344 ± 0.1907	12.7414 ± 0.3443	1.0387	0.0959
Ti	< 0.1	< 0.1	/	/
Zn	0.6884 ± 0.0114	0.6091 ± 0.0726	1.1302	0.1349
As	< 0.1	< 0.1	/	/
Cd	35.2473 ± 2.217	31.5128 ± 1.1835	1.1185	0.0618
Cr	< 0.1	< 0.1	/	/
Pb	1.4723 ± 0.2065	3.3086 ± 0.2659	0.445	0.0007
Pd	0.8137 ± 0.1397	1.7471 ± 0.0774	0.4657	0.0005
Hg	4.1142 ± 0.0975	2.0945 ± 0.1086	1.9643	<0.0001

Table 19. Comparison of UAL and TCLP results of ACB 2

Element/sample (ppm)	ACB2-TCLP Mean value ± SD	ACB2-UAL Mean value ± SD	Factor (TCLP/UAL)	p-value (Vs. TCLP)
Al	0.2886 ± 0.0121	0.3026 ± 0.0034	0.9537	0.1266
Fe	< 0.1	< 0.1	/	/
Si	13.3523 ± 0.2729	13.1283 ± 0.1999	1.0171	0.3154
Ti	< 0.1	< 0.1	/	/
Zn	< 0.1	< 0.1	/	/
As	< 0.1	< 0.1	/	/
Cd	< 0.1	< 0.1	/	/
Cr	< 0.1	< 0.1	/	/
Pb	< 0.1	< 0.1	/	/
Pd	< 0.1	< 0.1	/	/
Hg	< 0.1	< 0.1	/	/

Table 20. Comparison of UAL and TCLP results of ACB 3

Element/sample (ppm)	ACB3-TCLP Mean value ± SD	ACB3-UAL Mean value ± SD	Factor (TCLP/UAL)	p-value (Vs. TCLP)
Al	0.1163 ± 0.008	0.2155 ± 0.0099	0.5397	0.0002
Fe	< 0.1	< 0.1	/	/
Si	12.8633 ± 0.2277	12.5676 ± 0.0712	1.0235	0.0983
Ti	< 0.1	< 0.1	/	/
Zn	< 0.1	< 0.1	/	/
As	49.3411 ± 0.0491	39.4611 ± 0.0573	1.2504	<0.0001
Cd	< 0.1	< 0.1	/	/
Cr	< 0.1	< 0.1	/	/
Pb	< 0.1	< 0.1	/	/
Pd	< 0.1	< 0.1	/	/
Hg	< 0.1	< 0.1	/	/

6.3.2 Optimization and calibration results of electrochemical method

In addition to the five ions (Pd(II), As(III and V) and Cr(III and VI)) that were established the detection methods previously, three more heavy metal ions (Cd(II), Pb(II) and Hg(II)) were also studied [270, 271]. As shown in Figure 49 (a to d), lower deposition potential and longer deposition time give higher signals of Pb and Cd, but the errors also increase. The stronger signals were attributed to the rapid enrichment of Cd and Pb at low potentials; however, hydrogen evolution reaction (HER) also occurs in this potential range. The hydrogen gas generated during HER could randomly occupy the electrode surface, adversely affecting the deposition of Cd and Pb and interfering with their stripping signals [272]. To

balance signal strength and stability, -1.2 V, 150 s and -1.5 V, 180 s were selected for Cd and Pb, respectively. From -0.1 V to -0.3 V, the intensity of the signal of Hg(II) first increases and then continues to weaken at voltages lower than -0.3 V (Figure 49 e), which is similar to that observed by Nguyen *et al*. [273]. It was believed that using gold as the working electrode could reduce the overpotential of HER, which occurred when the potential was below -0.3 V, leading to a reduction in signal strength and stability [274]. Therefore, the optimal parameters selected for Hg(II) were a deposition potential of -0.3 V and a deposition time of 120 s. As mentioned above, the optimized parameters for all the analytes are listed in Table 16.

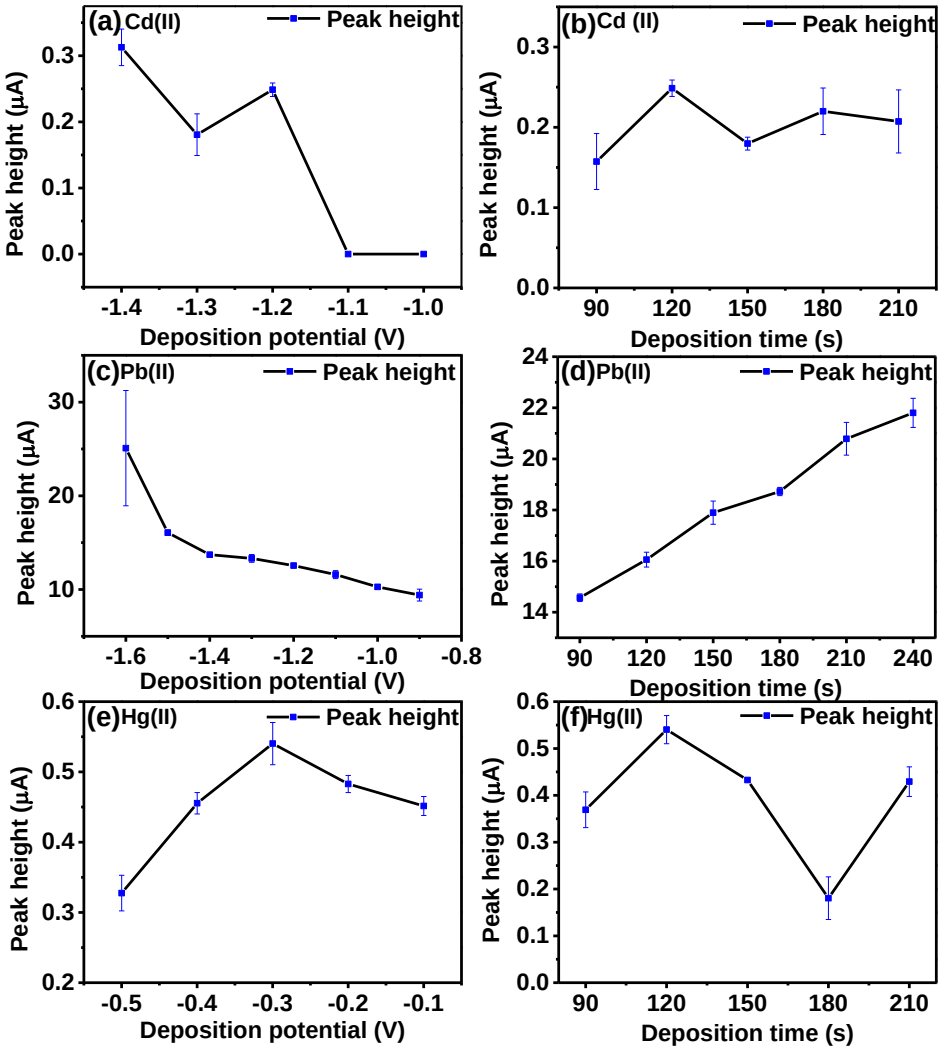

Figure 49. Optimization of deposition potential and deposition time of Cd (a and b), Pb

(c and d), and Hg (e and f).

Figure 50 to Figure 53 illustrate the voltammetric responses and calibration curves for As(III), As(total), Cr(III), Cr(VI), Cd(II), Pb(II), Pd(II), and Hg(II). The R^2 values of the linear fit for the calibration equations of most analytes exceeded 0.99, demonstrating excellent linearity. Although the shape of voltammograms for Pd(II) might appear irregular, the peaks were distinguishable and measurable. Furthermore, the calibration curve demonstrated acceptable linearity with an R^2 value of 0.9736, supporting the reliability of the method for Pd(II) determination.

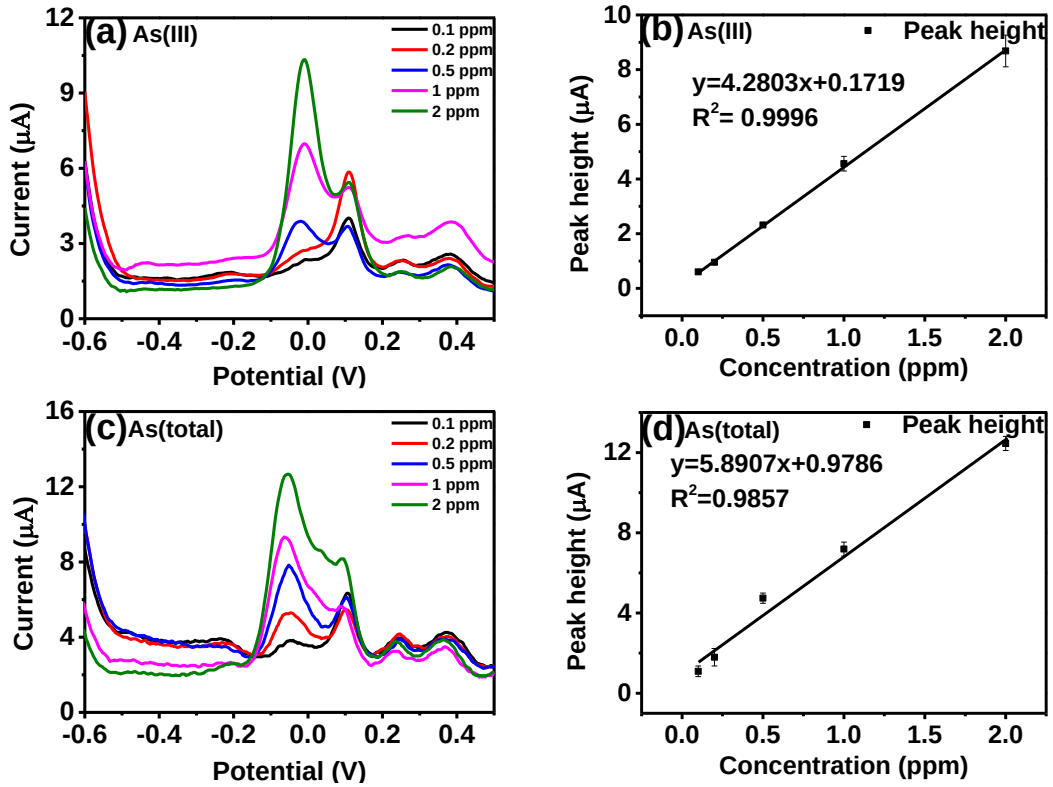

Figure 50. Voltammetry responses (a, c) and linearities (b, d) of As(III) and As(total), respectively.

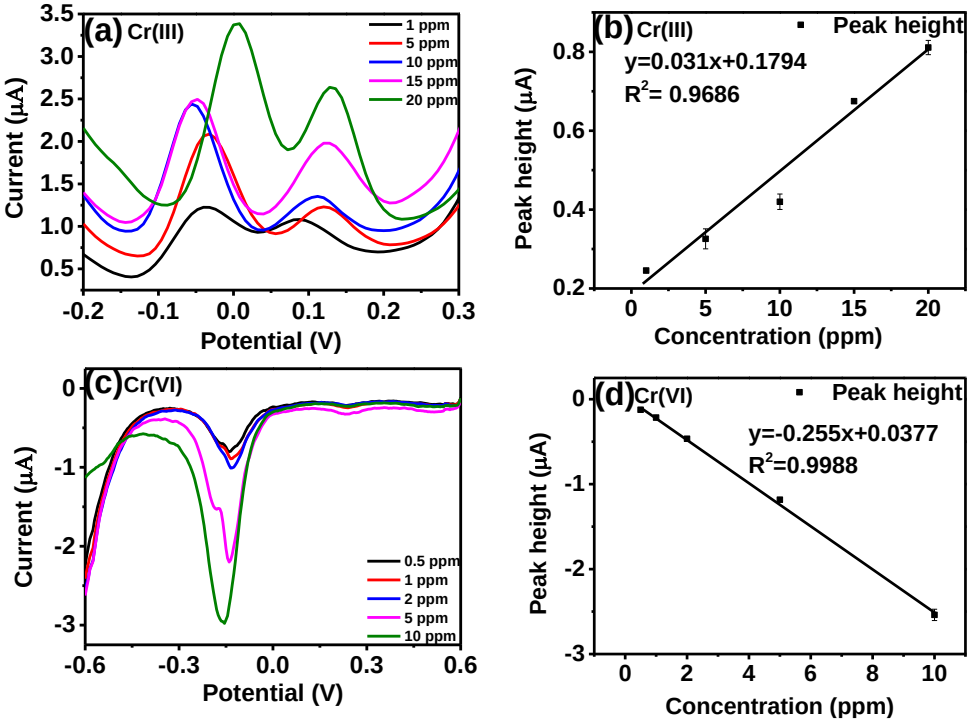

Figure 51. Voltammetry responses (a, c) and linearities (b, d) of Cr(III) and Cr(VI), respectively.

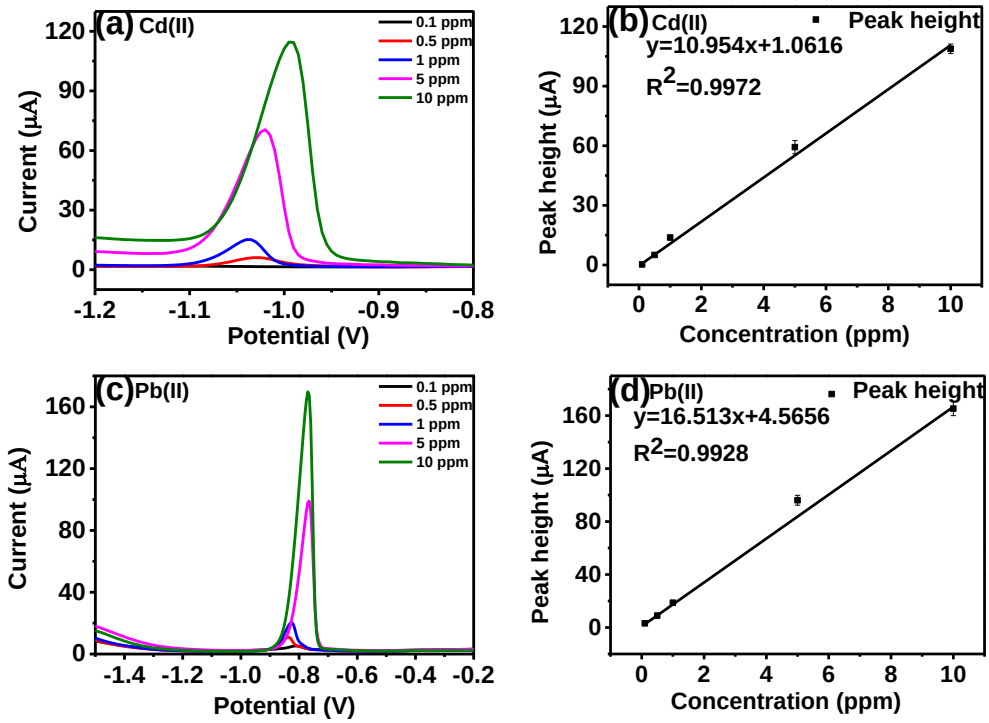

Figure 52. Voltammetry responses (a, c) and linearities (b, d) of Cd(II) and Pb(II), respectively.

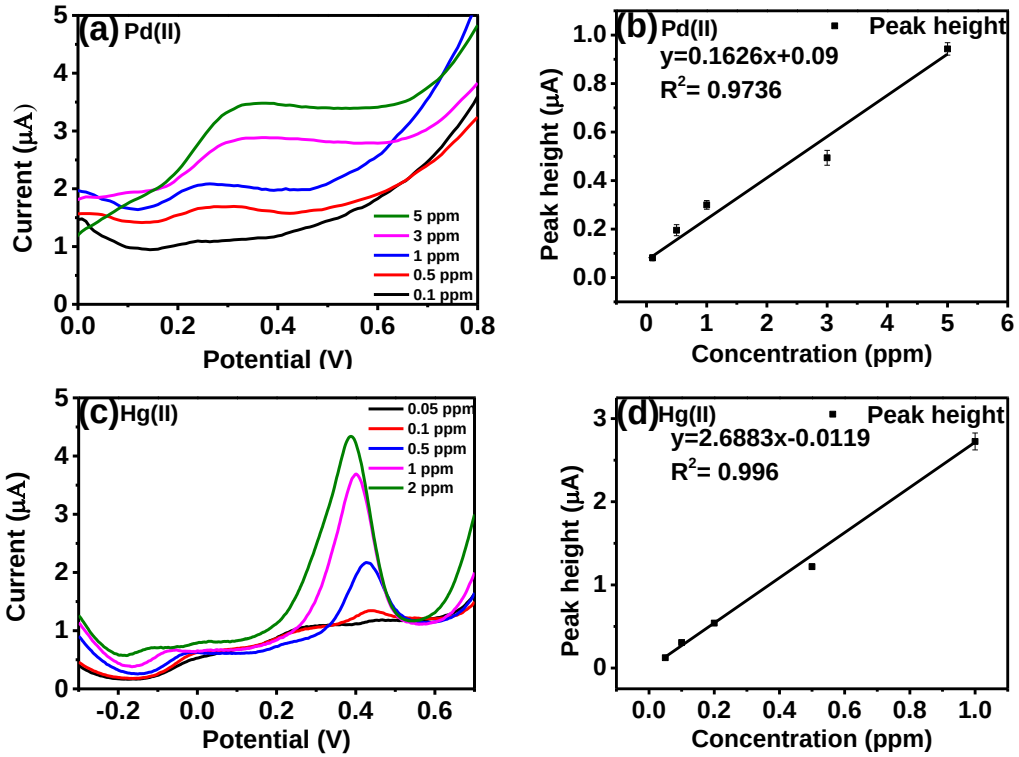

Figure 53. Voltammetry responses (a, c) and linearities (b, d) of Pd(II) and Hg(II), respectively.

The limit of detection (LOD, calculated as 3 times the standard deviation divided by the slope of the calibration curve [187]), and sensitivity (calculated as the slope of the calibration curve divided by the electrode active surface area [275]) for each analyte were shown in Table 21.

Table 21. Detection range, limit of detection and sensitivity of analytes.

Analyte	As(III)	As(total)	Cd(II)	Cr(III)	Cr(VI)	Hg(II)	Pb(II)	Pd(II)
Detection range/ppm	0.1-2	0.1-2	0.1-10	1-20	0.5-10	0.05-1	0.1-10	0.1-5
LOD/ppm	0.020	0.013	0.003	0.377	0.042	0.008	0.045	0.023
Sensitivity/μA·ppm^{-1}·cm^{-2}	36.899	50.782	94.431	0.267	2.198	23.175	142.353	1.402

For example, these working concentration ranges meet the Singapore Acceptance Criteria for Landfill set by the National Environment Agency (NEA), which stipulates maximum permissible concentrations of 5 ppm for As, Cr and Pb, 1 ppm for Cd, and 0.2 ppm for Hg [276].

6.3.3 Performance of voltammetric sensor in the leachate samples

Generally, the voltammetric sensors demonstrated strong agreement with ICP-OES/HPLC-ICP-QQQ results for all tested analytes, validating their applicability for rapid, on-site testing. Figure 54 to Figure 56 present the comparison of Cd, Pb, Pd, Hg, and the speciation results of Cr and As in both ACB leachate samples and spiked leachates of raw biochar measured by both ICP-OES/HPLC-ICP-QQQ and voltammetric sensors. Overall, the values obtained from the voltammetric sensors closely align with those from the standard methods.

As shown in Figure 54, Cd and Pb did not readily react with the leachate to form precipitates, nor were they significantly adsorbed by the biochar in a short timeframe. However, neither element was fully leached out during TCLP and UAL, suggesting that they may have been strongly adsorbed and immobilized on the biochar during the preparation of the ACB samples. TCLP simulates the leaching process through a landfill, which cannot leach out all the heavy metal and metalloid ions. When necessary, microwave acidic digestion should be employed to dissolve all the heavy metals and metalloids [277]. Pd and Hg showed reductions in concentration due to both precipitation in the leachate and adsorption by the biochar. Notably, nearly 90% of Hg was adsorbed by the biochar within 30 minutes, demonstrating the strong affinity of biochar for mercury removal under these conditions.

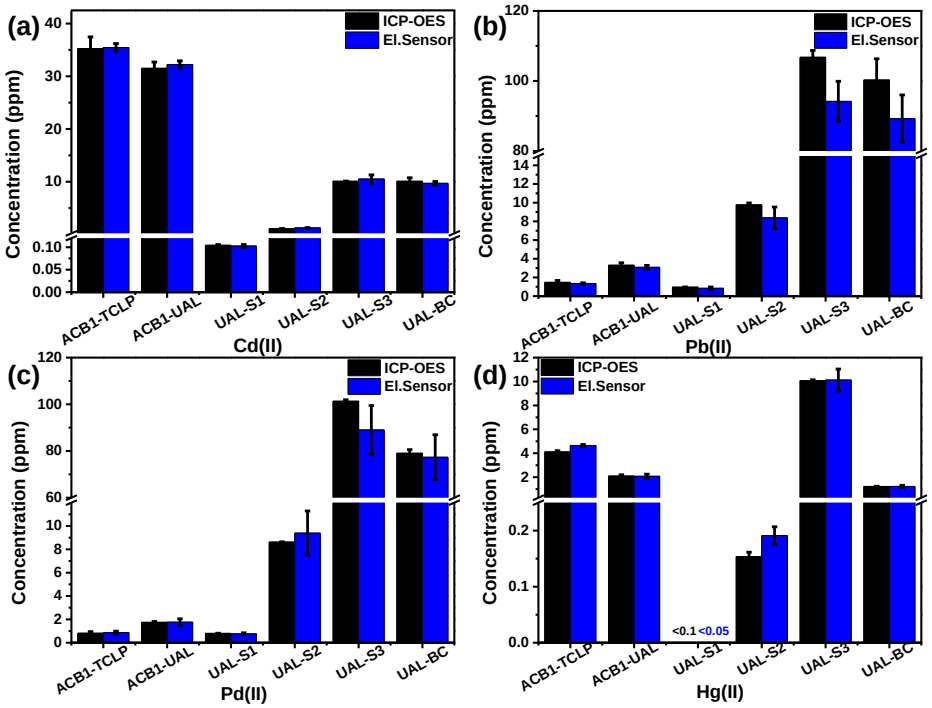

Figure 54. Comparison of (a) Cd(II), (b) Pb(II), (c) Pd(II) and (d) Hg(II) concentrations in leachate samples measured by ICP-OES and voltammetric sensors.

The concentrations of Cr in ACB2-TCLP/UAL were below 0.1 ppm, indicating limited leaching under the experimental conditions, and therefore, they are not included in Figure 55. Although most Cr(III) and Cr(VI) remained in the solution after prolonged exposure to leachate and short-term adsorption experiments, they were not detected in the leachate samples of ACB. This discrepancy could be attributed to the longer equilibrium time required for biochar to adsorb Cr and the varying biochar-to-Cr ratio [278]. However, Cr concentrations remained high in Cr spiked leachates (UAL-Cr-BC in Figure 55) after short-term biochar adsorption experiments, suggesting that a longer equilibrium time might enhance Cr adsorption. This observation highlights the potential for future optimization of biochar adsorption conditions to improve Cr retention.

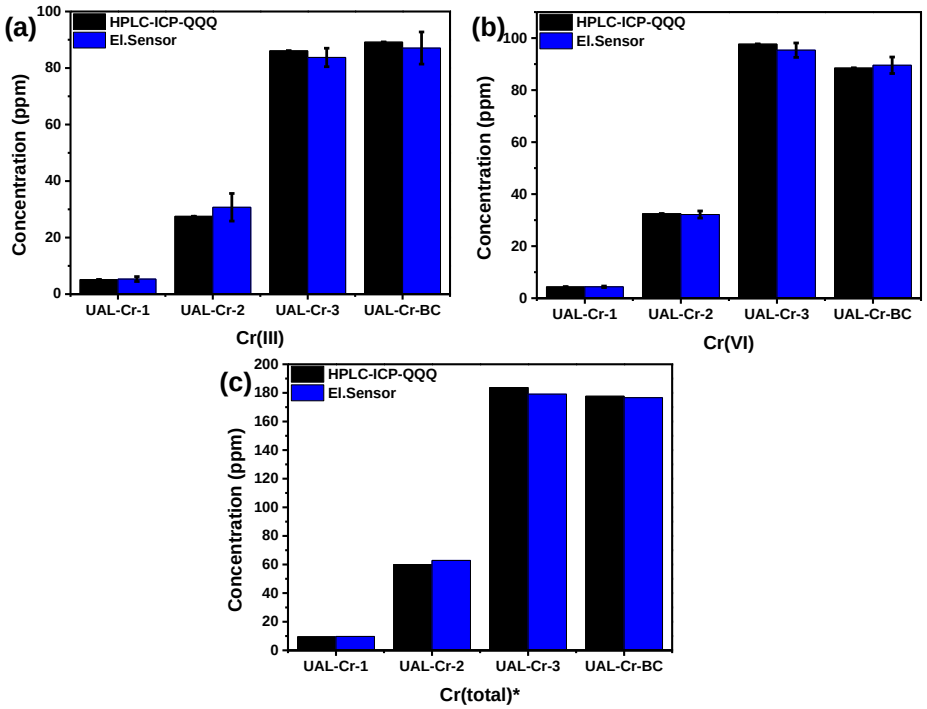

Figure 55. Comparison of Cr concentration and speciation results in leachate samples measured by HPLC-ICP-QQQ and voltammetric sensors. *Calculated by summing the average values of the individual HPLC-ICP-QQQ and results, without available SD data.

As shown in **Error! Reference source not found.**, the total As content measured by ICP-QQQ was in line with ICP-OES result in Table 18. Similar to Cr, the concentrations of As(III) and As(V) were close to each other and did not reduce much when spiked in leachates for ten days and contacted with biochar for a short time. However, As(III) concentrations in ACB3 leachates were significantly lower than As(V) concentrations, indicating that the biochar exhibited a higher adsorption capacity for the more toxic As(III), consistent with the findings outlined in the review of Benis *et al.* [279].

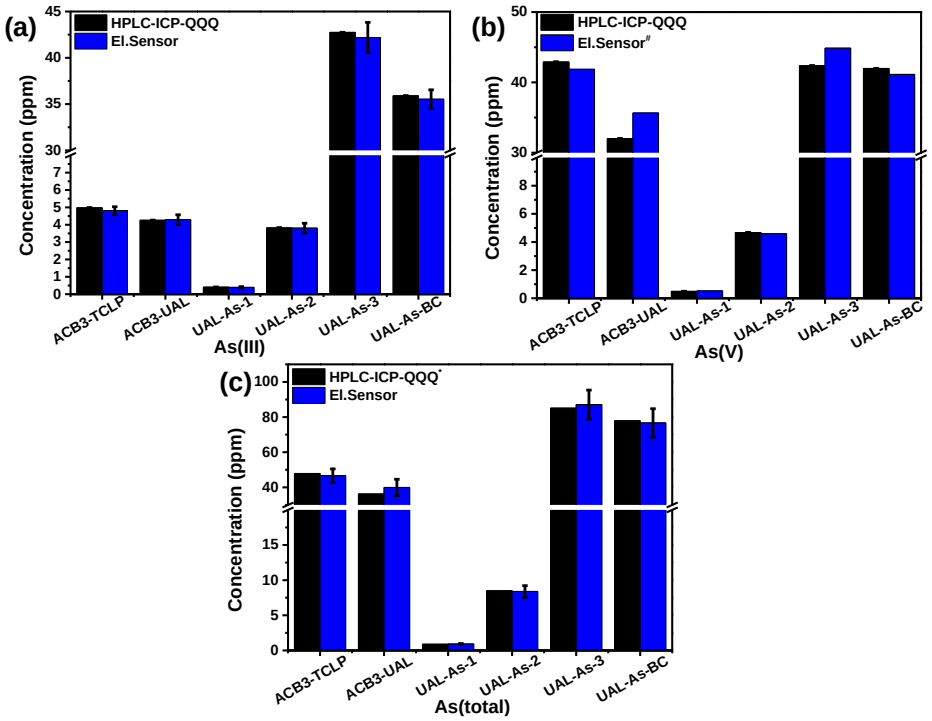

Figure 56. Comparison of As concentration and speciation results in leachate samples measured by HPLC-ICP-QQQ and voltammetric sensors. #Calculated by subtracting the As (III) concentration from the total As concentration, without available SD data. *Calculated by summing the average values of the individual HPLC-ICP-QQQ results, without available SD data.

6.4 Conclusion

This study introduced an innovative approach that combines a custom-made portable UAL device with a portable 8-channel electrochemical workstation. Using self-developed screen-printed electrode chips and our optimized protocols, this approach was successfully applied for rapid on-site determination of heavy metals and metalloids in contaminated biochar samples. Although some of the sensors were modified with precious metal such as gold, the minimal modification amount makes the cost increase very low. All the modified electrodes cost less than 10 Singapore dollar. In addition, the modifiers can be mixed into the ink for screen-print purpose, which make mass production possible. Most importantly, this approach significantly accelerated the leaching process,

reducing the time from 18 hours (as required by the traditional TCLP) to just 30 minutes, and allowed for the simultaneous detection of As(III and total), Cd(II), Cr(III and VI), Pb(II), Pd(II), and Hg(II) by voltammetric sensors within 15 minutes. The LOD of each analyte (0.013 ppm for As(total), 0.02 ppm for As (III), 0.377 ppm for Cr(III), 0.042 ppm for Cr(VI), 0.003 ppm for Cd(II), 0.045 ppm for Pb(II), 0.023 ppm for Pd(II), and 0.008 for Hg(II)) met the local landfill acceptance criteria, confirming the practicality and suitability for real-world applications.

The proposed approach was validated against standard techniques, including ICP-OES and HPLC-ICP-QQQ, demonstrating high reliability and effectiveness comparable to conventional methods. This study underscores the potential of the developed portable devices as a cost-effective, efficient, and scalable solution for rapid heavy metal and metalloid leaching and analysis, making them particularly valuable for safe waste management practices and environmental monitoring.

By streamlining the leaching and analysis processes, reducing reliance on bulky and expensive instruments, and minimizing the need for specialized personnel, this approach meets the critical demand for rapid on-site testing of heavy metals and metalloids in waste and waste-derived materials with low organic contents, such as those undergoing thermo-chemical treatment (e.g., incineration, pyrolysis, or gasification) before landfill disposal. These findings provide a transformative solution that supports sustainable urban development and enhances environmental protection efforts amid increasing challenges posed by rapid urbanization and industrialization.

CHAPTER 7 CONCLUSIONS AND RECOMMENDATIONS

7.1 Conclusions

This thesis presents the innovative synthesis and characterization of several nanomaterials and their applications in voltametric sensors in electrochemical targeted on-site monitoring and speciation of heavy metal ions. Key conclusions from each chapter are as follows:

Chapter 3 demonstrates the synthesis of BiONS and its application to an electrochemical sensor for detecting palladium ion (Pd^{2+}) in complex wastewater samples. BiONS with a width of 300 - 1000 nm and a thickness of 6 - 10 nm were synthesized through a co-precipitation-like method without adding halogens or doping metalloids. Characterizations confirmed that the BiONS predominantly consisted of β-Bi_2O_3 with minor amounts of α-Bi_2O_3, forming nanosheets with a thickness of approximately 6-10 nm. Critical parameters, including buffer composition, pH, deposition potential, and time were optimized, leading to the establishment of a reliable detection protocol. The BiONS-SPCEs exhibited enhanced sensitivity for Pd^{2+} detection with a linear detection range of 40-400 ppb and a LOD of 1.4 ppb. This sensitivity is notably higher than many conventional sensors, underscoring the effectiveness of BiONS in electrocatalytic enhancement. Interference studies confirmed the robustness of BiONS-SPCEs in the presence of various metal ions commonly found in wastewater, even though some interference was noted with Cu^{2+} and As^{3+}. This necessitates further optimization of pretreatment processes for samples with high concentrations of these interfering ions. The practical application of BiONS-SPCEs was validated through the detection of Pd^{2+} in real pharmaceutical wastewater samples. The results from BiONS-SPCEs were closely aligned with those obtained from ICP-OES, demonstrating the sensor's capability for rapid, accurate, and cost-effective Pd^{2+} monitoring. This correlation also highlights the potential of BiONS-SPCEs for in-situ monitoring and control of palladium recovery processes, enabling more

efficient management of reagent dosages and treatment efficacy.

In Chapter 4, the development and evaluation of the novel Ag-Au-SPCE and Au-SPCE electrodes offer significant advancements in the electrochemical detection of Cr species in various samples. The meticulous preparation process, involving electrodeposition and subsequent oxidation steps, successfully yielded electrodes with stable gold and silver nanoparticles that exhibited superior stability and enhanced electrochemical performance. Adding 1% Ag contributed to the formation of stable silver-gold oxide species, which was confirmed by characterization instruments, including FESEM, TEM, and XPS. Ag-Au-SPCE-a and Au-SPCE electrodes demonstrated high sensitivity for detecting Cr(III) and Cr(VI), respectively. Ag-Au-SPCE-a, in particular, showed approximately double the signal response for Cr(III) compared to Au-SPCE-a, highlighting the beneficial impact of silver on the electrode's performance. The optimized detection conditions provided wide linear ranges and low LOD, making these sensors highly competitive with existing methods. Specifically, the linear ranges and LODs for Cr(III) and Cr(VI) were 50 to 1000 ppb and 50 to 5000 ppb, respectively, and 0.1 ppb for both. Meanwhile, the developed sensors exhibited robust anti-interference performance against common metal ions, although certain ions such as Cu^{2+}, Zn^{2+}, and Pb^{2+} posed challenges by co-precipitating or reacting with chromium species. The electrodes were then effectively utilized to detect and quantify Cr(III) and Cr(VI) in various spiked samples, including artificial saliva, artificial sweat, and tap water, with high accuracy and recoveries ranging from 90.5% to 112.1%. In the analysis of chromium-containing wastewater and its treatment process, the sensors' performance was consistent with traditional methods like ICP and HPLC-ICP-MS, validating their practical applicability in real-world scenarios.

A series of gold-manganese nanoparticles (AuMnNPs) with varying compositions were synthesized and systematically evaluated their potential as

modifiers SPCEs in the electrochemical detection and speciation of arsenic in Chapter 5. The synthesis process involved the precise control of Au and Mn precursors, followed by pH adjustment and overnight stirring. The resulting nanoparticles were characterized using XRD, XPS, SEM, and TEM, revealing significant differences in structure and morphology depending on the Au-to-Mn ratio. The combination of Au and Mn promoted the formation of crystalline gold, while Mn remained predominantly amorphous, indicating a synergistic effect in the composite materials. Mn species were observed to coat the surface of Au particles, influencing both their size and structural properties. The AuMnNPs-10 composite was identified as the most effective modifier for SPCEs, providing the optimal balance of conductive and catalytic properties for arsenic detection. Parameters, such as pH, deposition potential, and deposition time, were systematically optimized. It was found that a pH of 2, a deposition potential of -1.1 V, and a deposition time of 180 s provided the best conditions for total arsenic detection. For As(III) specific detection, a deposition potential of -0.6 V was optimal. The modified electrodes exhibited distinct and well-resolved peaks for As(III) and As(V), allowing for effective speciation. The developed method showed a LOD of 0.048 ppm for total arsenic and 0.07 ppm for As(III), with a linear detection range of 0.2 to 2 ppm. The modified electrodes demonstrated high selectivity against common interfering ions and surfactants. Interferences from metals like Cd, Cu, Ni, Pb, and Hg were successfully mitigated using SDDC treatment, reducing the interference signal to below 10%. The impact of surfactants was also assessed, with cationic surfactants such as PEI showing significant signal reduction due to adsorption on the electrode surface, while anionic surfactants like SDS had minimal effect. The developed sensor was applied to monitor arsenic in wastewater treated with $Fe(OH)_3$, demonstrating its practical utility in environmental analysis. The method provided accurate and reliable quantification of both As(III) and As(V), which was further confirmed by HPLC-ICP-QQQ.

Chapter 6 is mainly an extension of Chapters 3, 4, and 5. A UAT was designed to enhance the leaching process of heavy metals from biochar under ultrasonic and mechanical agitation conditions. This device facilitated a more efficient and consistent leaching process than traditional methods. UAL parameters, including tumbling speed and sonication time, were optimized through systematic experimentation. Comparative analysis between UAL and TCLP methods demonstrated that UAL could be an effective alternative, with UAL6 (tumbling speed at 45 rpm and 30 min of sonication time) showing minimal statistical difference in the leaching of key elements, thus validating its efficacy. The commercial SPCE (DRP-C110) was utilized directly for the detection of Cd(II) and Pb(II), while another commercial screen-printed gold electrode (DRP-220BT) was dedicated to Hg(II) detection. The above mentioned electrodes, BiONS-SPCE, Ag-Au-SPCE, Ag-Au-SPCE-a, and AuMnNPs-10-SPCE, were applied for the determination/ speciation of Pd(II), Cr(III), Cr(VI), As(III and total), respectively. The electrochemical methods allowed for the simultaneous detection of multiple ions using an 8-channel potentiostat, providing a robust and efficient approach for monitoring heavy metal contamination in biochar leachates. The advancements made in this thesis not only enhance the understanding of nanomaterial applications in environmental sensing but also pave the way for the development of more effective and sustainable waste management practices amid escalating urbanization and environmental challenges.

7.2 Recommendations for future research

Based on the current results, it is clear that nanomaterial engineered electrochemical sensors appear to be a plausible alternative approach for the detection and speciation of heavy metal ions. Nevertheless, there are still some aspects of these works that can be improved in the future:

- The preparation method of Ag-Au-SPCE and Ag-Au-SPCE-a is relatively complicated as it takes 3 individual steps, the silver reference electrode needs to be covered in the beginning and needs to be removed after step

1, meanwhile, the electrode needs to be dry in between the steps. Thus, ex situ synthesis of gold and gold oxide species is preferred.

- The direct electrochemical speciation of As by AuMnNPs-10-SPCE was achieved at the expense of higher LODs. Refining the nanostructure or exploring alternative materials could lower the LODs for As detection.
- Even though the quantity of modifiers like gold and silver required for each sensor is minimal, exploring cost-effective alternatives could make the technology more accessible.
- Strategies to overcome interference from non-target analytes and complex sample matrices should be developed to enhance the applicability of the sensors across various environmental contexts.
- The range of synthesized nanomaterials and their applications should be broadened to include more diverse environmental matrices and contaminants.
- UAL coupled with voltammetric sensors can be applied to the on-site leaching and detection of other solid wastes such as incineration bottom and fly ashes (IBA and IFA), sludge, and municipal solid waste (MSW).

REFERENCES

[1] S.S. Raychaudhuri, P. Pramanick, P. Talukder, A. Basak, Chapter 6 - Polyamines, metallothioneins, and phytochelatins—Natural defense of plants to mitigate heavy metals, in: R. Atta ur (Ed.) Stud. Nat. Prod. Chem., Elsevier2021, pp. 227-261.

[2] S.F. Ahmed, P.S. Kumar, M.R. Rozbu, A.T. Chowdhury, S. Nuzhat, N. Rafa, T.M.I. Mahlia, H.C. Ong, M. Mofijur, Heavy metal toxicity, sources, and remediation techniques for contaminated water and soil, Environmental Technology & Innovation, 25 (2022) 102114.

[3] L.A. Malik, A. Bashir, A. Qureashi, A.H. Pandith, Detection and removal of heavy metal ions: a review, Environ. Chem. Lett., 17 (2019) 1495-1521.

[4] W. Wu, J. Wang, Y. Yu, H. Jiang, N. Liu, J. Bi, M. Liu, Optimizing critical source control of five priority-regulatory trace elements from industrial wastewater in China: Implications for health management, Environ. Pollut., 235 (2018) 761-770.

[5] D. Jayamurali, K.M. Varier, W. Liu, J. Raman, Y. Ben-David, X. Shen, B. Gajendran, An Overview of Heavy Metal Toxicity, in: S. Rajendran, M. Naushad, D. Durgalakshmi, E. Lichtfouse (Eds.) Metal, Metal Oxides and Metal Sulphides for Biomedical Applications, Springer International Publishing, Cham, 2021, pp. 323-342.

[6] B. Nowicka, Heavy metal–induced stress in eukaryotic algae—mechanisms of heavy metal toxicity and tolerance with particular emphasis on oxidative stress in exposed cells and the role of antioxidant response, Environmental Science and Pollution Research, 29 (2022) 16860-16911.

[7] E. Byeon, H.-M. Kang, C. Yoon, J.-S. Lee, Toxicity mechanisms of arsenic compounds in aquatic organisms, Aquat. Toxicol., 237 (2021) 105901.

[8] V.K. Sharma, M. Sohn, Aquatic arsenic: Toxicity, speciation, transformations, and remediation, Environ. Int., 35 (2009) 743-759.

[9] Y. Wang, S. Wang, P. Xu, C. Liu, M. Liu, Y. Wang, C. Wang, C. Zhang, Y. Ge, Review of arsenic speciation, toxicity and metabolism in microalgae,

Reviews in Environmental Science and Bio/Technology, 14 (2015) 427-451.
[10] A. Ashraf, I. Bibi, N.K. Niazi, Y.S. Ok, G. Murtaza, M. Shahid, A. Kunhikrishnan, D. Li, T. Mahmood, Chromium (VI) sorption efficiency of acid-activated banana peel over organo-montmorillonite in aqueous solutions, International journal of phytoremediation, 19 (2017) 605-613.
[11] D. Mohan, C.U. Pittman Jr, Activated carbons and low cost adsorbents for remediation of tri-and hexavalent chromium from water, J. Hazard. Mater., 137 (2006) 762-811.
[12] J.J. Coetzee, N. Bansal, E.M.N. Chirwa, Chromium in Environment, Its Toxic Effect from Chromite-Mining and Ferrochrome Industries, and Its Possible Bioremediation, Exposure and Health, 12 (2020) 51-62.
[13] M. Shahid, S. Shamshad, M. Rafiq, S. Khalid, I. Bibi, N.K. Niazi, C. Dumat, M.I. Rashid, Chromium speciation, bioavailability, uptake, toxicity and detoxification in soil-plant system: A review, Chemosphere, 178 (2017) 513-533.
[14] M. Kumar, M. Nandi, K. Pakshirajan, Recent advances in heavy metal recovery from wastewater by biogenic sulfide precipitation, Journal of Environmental Management, 278 (2021) 111555.
[15] A. Taghvaie Nakhjiri, H. Sanaeepur, A. Ebadi Amooghin, M.M.A. Shirazi, Recovery of precious metals from industrial wastewater towards resource recovery and environmental sustainability: A critical review, Desalination, 527 (2022) 115510.
[16] O. Moradi, A review on nanomaterial-based electrochemical sensors for determination of vanillin in food samples, Food and Chemical Toxicology, 168 (2022) 113391.
[17] M. Fojta, A. Daňhel, L. Havran, V. Vyskočil, Recent progress in electrochemical sensors and assays for DNA damage and repair, TrAC, Trends Anal. Chem., 79 (2016) 160-167.
[18] A. Sinha, Dhanjai, R. Jain, H. Zhao, P. Karolia, N. Jadon, Voltammetric sensing based on the use of advanced carbonaceous nanomaterials: a review,

Microchim. Acta, 185 (2018) 89.
[19] C. Zhu, G. Yang, H. Li, D. Du, Y. Lin, Electrochemical sensors and biosensors based on nanomaterials and nanostructures, Anal. Chem., 87 (2015) 230-249.
[20] K.Y. Goud, S.K. Kailasa, V. Kumar, Y.F. Tsang, K.V. Gobi, K.-H. Kim, Progress on nanostructured electrochemical sensors and their recognition elements for detection of mycotoxins: A review, Biosens. Bioelectron., 121 (2018) 205-222.
[21] D. Ilager, H. Seo, N.P. Shetti, S.S. Kalanur, T.M. Aminabhavi, Electrocatalytic detection of herbicide, amitrole at WO3· 0.33 H2O modified carbon paste electrode for environmental applications, Sci. Total Environ., 743 (2020) 140691.
[22] H. Du, Y. Xie, J. Wang, Nanomaterial-sensors for herbicides detection using electrochemical techniques and prospect applications, TrAC, Trends Anal. Chem., 135 (2021) 116178.
[23] Z. Liang, T. Qiu, S. Gao, R. Zhong, R. Zou, Multi-Scale Design of Metal–Organic Framework-Derived Materials for Energy Electrocatalysis, Advanced Energy Materials, 12 (2022) 2003410.
[24] M. Hao, M. Qiu, H. Yang, B. Hu, X. Wang, Recent advances on preparation and environmental applications of MOF-derived carbons in catalysis, Sci. Total Environ., 760 (2021) 143333.
[25] J.M. Gonçalves, P.R. Martins, D.P. Rocha, T.A. Matias, M.S.S. Julião, R.A.A. Munoz, L. Angnes, Recent trends and perspectives in electrochemical sensors based on MOF-derived materials, Journal of Materials Chemistry C, 9 (2021) 8718-8745.
[26] L. Lu, Z. Zhu, X. Hu, Hybrid nanocomposites modified on sensors and biosensors for the analysis of food functionality and safety, Trends Food Sci. Technol., 90 (2019) 100-110.
[27] N. Baig, M. Sajid, T.A. Saleh, Recent trends in nanomaterial-modified electrodes for electroanalytical applications, TrAC, Trends Anal. Chem., 111

(2019) 47-61.
[28] L.A. Kolahalam, I.V. Kasi Viswanath, B.S. Diwakar, B. Govindh, V. Reddy, Y.L.N. Murthy, Review on nanomaterials: Synthesis and applications, Materials Today: Proceedings, 18 (2019) 2182-2190.
[29] R.R. Poolakkandy, M.M. Menamparambath, Soft-template-assisted synthesis: a promising approach for the fabrication of transition metal oxides, Nanoscale Advances, 2 (2020) 5015-5045.
[30] M. Tulinski, M. Jurczyk, Nanomaterials Synthesis Methods, Metrology and Standardization of Nanotechnology2017, pp. 75-98.
[31] T.P. Yadav, R.M. Yadav, D.P. Singh, Mechanical milling: a top down approach for the synthesis of nanomaterials and nanocomposites, Nanoscience and Nanotechnology, 2 (2012) 22-48.
[32] H.D. Kurland, J. Grabow, G. Staupendahl, W. Andrä, S. Dutz, M.E. Bellemann, Magnetic iron oxide nanopowders produced by CO2 laser evaporation, Journal of Magnetism and Magnetic Materials, 311 (2007) 73-77.
[33] C.P. Poole, F.J. Owens, Introduction to nanotechnology, (2003).
[34] L. Bu, J. Xie, K. Chen, J. Huang, Z.P. Aguilar, A. Wang, K.W. Sun, M.S. Chua, S. So, Z. Cheng, Assessment and comparison of magnetic nanoparticles as MRI contrast agents in a rodent model of human hepatocellular carcinoma, Contrast Media Mol. Imaging, 7 (2012) 363-372.
[35] P. Ayyub, R. Chandra, P. Taneja, A.K. Sharma, R. Pinto, Synthesis of nanocrystalline material by sputtering and laser ablation at low temperatures, Appl. Phys. A, 73 (2001) 67-73.
[36] R. Ostermann, J. Cravillon, C. Weidmann, M. Wiebcke, B.M. Smarsly, Metal–organic framework nanofibers viaelectrospinning, Chem. Commun. (Cambridge, U. K.), 47 (2011) 442-444.
[37] K.M. Krishnan, Fundamentals and applications of magnetic materials, Oxford University Press2016.
[38] A. Ahmad, P. Mukherjee, S. Senapati, D. Mandal, M.I. Khan, R. Kumar, M. Sastry, Extracellular biosynthesis of silver nanoparticles using the fungus

Fusarium oxysporum, Colloids Surf. B. Biointerfaces, 28 (2003) 313-318.
[39] Y. Ma, X. Yang, Y. Wei, Q. Yuan, Applications of DNA Nanotechnology in Synthesis and Assembly of Inorganic Nanomaterials, Chinese Journal of Chemistry, 34 (2016) 291-298.
[40] Y. Xing, Y.-Y. Jin, J.-C. Si, M.-L. Peng, X.-F. Wang, C. Chen, Y.-L. Cui, Controllable synthesis and characterization of Fe3O4/Au composite nanoparticles, Journal of Magnetism and Magnetic Materials, 380 (2015) 150-156.
[41] M. Parashar, V.K. Shukla, R. Singh, Metal oxides nanoparticles via sol–gel method: a review on synthesis, characterization and applications, J. Mater. Sci.: Mater. Electron., 31 (2020) 3729-3749.
[42] N. Nandihalli, D.H. Gregory, T. Mori, Energy-Saving Pathways for Thermoelectric Nanomaterial Synthesis: Hydrothermal/Solvothermal, Microwave-Assisted, Solution-Based, and Powder Processing, Advanced Science, 9 (2022) 2106052.
[43] P. Machac, S. Cichon, L. Lapcak, L. Fekete, Graphene prepared by chemical vapour deposition process, Graphene Technology, 5 (2020) 9-17.
[44] O. Lebedeva, D. Kultin, L. Kustov, Electrochemical Synthesis of Unique Nanomaterials in Ionic Liquids, Nanomaterials, 11 (2021) 3270.
[45] C. Dincer, R. Bruch, E. Costa-Rama, M.T. Fernández-Abedul, A. Merkoçi, A. Manz, G.A. Urban, F. Güder, Disposable Sensors in Diagnostics, Food, and Environmental Monitoring, Adv. Mater., 31 (2019) 1806739.
[46] A. Adhikari, D.R. Acosta-Najarro, A.J. Fragoso-Medina, O. Reyes-Vallejo, F.J. Cano, M.d.l.L. Olvera Amador, V. Subramaniam, Review on the developments in copper indium gallium diselenide (CIGSe)-based thin film photovoltaic devices, J. Mater. Sci.: Mater. Electron., 35 (2024) 1016.
[47] C.B. Braungardt, Evaluation of Analytical Instrumentation. Part XXVI: Instrumentation for Voltammetry, Anal. Methods, 7 (2015) 1249-1260.
[48] J. Liu, Y. Xu, S. Liu, S. Yu, Z. Yu, S.S. Low, Application and Progress of Chemometrics in Voltammetric Biosensing, Biosensors, 12 (2022) 494.

[49] G. Herzog, V. Beni, Stripping voltammetry at micro-interface arrays: A review, Anal. Chim. Acta, 769 (2013) 10-21.
[50] A. Bratov, N. Abramova, A. Ipatov, Recent trends in potentiometric sensor arrays—A review, Anal. Chim. Acta, 678 (2010) 149-159.
[51] O. Özbek, C. Berkel, Recent advances in potentiometric analysis: Paper–based devices, Sensors International, 3 (2022) 100189.
[52] H. Karimi Maleh, Y. Orooji, F. Karimi, M. Alizadeh, M. Baghayeri, J. Rouhi, S. Tajik, H. Beitollahi, S. Agarwal, V.K. Gupta, S. Rajendran, A. Ayati, L. Fu, A.L. Sanati, B. Tanhaei, F. Sen, M. shabani-nooshabadi, P.N. Asrami, A. Al-Othman, A critical review on the use of potentiometric based biosensors for biomarkers detection, Biosens. Bioelectron., 184 (2021) 113252.
[53] W. Jin, H. Du, S. Zheng, Y. Zhang, Electrochemical processes for the environmental remediation of toxic Cr(VI): A review, Electrochim. Acta, 191 (2016) 1044-1055.
[54] M.G. Arellano-Sánchez, C. Devouge-Boyer, M. Hubert-Roux, C. Afonso, M. Mignot, Chromium Determination in Leather and Other Matrices: A Review, Crit. Rev. Anal. Chem., 52 (2022) 1537-1556.
[55] P. Dionisios, P. George, P. Dimitrios, A. Pavlos, Arsenic Geochemistry in Groundwater System, in: P. Dionisios (Ed.) Geochemistry, IntechOpen, Rijeka, 2012, pp. Ch. 2.
[56] C. Kalinke, P.R. Oliveira, G.A. Oliveira, A.S. Mangrich, L.H. Marcolino-Junior, M.F. Bergamini, Activated biochar: Preparation, characterization and electroanalytical application in an alternative strategy of nickel determination, Anal. Chim. Acta, 983 (2017) 103-111.
[57] A. Hojjati-Najafabadi, M. Mansoorianfar, T. Liang, K. Shahin, H. Karimi-Maleh, A review on magnetic sensors for monitoring of hazardous pollutants in water resources, Sci. Total Environ., 824 (2022) 153844.
[58] A. Technologies, Atomic Absorption Spectroscopy Overview, 2025.
[59] A. Technologies, ICP-OES Overview, 2025.
[60] A. Technologies, ICP-MS Overview, 2025.

[61] X. Wu, S.J. Cobbina, G. Mao, H. Xu, Z. Zhang, L. Yang, A review of toxicity and mechanisms of individual and mixtures of heavy metals in the environment, Environmental Science and Pollution Research, 23 (2016) 8244-8259.
[62] S. Fendorf, B.W. Wielinga, C.M. Hansel, Chromium Transformations in Natural Environments: The Role of Biological and Abiological Processes in Chromium(VI) Reduction, Int Geol Rev, 42 (2000) 691-701.
[63] B. Markiewicz, I. Komorowicz, A. Sajnóg, M. Belter, D. Barałkiewicz, Chromium and its speciation in water samples by HPLC/ICP-MS – technique establishing metrological traceability: A review since 2000, Talanta, 132 (2015) 814-828.
[64] P. Biswas, A.K. Karn, P. Balasubramanian, P.G. Kale, Biosensor for detection of dissolved chromium in potable water: A review, Biosens. Bioelectron., 94 (2017) 589-604.
[65] K. Zhao, L. Ge, T.I. Wong, X. Zhou, G. Lisak, Gold-silver nanoparticles modified electrochemical sensor array for simultaneous determination of chromium (III) and chromium (VI) in wastewater samples, Chemosphere, 281 (2021) 130880.
[66] J. Vuković, M.A. Avidad, L.F. Capitán-Vallvey, Characterization of disposable optical sensors for heavy metal determination, Talanta, 94 (2012) 123-132.
[67] M. Jin, H. Yuan, B. Liu, J. Peng, L. Xu, D. Yang, Review of the distribution and detection methods of heavy metals in the environment, Anal. Methods, 12 (2020) 5747-5766.
[68] G.M. Escandar, A.C. Olivieri, A Critical Review on the Development of Optical Sensors for the Determination of Heavy Metals in Water Samples. The Case of Mercury(II) Ion, ACS Omega, 7 (2022) 39574-39585.
[69] B. Bansod, T. Kumar, R. Thakur, S. Rana, I. Singh, A review on various electrochemical techniques for heavy metal ions detection with different sensing platforms, Biosens. Bioelectron., 94 (2017) 443-455.

[70] E.C. Okpara, O.E. Fayemi, O.B. Wojuola, D.C. Onwudiwe, E.E. Ebenso, Electrochemical detection of selected heavy metals in water: a case study of African experiences, Rsc Adv, 12 (2022) 26319-26361.
[71] S.-H. Chen, Y.-X. Li, P.-H. Li, X.-Y. Xiao, M. Jiang, S.-S. Li, W.-Y. Zhou, M. Yang, X.-J. Huang, W.-Q. Liu, Electrochemical spectral methods for trace detection of heavy metals: A review, TrAC, Trends Anal. Chem., 106 (2018) 139-150.
[72] L. Zhang, Q. Song, Y. Liu, Z. Xu, Novel approach for recovery of palladium in spent catalyst from automobile by a capture technology of eutectic copper, Journal of Cleaner Production, 239 (2019) 118093.
[73] J. Recho, R.J.G. Black, C. North, J.E. Ward, R.D. Wilkes, Statistical DoE Approach to the Removal of Palladium from Active Pharmaceutical Ingredients (APIs) by Functionalized Silica Adsorbents, Org. Process Res. Dev., 18 (2014) 626-635.
[74] C. Torborg, M. Beller, Recent Applications of Palladium-Catalyzed Coupling Reactions in the Pharmaceutical, Agrochemical, and Fine Chemical Industries, Adv. Synth. Catal., 351 (2009) 3027-3043.
[75] H.U. Blaser, A. Indolese, A. Schnyder, H. Steiner, M. Studer, Supported palladium catalysts for fine chemicals synthesis, J. Mol. Catal. A: Chem., 173 (2001) 3-18.
[76] World Health Organization, Environmental Health Criteria 226, Palladium, World Health Organization, International Programme on Chemical Safety, Geneva, 2002.
[77] F. Larese Filon, M. Crosera, M. Mauro, E. Baracchini, M. Bovenzi, T. Montini, P. Fornasiero, G. Adami, Palladium nanoparticles exposure: Evaluation of permeation through damaged and intact human skin, Environ. Pollut., 214 (2016) 497-503.
[78] J. Kielhorn, C. Melber, D. Keller, I. Mangelsdorf, Palladium – A review of exposure and effects to human health, International Journal of Hygiene and Environmental Health, 205 (2002) 417-432.

[79] S. Sarioglan, Recovery of palladium from spent activated carbon-supported palladium catalysts, Platin. Met. Rev, 57 (2013) 289-296.
[80] M. Barakat, M. Mahmoud, Y. Mahrous, Recovery and separation of palladium from spent catalyst, Applied Catalysis A: General, 301 (2006) 182-186.
[81] N.J. Creamer, V.S. Baxter-Plant, J. Henderson, M. Potter, L.E. Macaskie, Palladium and gold removal and recovery from precious metal solutions and electronic scrap leachates by Desulfovibrio desulfuricans, Biotechnology letters, 28 (2006) 1475-1484.
[82] M.A. Khan, F. Qazi, Z. Hussain, M.U. Idrees, S. Soomro, S. Soomro, Recent trends in electrochemical detection of NH3, H2S and NOx gases, Int. J. Electrochem. Sci., 12 (2017) 1711-1733.
[83] J.H. Kim, K.B. Kim, J.S. Park, N. Min, Single cytosine-based electrochemical biosensor for low-cost detection of silver ions, Sensors Actuators B: Chem., 245 (2017) 741-746.
[84] M. Georgieva, B. Pihlar, Determination of palladium by adsorptive stripping voltammetry, Fresenius' Journal of Analytical Chemistry, 357 (1997) 874-880.
[85] C. Locatelli, Voltammetric Peak Area as Instrumental Datum. A Possibility to Improve the Determination at Ultratrace Level Concentration of Platinum Group Metals (PGMs) and Lead. Application to Particulate Matter, Electroanalysis, 19 (2007) 445-452.
[86] A. Bobrowski, M. Gawlicki, P. Kapturski, V. Mirceski, F. Spasovski, J. Zarębski, The Silver Amalgam Film Electrode in Adsorptive Stripping Voltammetric Determination of Palladium(II) as Its Dimethyldioxime Complex, Electroanalysis, 21 (2009) 36-40.
[87] B. Silwana, C. van der Horst, E. Iwuoha, V. Somerset, Screen-printed carbon electrodes modified with a bismuth film for stripping voltammetric analysis of platinum group metals in environmental samples, Electrochim. Acta, 128 (2014) 119-127.

[88] G. Raber, K. Kalcher, C. Neuhold, C. Talaber, G. Kölbl, Adsorptive stripping voltammetry of palladium (II) with thioridazine in situ modified carbon paste electrodes, Electroanalysis, 7 (1995) 138-142.
[89] C. Van der Horst, B. Silwana, E. Iwuoha, V. Somerset, Stripping voltammetric determination of palladium, platinum and rhodium in freshwater and sediment samples from South African water resources, Journal of Environmental Science and Health, Part A, 47 (2012) 2084-2093.
[90] M. Velmurugan, B. Thirumalraj, S.-M. Chen, F.M. Al-Hemaid, M.A. Ali, M.S. Elshikh, Development of electrochemical sensor for the determination of palladium ions (Pd2+) using flexible screen printed un-modified carbon electrode, J. Colloid Interface Sci., 485 (2017) 123-128.
[91] M. Lamblin, L. Nassar-Hardy, J.-C. Hierso, E. Fouquet, F.-X. Felpin, Recyclable Heterogeneous Palladium Catalysts in Pure Water: Sustainable Developments in Suzuki, Heck, Sonogashira and Tsuji–Trost Reactions, Adv. Synth. Catal., 352 (2010) 33-79.
[92] H. Bai, S. Wang, P. Liu, C. Xiong, K. Zhang, Q. Cao, Electrochemical sensor based on in situ polymerized ion-imprinted membranes at graphene modified electrode for palladium determination, J. Electroanal. Chem., 771 (2016) 29-36.
[93] B. Baś, K. Węgiel, K. Jedlińska, New voltammetric sensor based on the renewable bismuth bulk annular band electrode and its application for the determination of palladium (II), Electrochim. Acta, 178 (2015) 665-672.
[94] M. Korolczuk, K. Tyszczuk, M. Grabarczyk, Adsorptive stripping voltammetry of nickel and cobalt at in situ plated lead film electrode, Electrochem. Commun., 7 (2005) 1185-1189.
[95] C.A. Grimes, E.C. Dickey, M.V. Pishko, Encyclopedia of sensors, American Scientific Publishers Stevenson Ranch2006.
[96] I. Svancara, K. Kalcher, A. Walcarius, K. Vytras, Electroanalysis with carbon paste electrodes, Crc Press2012.
[97] L. Li, F. Cai, F. Qi, D.-K. Ma, Cu nanowire bridged Bi nanosheet arrays

for efficient electrochemical CO2 reduction toward formate, Journal of Alloys and Compounds, 841 (2020) 155789.
[98] M. Jiang, Y. Ding, H. Zhang, J. Ren, J. Li, C. Wan, Y. Hong, M. Qi, B. Mei, L. Deng, A novel ultrathin single-crystalline Bi 2 O 3 nanosheet wrapped by reduced graphene oxide with improved electron transfer for Li storage, J. Solid State Electrochem., 24 (2020) 2487-2497.
[99] H. Liu, Z. Chen, L. Zhou, X. Li, K. Pei, J. Zhang, Y. Song, F. Fang, R. Che, D. Sun, Rooting bismuth oxide nanosheets into porous carbon nanoboxes as a sulfur immobilizer for lithium–sulfur batteries, J Mater Chem A, 7 (2019) 7074-7081.
[100] J. Mei, T. Liao, G.A. Ayoko, Z. Sun, Two-Dimensional Bismuth Oxide Heterostructured Nanosheets for Lithium- and Sodium-Ion Storages, ACS Appl. Mater. Interfaces, 11 (2019) 28205-28212.
[101] H. Zheng, H. Li, M. Yu, M. Zhang, Y. Tong, F. Cheng, X. Lu, Vertical bismuth oxide nanosheets with enhanced crystallinity: promising stable anodes for rechargeable alkaline batteries, J Mater Chem A, 5 (2017) 25539-25544.
[102] L. Li, D. Zhang, M. Cao, J. Deng, X. Ji, Q. Wang, Electrochemical synthesis of 2D antimony, bismuth and their compounds, Journal of Materials Chemistry C, 8 (2020) 9464-9475.
[103] J. Yang, M. Wang, S. Zhao, Y. Liu, W. Zhang, B. Wu, Q. Liu, Biotemplate preparation of Bi2O3 nanosheet for enhanced photodegradation of methylene blue, Micro & Nano Letters, 14 (2019) 705-710.
[104] N. Han, Y. Wang, H. Yang, J. Deng, J. Wu, Y. Li, Y. Li, Ultrathin bismuth nanosheets from in situ topotactic transformation for selective electrocatalytic CO 2 reduction to formate, Nat. Commun., 9 (2018) 1-8.
[105] N.T. Program, Chromium hexavalent compounds, Rep. Carcinog. Carcinog. Prof., 12 (2011) 106.
[106] S. Avudainayagam, M. Megharaj, G. Owens, R.S. Kookana, D. Chittleborough, R. Naidu, Chemistry of Chromium in Soils with Emphasis on Tannery Waste Sites, in: G.W. Ware (Ed.) Rev. Environ. Contam. Toxicol.,

Springer New York, New York, NY, 2003, pp. 53-91.
[107] S.P. Mohanty, E. Kougianos, Biosensors: a tutorial review, IEEE Potentials, 25 (2006) 35-40.
[108] I. Komorowicz, D. Barałkiewicz, Arsenic and its speciation in water samples by high performance liquid chromatography inductively coupled plasma mass spectrometry—Last decade review, Talanta, 84 (2011) 247-261.
[109] K. Zhu, C. Chen, H. Xu, Y. Gao, X. Tan, A. Alsaedi, T. Hayat, Cr(VI) Reduction and Immobilization by Core-Double-Shell Structured Magnetic Polydopamine@Zeolitic Idazolate Frameworks-8 Microspheres, Acs Sustain Chem Eng, 5 (2017) 6795-6802.
[110] S.C. Gad, Chromium, in: P. Wexler (Ed.) Encyclopedia of Toxicology (Third Edition), Academic Press, Oxford, 2014, pp. 952-954.
[111] A. Ertani, A. Mietto, M. Borin, S. Nardi, Chromium in Agricultural Soils and Crops: A Review, Water, Air, Soil Pollut., 228 (2017) 190.
[112] M.B. Arain, I. Ali, E. Yilmaz, M. Soylak, Nanomaterial's based chromium speciation in environmental samples: A review, TrAC, Trends Anal. Chem., 103 (2018) 44-55.
[113] F. Hao, P. Liu, D. Li, H. Ge, Design and simulation of a fiber-optic hydrogen sensor based on tunable diode laser spectroscopy, Advanced Sensor Systems and Applications VIII, International Society for Optics and Photonics, 2018, pp. 108211P.
[114] F. Kong, Y. Zhang, H. Wang, J. Tang, Y. Li, S. Wang, Removal of Cr(VI) from wastewater by artificial zeolite spheres loaded with nano Fe–Al bimetallic oxide in constructed wetland, Chemosphere, 257 (2020) 127224.
[115] W. Niu, J. Sun, L. Zhang, F. Cao, The enhanced removal of highly toxic Cr(VI) by the synergy of uniform fiber ball loaded with Fe(OH)3 and oxalate acid, Chemosphere, 262 (2021) 127806.
[116] L. Zhang, W. Niu, J. Sun, Q. Zhou, Efficient removal of Cr(VI) from water by the uniform fiber ball loaded with polypyrrole: Static adsorption, dynamic adsorption and mechanism studies, Chemosphere, 248 (2020) 126102.

[117] W. Wang, B. Hu, C. Wang, Z. Liang, F. Cui, Z. Zhao, C. Yang, Cr(VI) removal by micron-scale iron-carbon composite induced by ball milling: The role of activated carbon, Chem. Eng. J., 389 (2020) 122633.
[118] Z. Lv, X. Tan, C. Wang, A. Alsaedi, T. Hayat, C. Chen, Metal-organic frameworks-derived 3D yolk shell-like structure Ni@carbon as a recyclable catalyst for Cr(VI) reduction, Chem. Eng. J., 389 (2020) 123428.
[119] P. Miretzky, A.F. Cirelli, Cr(VI) and Cr(III) removal from aqueous solution by raw and modified lignocellulosic materials: A review, J. Hazard. Mater., 180 (2010) 1-19.
[120] S.K. Aggarwal, M. Kinter, R.L. Fitzgerald, D.A. Herold, W.W. Harrison, Mass Spectrometry of Trace Elements in Biological Samples, Crit. Rev. Clin. Lab. Sci., 31 (1994) 35-87.
[121] J.A.B. Kettelarij, C. Liden, E. Axen, A. Julander, Cobalt, nickel and chromium release from dental tools and alloys, Contact Dermatitis, 70 (2014) 3-10.
[122] D. Bregnbak, J.D. Johansen, D. Hamann, C.R. Hamann, C. Hamann, R. Spiewak, T. Menne, C. Zachariae, M.S. Jellesen, J.P. Thyssen, Assessment of chromium(VI) release from 848 jewellery items by use of a diphenylcarbazide spot test, Contact Dermatitis, 75 (2016) 115-U181.
[123] D. Hamann, J.P. Thyssen, C.R. Hamann, C. Hamann, T. Menne, J.D. Johansen, R. Spiewak, H. Maibach, L. Lundgren, C. Liden, Jewellery: alloy composition and release of nickel, cobalt and lead assessed with the EU synthetic sweat method, Contact Dermatitis, 73 (2015) 231-238.
[124] A.P. Kurek, M.E.R. Dotto, P.H.H. de Araújo, N. Sellin, Evaluation of the etching and chrome plating on the ABS, PVC, and PVC/ABS blends surface, J. Appl. Polym. Sci., 134 (2017).
[125] H. Barhoumi, A. Maaref, R. Mlika, C. Martelet, N. Jaffrezic-Renault, L. Ponsonnet, EIS field effect structures functionalized by p-tert-butylcalix[6]arene for Ni2+ detection, Materials Science and Engineering: C, 25 (2005) 61-66.

[126] J. Peris Vicente, J.V. Gimeno Adelantado, M.T. Doménech Carbó, R. Mateo Castro, F. Bosch Reig, Identification of lipid binders in old oil paintings by separation of 4-bromomethyl-7-methoxycoumarin derivatives of fatty acids by liquid chromatography with fluorescence detection, J. Chromatogr. A, 1076 (2005) 44-50.
[127] K.M. Diniz, C.R.T. Tarley, Speciation analysis of chromium in water samples through sequential combination of dispersive magnetic solid phase extraction using mesoporous amino-functionalized Fe3O4/SiO2 nanoparticles and cloud point extraction, Microchem. J., 123 (2015) 185-195.
[128] T. Sumida, T. Ikenoue, K. Hamada, A. Sabarudin, M. Oshima, S. Motomizu, On-line preconcentration using dual mini-columns for the speciation of chromium(III) and chromium(VI) and its application to water samples as studied by inductively coupled plasma-atomic emission spectrometry, Talanta, 68 (2005) 388-393.
[129] J. NamieŚNik, A. Rabajczyk, Speciation Analysis of Chromium in Environmental Samples, Crit. Rev. Environ. Sci. Technol., 42 (2012) 327-377.
[130] J.S. Suleiman, B. Hu, C.Z. Huang, On-line speciation of Cr(III) and Cr(VI) using microcolumn packed with immobilized used green tea leaves (UGTLs) and determination by ICP-OES in environmental water samples, At. Spectrosc., 28 (2007) 234-240.
[131] Q. Meng, Z. Fan, B. Buckley, L. Lin, L. Huang, C.-H. Yu, R. Stiles, L. Bonanno, Development and evaluation of a method for hexavalent chromium in ambient air using IC-ICP-MS, Atmos. Environ., 45 (2011) 2021-2027.
[132] K. Zhao, A. Veksha, L. Ge, G. Lisak, Near real-time analysis of para-cresol in wastewater with a laccase-carbon nanotube-based biosensor, Chemosphere, (2020) 128699.
[133] H. Filik, A.A. Avan, Dextran modified magnetic nanoparticles based solid phase extraction coupled with linear sweep voltammetry for the speciation of Cr(VI) and Cr(III) in tea, coffee, and mineral water samples, Food Chem., 292 (2019) 151-159.

[134] J.R. Zhang, A.L. Zeng, H.Q. Luo, N.B. Li, Fluorescent silver nanoclusters for ultrasensitive determination of chromium(VI) in aqueous solution, J. Hazard. Mater., 304 (2016) 66-72.
[135] A. Manova, S. Humenikova, M. Strelec, E. Beinrohr, Determination of chromium(VI) and total chromium in water by in-electrode coulometric titration in a porous glassy carbon electrode, Microchim. Acta, 159 (2007) 41-47.
[136] J.P. Metters, R.O. Kadara, C.E. Banks, Electroanalytical sensing of chromium(iii) and (vi) utilising gold screen printed macro electrodes, Analyst, 137 (2012) 896-902.
[137] A. Salimi, B. Pourbahram, S. Mansouri-Majd, R. Hallaj, Manganese oxide nanoflakes/multi-walled carbon nanotubes/chitosan nanocomposite modified glassy carbon electrode as a novel electrochemical sensor for chromium (III) detection, Electrochim. Acta, 156 (2015) 207-215.
[138] A.K. Das, C.R. Raj, Shape-controlled growth of surface-confined Au nanostructures for electroanalytical applications, J. Electroanal. Chem., 717 (2014) 140-146.
[139] W. Jin, G.S. Wu, A.C. Chen, Sensitive and selective electrochemical detection of chromium(VI) based on gold nanoparticle-decorated titania nanotube arrays, Analyst, 139 (2014) 235-241.
[140] J. Wei, Z. Guo, X. Chen, D.D. Han, X.K. Wang, X.J. Huang, Ultrasensitive and Ultraselective impedimetric Detection of Cr(VI) Using Crown Ethers as High-Affinity Targeting Receptors, Anal. Chem., 87 (2015) 1991-1998.
[141] C.M. Welch, M.E. Hyde, O. Nekrassova, R.G. Compton, The oxidation of trivalent chromium at polycrystalline gold electrodes, Phys. Chem. Chem. Phys., 6 (2004) 3153-3159.
[142] M. Yang, L.F. Allard, M. Flytzani-Stephanopoulos, Atomically Dispersed Au–(OH)x Species Bound on Titania Catalyze the Low-Temperature Water-Gas Shift Reaction, J. Am. Chem. Soc., 135 (2013) 3768-3771.
[143] L. Alves, B. Ballesteros, M. Boronat, J.R. Cabrero-Antonino, P.

Concepción, A. Corma, M.A. Correa-Duarte, E. Mendoza, Synthesis and Stabilization of Subnanometric Gold Oxide Nanoparticles on Multiwalled Carbon Nanotubes and Their Catalytic Activity, J. Am. Chem. Soc., 133 (2011) 10251-10261.
[144] M.-L. Chen, L.-Y. Ma, X.-W. Chen, New procedures for arsenic speciation: A review, Talanta, 125 (2014) 78-86.
[145] M.S. Reid, K.S. Hoy, J.R.M. Schofield, J.S. Uppal, Y. Lin, X. Lu, H. Peng, X.C. Le, Arsenic speciation analysis: A review with an emphasis on chromatographic separations, TrAC, Trends Anal. Chem., 123 (2020) 115770.
[146] S.G. Johnston, W.W. Bennett, N. Doriean, K. Hockmann, N. Karimian, E.D. Burton, Antimony and arsenic speciation, redox-cycling and contrasting mobility in a mining-impacted river system, Sci. Total Environ., 710 (2020) 136354.
[147] N.M. Zarić, S. Braeuer, W. Goessler, Arsenic speciation analysis in honey bees for environmental monitoring, J. Hazard. Mater., 432 (2022) 128614.
[148] C.M. Navarathna, A.G. Karunanayake, S.R. Gunatilake, C.U. Pittman, F. Perez, D. Mohan, T. Mlsna, Removal of Arsenic(III) from water using magnetite precipitated onto Douglas fir biochar, Journal of Environmental Management, 250 (2019) 109429.
[149] M. Contreras-Acuña, T. García-Barrera, M.A. García-Sevillano, J.L. Gómez-Ariza, Speciation of arsenic in marine food (Anemonia sulcata) by liquid chromatography coupled to inductively coupled plasma mass spectrometry and organic mass spectrometry, J. Chromatogr. A, 1282 (2013) 133-141.
[150] A. Gonzálvez, A. Llorens, M.L. Cervera, S. Armenta, M. de la Guardia, Non-chromatographic speciation of inorganic arsenic in mushrooms by hydride generation atomic fluorescence spectrometry, Food Chem., 115 (2009) 360-364.
[151] S.J. Stetson, C. Lawrence, S. Whitcomb, C. Kanagy, Determination of

four arsenic species in environmental water samples by liquid chromatography-inductively coupled plasma - tandem mass spectrometry, MethodsX, 8 (2021) 101183.
[152] F. Ardini, G. Dan, M. Grotti, Arsenic speciation analysis of environmental samples, J. Anal. At. Spectrom., 35 (2020) 215-237.
[153] Z.-G. Liu, X.-J. Huang, Voltammetric determination of inorganic arsenic, TrAC, Trends Anal. Chem., 60 (2014) 25-35.
[154] H. Hu, B. Xie, Y. Lu, J. Zhu, Advances in Electrochemical Detection Electrodes for As(III), Nanomaterials, 12 (2022) 781.
[155] P. Mukherjee, B. Raj, U. Adhikari, M. Mohapatra, Recent advances, challenges, and future road map in determination of trace As(III) via hybrid electroactive materials: A review, Mater. Res. Bull., 169 (2024) 112535.
[156] S. Jain, R. Panwar, J. Mathur, Design and development of colorimetric, whole-cell based, electrochemical biosensors for arsenic detection, Inorg. Chem. Commun., 153 (2023) 110730.
[157] W. Tupiti, S. Chandra, S. Prasad, Sensitive inorganic arsenic speciation on a voltammetric platform in environmental water samples, Microchem. J., 139 (2018) 301-305.
[158] A.A. Ensafi, A.C. Ring, I. Fritsch, Highly Sensitive Voltammetric Speciation and Determination of Inorganic Arsenic in Water and Alloy Samples Using Ammonium 2-Amino-1-Cyclopentene-1-Dithiocarboxylate, Electroanalysis, 22 (2010) 1175-1185.
[159] K. Gibbon-Walsh, P. Salaün, C.M.G. van den Berg, Determination of arsenate in natural pH seawater using a manganese-coated gold microwire electrode, Anal. Chim. Acta, 710 (2012) 50-57.
[160] E.A. Zakharova, G.N. Noskova, S.G. Antonova, A.S. Kabakaev, Speciation of arsenic(III) and arsenic(V) by manganese-mediated stripping voltammetry at gold microelectrode ensemble in neutral and basic medium, Int. J. Environ. Anal. Chem., 94 (2014) 1478-1498.
[161] X. Dai, R.G. Compton, Detection of As(iii) via oxidation to As(v) using

platinum nanoparticle modified glassy carbon electrodes: arsenic detection without interference from copper, Analyst, 131 (2006) 516-521.
[162] M. Yang, X. Chen, T.-J. Jiang, Z. Guo, J.-H. Liu, X.-J. Huang, Electrochemical Detection of Trace Arsenic(III) by Nanocomposite of Nanorod-Like α-MnO2 Decorated with ~5 nm Au Nanoparticles: Considering the Change of Arsenic Speciation, Anal. Chem., 88 (2016) 9720-9728.
[163] B. Ren, P. Sudarsanam, A.E. Kandjani, B. Hillary, M.H. Amin, S.K. Bhargava, L.A. Jones, Electrochemical Detection of As (III) on a Manganese Oxide-Ceria (Mn2O3/CeO2) Nanocube Modified Au Electrode, Electroanalysis, 30 (2018) 928-936.
[164] S. Nanda, F. Berruti, Municipal solid waste management and landfilling technologies: a review, Environ. Chem. Lett., 19 (2021) 1433-1456.
[165] THE WORLD BANK, Trends in Solid Waste Management, 2020.
[166] E. US, Toxicity characteristics leaching procedure (TCLP), method 1311, US Environmental Protection Agency USA, 1992.
[167] K. Yin, X. Dou, W.-P. Chan, V.W.-C. Chang, Comparative leaching characteristics of fly/bottom ashes from municipal solid waste incineration under various environmental stresses, J. Mater. Cycles Waste Manage., 22 (2020) 46-55.
[168] Y. Tian, S. Dai, J. Wang, Environmental standards and beneficial uses of waste-to-energy (WTE) residues in civil engineering applications, Waste Disposal & Sustainable Energy, 5 (2023) 323-350.
[169] R. Siddique, G. Kaur, A. Rajor, Waste foundry sand and its leachate characteristics, Resources, Conservation and Recycling, 54 (2010) 1027-1036.
[170] G. Gupta, M. Datta, G.V. Ramana, B.J. Alappat, S. Bishnoi, Contaminants of concern (CoCs) pivotal in assessing the fate of MSW incineration bottom ash (MIBA): First results from India and analogy between several countries, Waste Management, 135 (2021) 167-181.
[171] J. Lehmann, A. Cowie, C.A. Masiello, C. Kammann, D. Woolf, J.E. Amonette, M.L. Cayuela, M. Camps-Arbestain, T. Whitman, Biochar in climate

change mitigation, Nature Geoscience, 14 (2021) 883-892.
[172] Y. Xie, L. Wang, H. Li, L.J. Westholm, L. Carvalho, E. Thorin, Z. Yu, X. Yu, Ø. Skreiberg, A critical review on production, modification and utilization of biochar, Journal of Analytical and Applied Pyrolysis, 161 (2022) 105405.
[173] G. Jha, S. Soren, K.D. Mehta, Partial substitution of coke breeze with biomass and charcoal in metallurgical sintering, Fuel, 278 (2020) 118350.
[174] M. Hassan, Y. Liu, R. Naidu, S.J. Parikh, J. Du, F. Qi, I.R. Willett, Influences of feedstock sources and pyrolysis temperature on the properties of biochar and functionality as adsorbents: A meta-analysis, Sci. Total Environ., 744 (2020) 140714.
[175] A. Choudhury, S. Lansing, Biochar addition with Fe impregnation to reduce H_2S production from anaerobic digestion, Bioresour. Technol., 306 (2020) 123121.
[176] L. Li, D. Zou, Z. Xiao, X. Zeng, L. Zhang, L. Jiang, A. Wang, D. Ge, G. Zhang, F. Liu, Biochar as a sorbent for emerging contaminants enables improvements in waste management and sustainable resource use, Journal of Cleaner Production, 210 (2019) 1324-1342.
[177] L. Lu, X. Li, M. Mahoney, Z. Zhang, Biomass materials for metallurgical applications, Hindawi, 2018.
[178] J. Lee, K.-H. Kim, E.E. Kwon, Biochar as a catalyst, Renewable and Sustainable Energy Reviews, 77 (2017) 70-79.
[179] Y. Ding, Y. Liu, S. Liu, Z. Li, X. Tan, X. Huang, G. Zeng, L. Zhou, B. Zheng, Biochar to improve soil fertility. A review, Agron. Sustain. Dev., 36 (2016) 1-18.
[180] Z. Chen, V. Kamchoom, A. Apriyono, R. Chen, C. Chen, Laboratory study of water infiltration and evaporation in biochar-amended landfill covers under extreme climate, Waste Management, 153 (2022) 323-334.
[181] L. Qin, X. Huang, Q. Xue, L. Liu, Y. Wan, In-situ biodegradation of harmful pollutants in landfill by sludge modified biochar used as biocover, Environ. Pollut., 258 (2020) 113710.

[182] L. Zhang, Z. Xu, A review of current progress of recycling technologies for metals from waste electrical and electronic equipment, Journal of Cleaner Production, 127 (2016) 19-36.
[183] M. Rosende, M. Miró, Recent trends in automatic dynamic leaching tests for assessing bioaccessible forms of trace elements in solid substrates, TrAC, Trends Anal. Chem., 45 (2013) 67-78.
[184] S. Lin, X. Zhou, L. Ge, S.H. Ng, X. Zhou, V.W.-C. Chang, Development of an accelerated leaching method for incineration bottom ash correlated to toxicity characteristic leaching protocol, Electrophoresis, 37 (2016) 2458-2461.
[185] T.I. Wong, X. Zhou, L. Ge, G. Lisak, K. Zhao, Leaching device, 2024.
[186] Y. Lu, X. Liang, C. Niyungeko, J. Zhou, J. Xu, G. Tian, A review of the identification and detection of heavy metal ions in the environment by voltammetry, Talanta, 178 (2018) 324-338.
[187] K. Zhao, C. Mao, R. Ding, D. Song, L. Ge, G. Lisak, Simultaneous Speciation of Inorganic Arsenic (III and V) Utilizing Gold-Manganese Oxide Nanoparticles Modified Electrochemical Sensors, Electrochim. Acta, (2024) 144796.
[188] K. Zhao, L. Ge, T.I. Wong, X. Zhou, G. Lisak, Gold-silver nanoparticles modified electrochemical sensor array for simultaneous determination of chromium(III) and chromium(VI) in wastewater samples, Chemosphere, 281 (2021) 130880.
[189] A. Biffis, P. Centomo, A. Del Zotto, M. Zecca, Pd Metal Catalysts for Cross-Couplings and Related Reactions in the 21st Century: A Critical Review, Chem. Rev., 118 (2018) 2249-2295.
[190] A. Chen, C. Ostrom, Palladium-Based Nanomaterials: Synthesis and Electrochemical Applications, Chem. Rev., 115 (2015) 11999-12044.
[191] S.K. Konda, A. Chen, Palladium based nanomaterials for enhanced hydrogen spillover and storage, Mater. Today, 19 (2016) 100-108.
[192] S. McCarthy, D.C. Braddock, J.D.E.T. Wilton-Ely, Strategies for sustainable palladium catalysis, Coord. Chem. Rev., 442 (2021) 213925.

[193] K.S. Egorova, V.P. Ananikov, Which Metals are Green for Catalysis? Comparison of the Toxicities of Ni, Cu, Fe, Pd, Pt, Rh, and Au Salts, Angew. Chem. Int. Ed., 55 (2016) 12150-12162.
[194] B. Baś, K. Węgiel, K. Jedlińska, New voltammetric sensor based on the renewable bismuth bulk annular band electrode and its application for the determination of palladium(II), Electrochim. Acta, 178 (2015) 665-672.
[195] F.D. Hardcastle, I.E. Wachs, The molecular structure of bismuth oxide by Raman spectroscopy, J. Solid State Chem., 97 (1992) 319-331.
[196] J. Steele, R. Lewis, In situ micro-Raman studies of laser-induced bismuth oxidation reveals metastability of β-Bi 2 O 3 microislands, Optical Materials Express, 4 (2014) 2133-2142.
[197] J. Malm, E. Sahramo, J. Perälä, T. Sajavaara, M. Karppinen, Low-temperature atomic layer deposition of ZnO thin films: Control of crystallinity and orientation, Thin Solid Films, 519 (2011) 5319-5322.
[198] J. Hou, C. Yang, Z. Wang, W. Zhou, S. Jiao, H. Zhu, In situ synthesis of α–β phase heterojunction on Bi2O3 nanowires with exceptional visible-light photocatalytic performance, Applied Catalysis B: Environmental, 142-143 (2013) 504-511.
[199] R. Li, W. Chen, H. Kobayashi, C. Ma, Platinum-nanoparticle-loaded bismuth oxide: an efficient plasmonic photocatalyst active under visible light, Green Chem., 12 (2010) 212-215.
[200] D. D'Angelo, S. Filice, M. Miritello, C. Bongiorno, E. Fazio, F. Neri, G. Compagnini, S. Scalese, β-Bi2O3 reduction by laser irradiation in a liquid environment, Phys. Chem. Chem. Phys., 20 (2018) 10292-10301.
[201] X. Li, Y. Sun, T. Xiong, G. Jiang, Y. Zhang, Z. Wu, F. Dong, Activation of amorphous bismuth oxide via plasmonic Bi metal for efficient visible-light photocatalysis, J. Catal., 352 (2017) 102-112.
[202] J. Rashid, S. Karim, R. Kumar, M.A. Barakat, B. Akram, N. Hussain, H.B. Bin, M. Xu, A facile synthesis of bismuth oxychloride-graphene oxide composite for visible light photocatalysis of aqueous diclofenac sodium, Sci.

Rep., 10 (2020) 14191.
[203] V. Vivier, A. Régis, G. Sagon, J.Y. Nedelec, L.T. Yu, C. Cachet-Vivier, Cyclic voltammetry study of bismuth oxide Bi2O3 powder by means of a cavity microelectrode coupled with Raman microspectrometry, Electrochim. Acta, 46 (2001) 907-914.
[204] J. Liu, B. Sun, J. Hu, Y. Pei, H. Li, M. Qiao, Aqueous-phase reforming of ethylene glycol to hydrogen on Pd/Fe3O4 catalyst prepared by co-precipitation: Metal–support interaction and excellent intrinsic activity, J. Catal., 274 (2010) 287-295.
[205] J. Wang, W. Xu, H. Liu, F. Yu, H. Wang, Extractant structures and their performance for palladium extraction and separation from chloride media: A review, Miner. Eng., 163 (2021) 106798.
[206] E.F. Bazarkina, G.S. Pokrovski, J.-L. Hazemann, Structure, stability and geochemical role of palladium chloride complexes in hydrothermal fluids, Geochim. Cosmochim. Acta, 146 (2014) 107-131.
[207] A.S. Kholmogorova, E.A. Svintsova, L.K. Neudachina, E.L. Lebedeva, I.S. Puzyrev, Potentiometric Determination of Palladium(II) in Aqueous Solutions Using a Modified Carbon-Paste Electrode, J. Anal. Chem., 75 (2020) 679-684.
[208] A. Sharif, M. Ashraf, A.A. Anjum, A. Javeed, I. Altaf, M.F. Akhtar, M. Abbas, B. Akhtar, A. Saleem, Pharmaceutical wastewater being composite mixture of environmental pollutants may be associated with mutagenicity and genotoxicity, Environmental Science and Pollution Research, 23 (2016) 2813-2820.
[209] F. Mehrarad, P. Ziarati, Z. Mousavi, Removing heavy metals from pharmaceutical effluent by plarganium grandiflorum, Biomedical and Pharmacology Journal, 9 (2016) 151-161.
[210] O.O. James, K. Nwaeze, E. Mesagan, M. Agbojo, K.L. Saka, D. Olabanji, Concentration of heavy metals in five pharmaceutical effluents in Ogun State, Nigeria, Bull Environ Pharmacol Life Sci, 2 (2013) 84-90.

[211] J. Wang, J. Lu, Ü.A. Kirgöz, S.B. Hocevar, B. Ogorevc, Insights into the anodic stripping voltammetric behavior of bismuth film electrodes, Anal. Chim. Acta, 434 (2001) 29-34.
[212] M. Bissen, F.H. Frimmel, Arsenic — a Review. Part II: Oxidation of Arsenic and its Removal in Water Treatment, Acta hydrochimica et hydrobiologica, 31 (2003) 97-107.
[213] W. Song, W. Ma, J. Ma, C. Chen, J. Zhao, Y. Huang, Y. Xu, Photochemical Oscillation of Fe(II)/Fe(III) Ratio Induced by Periodic Flux of Dissolved Organic Matter, Environ. Sci. Technol., 39 (2005) 3121-3127.
[214] P. He, T. Mao, A. Wang, Y. Yin, J. Shen, H. Chen, P. Zhang, Enhanced reductive removal of ciprofloxacin in pharmaceutical wastewater using biogenic palladium nanoparticles by bubbling H2, Rsc Adv, 10 (2020) 26067-26077.
[215] D. Fontana, M. Pietrantonio, S. Pucciarmati, G.N. Torelli, C. Bonomi, F. Masi, Palladium recovery from monolithic ceramic capacitors by leaching, solvent extraction and reduction, J. Mater. Cycles Waste Manage., 20 (2018) 1199-1206.
[216] B. Jiang, Y. Gong, J. Gao, T. Sun, Y. Liu, N. Oturan, M.A. Oturan, The reduction of Cr(VI) to Cr(III) mediated by environmentally relevant carboxylic acids: State-of-the-art and perspectives, J. Hazard. Mater., 365 (2019) 205-226.
[217] T. Pavesi, J.C. Moreira, Mechanisms and individuality in chromium toxicity in humans, J. Appl. Toxicol., 40 (2020) 1183-1197.
[218] T.L. DesMarias, M. Costa, Mechanisms of chromium-induced toxicity, Current Opinion in Toxicology, 14 (2019) 1-7.
[219] N. Hilali, H. Mohammadi, A. Amine, N. Zine, A. Errachid, Recent Advances in Electrochemical Monitoring of Chromium, Sensors, 20 (2020) 5153.
[220] K. Midander, A. Julander, J. Kettelarij, C. Lidén, Testing in artificial sweat – Is less more? Comparison of metal release in two different artificial sweat solutions, Regul. Toxicol. Pharm., 81 (2016) 381-386.

[221] F. Séby, S. Charles, M. Gagean, H. Garraud, O.F.X. Donard, Chromium speciation by hyphenation of high-performance liquid chromatography to inductively coupled plasma-mass spectrometry—study of the influence of interfering ions, J. Anal. At. Spectrom., 18 (2003) 1386-1390.
[222] L. Xing, D. Beauchemin, Chromium speciation at trace level in potable water using hyphenated ion exchange chromatography and inductively coupled plasma mass spectrometry with collision/reaction interface, J. Anal. At. Spectrom., 25 (2010) 1046-1055.
[223] B. Boruah, R. Gupta, J.M. Modak, G. Madras, Novel insights into the properties of AgBiO3 photocatalyst and its application in immobilized state for 4-nitrophenol degradation and bacteria inactivation, J. Photochem. Photobiol. A: Chem., 373 (2019) 105-115.
[224] E. Albiter, M.A. Valenzuela, S. Alfaro, G. Valverde-Aguilar, F.M. Martínez-Pallares, Photocatalytic deposition of Ag nanoparticles on TiO2: Metal precursor effect on the structural and photoactivity properties, J. Saudi Chem. Soc., 19 (2015) 563-573.
[225] L. Zeng, C. Dai, B. Liu, C. Xue, Oxygen-assisted stabilization of single-atom Au during photocatalytic hydrogen evolution, J Mater Chem A, 7 (2019) 24217-24221.
[226] S. Wu, N. Chandra Sekar, S.N. Tan, H. Xie, S.H. Ng, Determination of chromium(iii) by differential pulse stripping voltammetry at a chitosan–gold nanocomposite modified screen printed electrode, Anal. Methods, 8 (2016) 962-967.
[227] T. Alizadeh, F. Rafiei, N. Hamidi, M.R. Ganjali, A new electrochemical sensing platform for Cr(III) determination based on nano-structured Cr(III)-imprinted polymer-modified carbon composite electrode, Electrochim. Acta, 247 (2017) 812-819.
[228] T.N. Ravishankar, S. Muralikrishna, K. Suresh kumar, G. Nagaraju, T. Ramakrishnappa, Electrochemical detection and photochemical detoxification of hexavalent chromium (Cr(vi)) by Ag doped TiO2 nanoparticles, Anal.

Methods, 7 (2015) 3493-3499.
[229] B. Kowsalya, V.V. Anusha Thampi, V. Sivakumar, B. Subramanian, Electrochemical detection of Chromium(VI) using NiO nanoparticles, J. Mater. Sci.: Mater. Electron., 30 (2019) 14755-14761.
[230] G. Genchi, G. Lauria, A. Catalano, A. Carocci, M.S. Sinicropi, Arsenic: A Review on a Great Health Issue Worldwide, Applied Sciences, 2022.
[231] A. Sattar, S. Xie, M.A. Hafeez, X. Wang, H.I. Hussain, Z. Iqbal, Y. Pan, M. Iqbal, M.A. Shabbir, Z. Yuan, Metabolism and toxicity of arsenicals in mammals, Environmental Toxicology and Pharmacology, 48 (2016) 214-224.
[232] R. Khanam, A. Kumar, A.K. Nayak, M. Shahid, R. Tripathi, S. Vijayakumar, D. Bhaduri, U. Kumar, S. Mohanty, P. Panneerselvam, D. Chatterjee, B.S. Satapathy, H. Pathak, Metal(loid)s (As, Hg, Se, Pb and Cd) in paddy soil: Bioavailability and potential risk to human health, Sci. Total Environ., 699 (2020) 134330.
[233] S. Kempahanumakkagari, A. Deep, K.-H. Kim, S. Kumar Kailasa, H.-O. Yoon, Nanomaterial-based electrochemical sensors for arsenic - A review, Biosens. Bioelectron., 95 (2017) 106-116.
[234] S. Vaidya, O. Veselska, A. Zhadan, M. Diaz-Lopez, Y. Joly, P. Bordet, N. Guillou, C. Dujardin, G. Ledoux, F. Toche, Transparent and luminescent glasses of gold thiolate coordination polymers, Chemical Science, 11 (2020) 6815-6823.
[235] A.M. Abdelghany, A.H. Oraby, M.O. Farea, Influence of green synthesized gold nanoparticles on the structural, optical, electrical and dielectric properties of (PVP/SA) blend, Physica B: Condensed Matter, 560 (2019) 162-173.
[236] S. Almheiri, A.A.L. Ahmad, B. Le Droumaguet, R. Pires, A.A. Mohamed, M.M. Chehimi, Development of Latent Fingerprints via Aryldiazonium Tetrachloroaurate Salts on Copper Surfaces: An XPS Study, Langmuir, 36 (2020) 74-83.
[237] D.P. Anderson, J.F. Alvino, A. Gentleman, H.A. Qahtani, L. Thomsen,

M.I.J. Polson, G.F. Metha, V.B. Golovko, G.G. Andersson, Chemically-synthesised, atomically-precise gold clusters deposited and activated on titania, Phys. Chem. Chem. Phys., 15 (2013) 3917-3929.
[238] M. Turner, V.B. Golovko, O.P.H. Vaughan, P. Abdulkin, A. Berenguer-Murcia, M.S. Tikhov, B.F.G. Johnson, R.M. Lambert, Selective oxidation with dioxygen by gold nanoparticle catalysts derived from 55-atom clusters, Nature, 454 (2008) 981-983.
[239] R. Ghobeira, P.S. Esbah Tabaei, R. Morent, N. De Geyter, Chemical characterization of plasma-activated polymeric surfaces via XPS analyses: A review, Surf. Interfaces, 31 (2022) 102087.
[240] E. Bolli, S. Kaciulis, A. Mezzi, R. Montanari, A. Varone, XPS investigation of 5N purity Al thin foils for MEMS devices, Surf. Interface Anal., 55 (2023) 466-473.
[241] G. Varga, A. Sápi, T. Varga, K. Baán, I. Szenti, G. Halasi, R. Mucsi, L. Óvári, J. Kiss, Z. Fogarassy, B. Pécz, Á. Kukovecz, Z. Kónya, Ambient pressure CO2 hydrogenation over a cobalt/manganese-oxide nanostructured interface: A combined in situ and ex situ study, J. Catal., 386 (2020) 70-80.
[242] F.A. Al-Agel, E. Al-Arfaj, A.A. Al-Ghamdi, Y. Losovyj, L.M. Bronstein, W.E. Mahmoud, A novel recipe to improve the magnetic properties of Mn doped CeO2 as a room temperature ferromagnetic diluted metal oxide, Journal of Magnetism and Magnetic Materials, 360 (2014) 73-79.
[243] C. Mao, D. Yuan, L. Wang, E. Bakker, Separating boundary potential changes at thin solid contact ion transfer voltammetric membrane electrodes, J. Electroanal. Chem., 880 (2021) 114800.
[244] D.G. Leaist, Mutual Diffusion Coefficients for Binary Aqueous Solutions of Arsenous, Arsenic, and Malonic Acids, J. Chem. Eng. Data, 52 (2007) 1319-1325.
[245] J. Durst, A. Siebel, C. Simon, F. Hasché, J. Herranz, H.A. Gasteiger, New insights into the electrochemical hydrogen oxidation and evolution reaction mechanism, Energy Environ. Sci., 7 (2014) 2255-2260.

[246] D.S. Silvester, K.R. Ward, L. Aldous, C. Hardacre, R.G. Compton, The electrochemical oxidation of hydrogen at activated platinum electrodes in room temperature ionic liquids as solvents, J. Electroanal. Chem., 618 (2008) 53-60.
[247] C. Sullivan, D. Lu, A. Senecal, P. Kurup, Voltammetric detection of arsenic (III) using gold nanoparticles modified carbon screen printed electrodes: Application for facile and rapid analysis in commercial apple juice, Food Chem., 352 (2021) 129327.
[248] L. Bu, Q. Xie, H. Ming, Gold nanoparticles decorated three-dimensional porous graphitic carbon nitrides for sensitive anodic stripping voltammetric analysis of trace arsenic(III), Journal of Alloys and Compounds, 823 (2020) 153723.
[249] E. Toral-Sanchez, J.R. Rangel-Mendez, L.F. Chazaro-Ruiz, Characterization of iron-modified carbon paste electrodes and their application in As(V) detection, J. Appl. Electrochem., 46 (2016) 205-215.
[250] Y.-j. Zheng, F.-x. Xiao, Y. Wang, C.-h. Li, W. Xu, H.-s. Jian, Y.-t. Ma, Industrial experiment of copper electrolyte purification by copper arsenite, Journal of Central South University of Technology, 15 (2008) 204-208.
[251] Z. Liu, D. Wang, B. Peng, L. Chai, S. Yang, C. Liu, C. Zhang, X. Xie, H. Liu, Mercury Re-Emission in the Smelting Flue Gas Cleaning Process: The Influence of Arsenite, Energy Fuels, 31 (2017) 11053-11059.
[252] M. Weil, Crystal Structure Refinements of the Lead(II) Oxoarsenates(V) Pb2As2O7, Pb(H2AsO4)2, Pb5(AsO4)3OH and NaPb4(AsO4)3 from Single-Crystal X-ray Data, Minerals, 11 (2021) 1156.
[253] S.K. Kim, D. Josell, T.P. Moffat, Electrodeposition of Cu in the PEI-PEG-Cl-SPS Additive System: Reduction of Overfill Bump Formation During Superfilling, J. Electrochem. Soc., 153 (2006) C616.
[254] B. Hoyer, N. Jensen, Suppression of surfactant interferences in anodic stripping voltammetry by sodium dodecyl sulfate, Electrochem. Commun., 5 (2003) 759-764.
[255] M.T. Emett, G.H. Khoe, Photochemical oxidation of arsenic by oxygen

and iron in acidic solutions, Water Res., 35 (2001) 649-656.
[256] P.V. Nidheesh, T.S.A. Singh, Arsenic removal by electrocoagulation process: Recent trends and removal mechanism, Chemosphere, 181 (2017) 418-432.
[257] L. Hao, M. Liu, N. Wang, G. Li, A critical review on arsenic removal from water using iron-based adsorbents, Rsc Adv, 8 (2018) 39545-39560.
[258] C. Sullivan, M. Tyrer, C.R. Cheeseman, N.J.D. Graham, Disposal of water treatment wastes containing arsenic — A review, Sci. Total Environ., 408 (2010) 1770-1778.
[259] V. Intrakamhaeng, K.A. Clavier, T.G. Townsend, Hazardous waste characterization implications of updating the toxicity characteristic list, J. Hazard. Mater., 383 (2020) 121171.
[260] Y.H. Jayaneththi, D. Robert, F. Giustozzi, A critical review on leaching of contaminants from asphalt pavements, Sci. Total Environ., 950 (2024) 174967.
[261] H.T. Kim, T.G. Lee, A simultaneous stabilization and solidification of the top five most toxic heavy metals (Hg, Pb, As, Cr, and Cd), Chemosphere, 178 (2017) 479-485.
[262] K. Zhao, L. Ge, G. Lisak, Facile synthesis of electrocatalytically active bismuth oxide nanosheets for detection of palladium traces in pharmaceutical wastewater, Environ. Pollut., 307 (2022) 119524.
[263] H. Ehrlich, K.D. Demadis, O.S. Pokrovsky, P.G. Koutsoukos, Modern Views on Desilicification: Biosilica and Abiotic Silica Dissolution in Natural and Artificial Environments, Chem. Rev., 110 (2010) 4656-4689.
[264] R. Shetty, N.B. Prakash, Effect of different biochars on acid soil and growth parameters of rice plants under aluminium toxicity, Sci. Rep., 10 (2020) 12249.
[265] D. Lakshmanan, D. Clifford, G. Samanta, Arsenic Removal by Coagulation With Aluminum, Iron, Titanium, and Zirconium, Journal AWWA, 100 (2008) 76-88.

[266] B. Dhal, H.N. Thatoi, N.N. Das, B.D. Pandey, Chemical and microbial remediation of hexavalent chromium from contaminated soil and mining/metallurgical solid waste: A review, J. Hazard. Mater., 250-251 (2013) 272-291.
[267] I. Wittayarak, A. Imyim, K. Wongravee, Simultaneous removal of As(III) and As(V) from wastewater by co-precipitation using an experimental design approach, Desalination and Water Treatment, 57 (2016) 16571-16582.
[268] J. Zhang, C. Zhang, G. Wei, Y. Li, X. Liang, W. Chu, H. He, D. Huang, J. Zhu, R. Zhu, Reduction removal of hexavalent chromium by zinc-substituted magnetite coupled with aqueous Fe(II) at neutral pH value, J. Colloid Interface Sci., 500 (2017) 20-29.
[269] M. Shi, X. Min, Y. Ke, Z. Lin, Z. Yang, S. Wang, N. Peng, X. Yan, S. Luo, J. Wu, Y. Wei, Recent progress in understanding the mechanism of heavy metals retention by iron (oxyhydr)oxides, Sci. Total Environ., 752 (2021) 141930.
[270] I. Ilyin, T. Berg, S. Dutchak, J. Pacyna, Heavy metals, EMEP assessment part I European perspective. Norwegian Meteorological Institute, Oslo, (2004) 107-128.
[271] S.A. Mansour, Heavy metals of special concern to human health and environment, Practical food safety: contemporary issues and future directions, (2014) 213-233.
[272] Y. Wang, X. Wu, J. Sun, C. Wang, G. Zhu, L.-P. Bai, Z.-H. Jiang, W. Zhang, Stripping voltammetric determination of cadmium and lead ions based on a bismuth oxide surface-decorated nanoporous bismuth electrode, Electrochem. Commun., 136 (2022) 107233.
[273] N.P.T. Nguyen, H.T. Nguyen, H.V. Nguyen, L.T. Hoang, Gold–Copper Film Electrode for Voltammetry Determination of Mercury in Water, Journal of Nanomaterials, 2021 (2021) 2202677.
[274] J. Zhang, Q. Zhang, X. Feng, Support and Interface Effects in Water-Splitting Electrocatalysts, Adv. Mater., 31 (2019) 1808167.

[275] H. Alwael, A.S. Alharthi, M.M. Dabi, M. Oubaha, M.S. El-Shahawi, A highly sensitive electrochemical sensing probe incorporating classical Berthelot's reaction and glassy carbon electrode for measuring ultra-trace levels of ammonia/ NH4+ in water, Electrochem. Commun., 162 (2024) 107686.
[276] National Environment Agency of Singapore, LEACHING TEST - RECOMMENDED ACCEPTANCE CRITERIA FOR SUITABILITY OF INDUSTRIAL WASTES FOR LANDFILL DISPOSAL.
[277] Y. Duan, X. Liu, W. Hong, Z. Khalid, G. Lv, X. Jiang, Leaching behavior and comprehensive toxicity evaluation of heavy metals in MSWI fly ash from grate and fluidized bed incinerators using various leaching methods: A comparative study, Sci. Total Environ., 914 (2024) 169595.
[278] X. Dong, L.Q. Ma, Y. Li, Characteristics and mechanisms of hexavalent chromium removal by biochar from sugar beet tailing, J. Hazard. Mater., 190 (2011) 909-915.
[279] K. Zoroufchi Benis, A. Motalebi Damuchali, J. Soltan, K.N. McPhedran, Treatment of aqueous arsenic – A review of biochar modification methods, Sci. Total Environ., 739 (2020) 139750.